MICROSTRUCTURE EVOLUTION AND MECHANICAL RESPONSE OF THERMALLY AGED AND IRRADIATED FE-CR ALLOYS

A Dissertation Presented for the

Doctor of Philosophy

Degree

The University of Tennessee, Knoxville

Pengcheng Zhu

May 2023

ACKNOWLEDGEMENT

This work was supported by the U.S. Department of Energy, Office of Nuclear Energy, under contract as part of the SNAP consortium research activities, and under DOE Idaho Operations Office Contract DE-AC07- 051D14517 as part of a Nuclear Science User Facilities experiment. The fabrication of the Fe-Cr binary alloys has been carried out within the framework of the EUROfusion. The APT work was conducted at the ORNL's Center for Nanophase Materials Sciences, which is a DOE office of Science User Facility. The author would like to acknowledge funding from the State of Tennessee and Tennessee Higher Education Commission (THEC) through their support of the Center for Materials Processing. Thank you to my advisor, Dr. Steven Zinkle, for the generous support and guidance during my PhD research. I am grateful for the help and constructive suggestions from the committee members, Dr. Shradha Agarwal, Dr. Brian Wirth, Dr. Sudarsanam Babu and Dr. Warren Oliver. The thanks also go to Dr. Jean Henry for providing binary FeCr alloys, Dr. Yan-Ru Lin for help on TEM characterizations, Dr. Stephen Taller for irradiations on T91 and HT9 alloys, Dr. Caleb Massey for help with the APT data collection and Jennifer Hay (KLA company) for technical support in nanoindentation testing. I sincerely appreciate the discussions and help from Dr. Ling Wang, Dr. Yajie Zhao, Yao Li, Qinyun Chen, Zehui Qi and other group colleagues. Finally, I will thank my parents, Mrs. Yunchun Wang and Mr. Yingming Zhu, who always provide strong emotional support and understand my decision thoroughly during the past five years.

ABSTRACT

Estimations of bulk hardness from nanoindentation are frequently subject to considerable uncertainties due to indentation size effects (ISE), pileup effects, and potential influence of surface quality or test methods. This study examined materials science principles of the nanoindentation test method to enable accurate prediction of bulk hardness from nano scale, and correlated microstructure with mechanical properties. The research started by developing a scientific nanoindentation test protocol on a series of high purity Fe and Fe-(3-25 wt. %) Cr alloys. These materials were tested in as-annealed and thermally aged (100-900 hours at 475 ℃ to produce Cr-rich α' precipitates) conditions. Nanoindentation with a Berkovich indenter at constant strain rate (0.05 to 0.5 /s) and constant loading rate conditions provided comparable bulk equivalent hardness (H_0) extracted by Nix-Gao model, indicating a weak strain rate sensitivity at room temperature. Results from electropolished and fine mechanically polished samples gave comparable measured hardness. Pileup corrections produced a 5-14% correction to H_0 which agreed with the experimental bulk Vickers hardness within ~10% for most tested materials. The microstructural model-predicted and measured strength values agreed for aged samples. A derived analytic expression demonstrates that an ISE error, associated with inappropriate methods such as hardness ratios or changes at a reference depth, can be as large as 60% in estimated bulk hardness for the investigated Fe-Cr alloys. Subsequently, the nanoindentation protocol was applied to ion irradiated binary Fe18Cr alloys. The microstructure was characterized by APT, S/TEM and EDS to understand the irradiation effects on the mechanical properties. An accurate way to calculate the strength factor was provided based on the size of the defects. A newly refined hardening model with superposition method was applied to correlate the microstructures with the mechanical properties, which further demonstrated the consistency between model prediction and nanoindentation measurement. This study also provides insight into the fidelity of ion irradiation as a surrogate of neutron irradiation based on the dual ion irradiated and neutron irradiated T91 and HT9 ferritic/ martensitic steels. Microstructures and mechanical properties were quantified and compared according to the protocol developed in the thermally aged and ion irradiated binary alloys.

TABLE OF CONTENTS

LIST OF TABLES

LIST OF FIGURES

CHAPTER 1. INTRODUCTION

High chromium ferritic-martensitic steels are one of the candidate structural component materials for future fission and fusion reactors due to their low swelling rates, low thermal expansion coefficient, good elevated-temperature strength, high conductivity, etc. They are considered as fuel cladding and wrapper materials for fast reactors and first wall and blanket structures for fusion reactors [1]. Considering the need for safe operation of advanced fission and fusion reactors under higher neutron flux and temperatures than the present reactors, the component integrity associated with the mechanical properties of the structural materials is extremely important. Conventionally, the mechanical properties are evaluated by tensile testing to obtain the yield strength, elongation, ultimate strength, etc. for the neutron and as-received alloys due to the uniform structures. However, there are several challenges with studying the degradation of mechanical properties of neutron irradiated alloys. Both commercial and test reactors have relatively low damage rate, which means it is generally not possible to measure the evolution of mechanical properties with irradiation (to avoid any possible accident due to material degradation) by accelerated testing in any fission reactor. Besides, a long-term cooling for the hot samples may be needed since the radioactivity induced by neutron irradiation makes it difficult to perform characterizations on the materials immediately after irradiation. Other issues such as the rising cost for neutron irradiation and limited access to neutron facilities also impede investigating irradiation effect son mechanical properties.

Ion irradiation is a promising way to simulate neutron irradiation with high damage rate and low radioactive productions. A successful simulation requires high similarities in both neutron-modified microstructures and neutron-induced bulk properties with those caused by ion irradiation. The state-of-art techniques, such as TEM, APT, XRD, etc. can provide detailed characterization on the evolution of microstructures, with little technical differences to characterizing neutron samples. Conversely, the tensile or Vickers testing methods, used for neutron samples, are no longer appropriate for ion-irradiated samples due to shallow and nonuniform damage layer, which introduces a new problem to obtain the mechanical properties of Fe-Cr alloys. Therefore, the micro- and nano-scale testing methods, such as micro-tensile, micropillar, compression, nanoindentation, etc. are developed to minimize the effect of limited irradiated volume [2–4]. Among all the methods, nanoindentation is the easiest way to characterize the mechanical properties of Fe-Cr alloys in nanoscale, which has been widely used based on the analytical method proposed by Oliver and Pharr [5].

The irradiation-induced defects, such as dislocation loops, precipitates, and cavities,

impede the dislocation motion, resulting in the irradiation hardening. One of the most significant challenges in nanoindentation studies is to bridge the gap between nanoscale and macro-scale hardness, namely develop quantitatively accurate correlations between nanoindentation hardness and Vickers hardness, as well as between nanoindentation hardness and tensile strength. Already in 1951, Tabor [6] noted that bulk indentation hardness is approximately three times the flow stress at a strain of about 8%, i.e., $H=3\sigma_{0.08}$, where H is the Vickers hardness, $\sigma_{0.08}$ is the tensile stress. This simple correlation has been heavily applied and demonstrated on different materials for many decades. Therefore, the hardness can be an indicator of the tensile properties of the irradiated materials. For historical reasons, the Vickers hardness is defined as the load divided by actual surface area which can be expressed as $A_V=26.43h^2$, where h is the indent depth. As with most hardness tests, the projected contact area is applied in the definition of Berkovich pyramid nanoindentation hardness and (ignoring potential pileup effects) is given by $A_n=24.50h^2$. Therefore, an ideal correlation factor between Vickers and bulk equivalent hardness can be simply derived from the area ratio as H_V (kgf/mm^2)/H_0 (MPa)=0.095. However, this correlation factor varies considerably among different investigations even for a similar alloy system such as Fe-Cr alloys, e.g. the reported ratio for H_V(kgf/mm^2)/H_n(MPa)=0.066 to 0.081 [7–9] etc., as shown in Fig. 1.1. Of potentially even greater concern is the systematic overestimate of bulk hardness obtained from nanoindentation testing (i.e., all of the correlations in Fig. 1.1 have significantly larger nanoindentation hardness compared to the ideal correlation curve). Such a large and skewed variation in this correlation factor (and the even larger variability in the constitutive data points) is an indicator of the current poor quantitative accuracy in extraction of bulk hardness from nanoindentation tests. Numerous potential factors may contribute to the difficulties in accurately evaluating nanoindentation hardness, such as indentation size effect (ISE), strain rate effects, specimen surface preparation, pileup, or sink-in effects. For improved quantitative correlation of nanoindentation hardness to macroscopic Vickers hardness and tensile strength, investigations on the quantitative importance of these various experimental parameters as well as possible refinement of the Nix-Gao model [10] are necessary.

In this study, nanoindentation tests with a Berkovich indenter are performed on a variety of Fe-Cr alloys under as-received and different irradiation conditions to estimate the bulk hardness in nanoscale volumes. The nanoindentation results and microstructures for both ion-irradiated and neutron-irradiated Fe-Cr alloys are compared to further understand the simulation possibility of ion irradiation to neutron irradiation. And the correlation between

nanoindentation tested mechanical properties and microstructure predicted bulk properties are investigated for better understanding the conventional hardening models. This study provides new insights to the way to extract macro properties in nanoscale volume, and how the irradiation conditions, such as temperatures, dose, and dose rate affect the microstructures and mechanical properties of Fe-Cr alloys used in the future fission and fusion reactors.

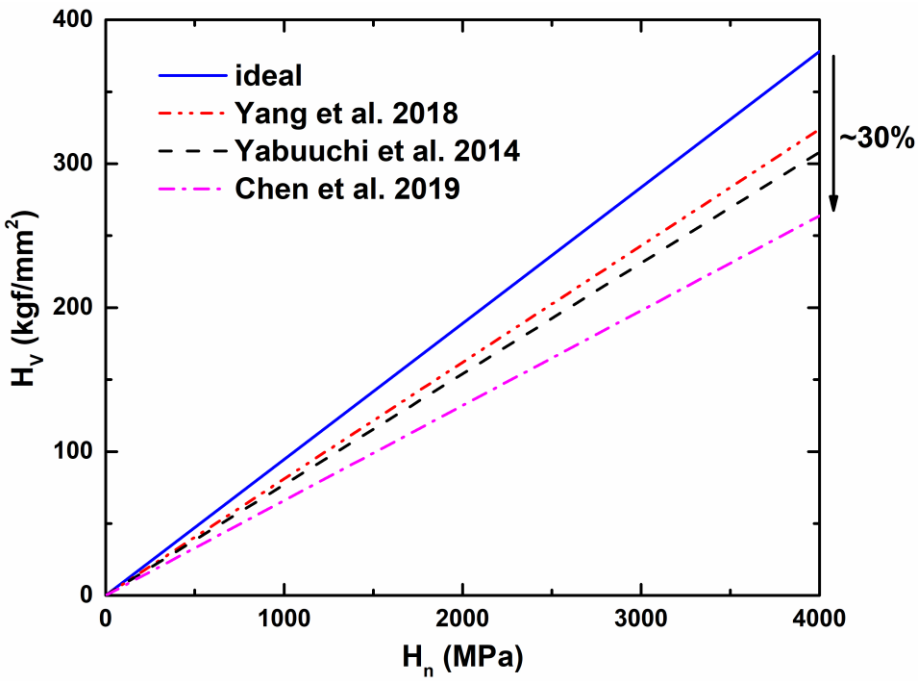

Fig. 1.1 The typical correlation fitting lines between Vickers hardness and nanoindentation hardness for nickel-base and ODS-Fe-Cr alloys [7], 316L stainless steel [8] and cast austenitic stainless steel [9]. The ideal correlation line is shown for reference purposes.

CHAPTER 2. LITERATURE REVIEW

2.1. Fe-Cr alloys as candidates for next generation fission and fusion reactors

Considering the safe and efficient operation of the fission and fusion reactors, the radiation resistance is the most challenging issue. Fig. 2.1 presents the operating temperature and lifetime damage in the next generation fission and fusion reactors. Comparing with the current fission reactor, the advanced fission reactors and fusion reactors operate at much higher temperatures and dpa levels. This requires the use of higher performance materials compared to what is employed in current water-cooled fission reactors. For the structural materials used in fusion reactors, there are three major options: ferritic/martensitic steels, vanadium alloys and SiC/SiC ceramic composites. The high chromium Fe-Cr alloys containing 9-12%Cr are very promising since this kind of material has been widely developed with good resistance to void swelling, low expansion coefficient, high thermal conductivity, and good high temperature strength. Meanwhile, the extensive accumulated expertise in the fabrication and engineering application of Fe-Cr alloys in the general power-industry promotes their practical use now and in the future [11].

There is a long history to use high chromium Fe-Cr alloys in the power generation industry. The additions of Mo, V, Nb and W elements in the Fe-Cr alloys increased the creep-rupture strength from 40MPa to 180MPa up to 650 ℃ [12]. Later in 1970s, the Fe-Cr alloys were considered as candidate structural materials for the advanced fission and fusion reactors [13]. However, the high neutron irradiation and high operating temperature requires good resistance to irradiation degradation of mechanical properties and low production of radioactivity during the service time. Therefore, the high-radioactive elements in the conventional Fe-Cr alloys, such as molybdenum and niobium, were replaced by tungsten (and/or vanadium) and tantalum, respectively, to develop the reduced-activation ferritic/martensitic steels [14]. Another issue that may challenge the use of Fe-Cr alloys in fusion reactors is the ferro-magnetic characteristic. The magnetostatic field of the fusion reactor to confine the plasma particles will induce negligible stresses on the F/M steels. There is still lack of comprehensive understanding about the ferromagnetic effects for the Fe-Cr alloys used as the first wall and blank materials [1].

2.2. Thermal aging effect on mechanical properties of Fe-Cr alloys

Pronounced precipitation and impurities segregation can occur during long term thermal aging following the normalizing and tempering. These phenomena have significant effects on

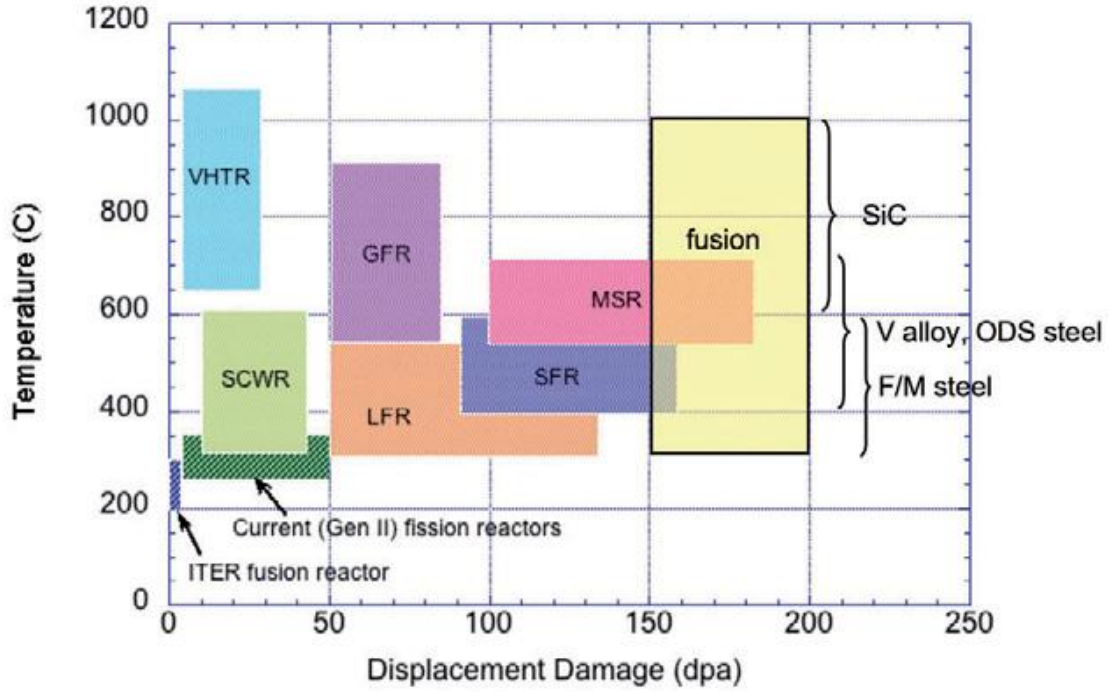

Fig. 2.1 Overview of the operating temperatures and damage levels for the current fission and future fission and fusion reactors. Reproduced from Ref. [11].

the mechanical properties of Fe-Cr alloys, such as strength, fracture toughness and resistance to cracking.

In 9-12% Cr F/M steels, the most common phases that formed during thermal aging are the $M_{23}C_6$ carbides, where M refers to the metal elements and C refers to carbon. Meanwhile, some other carbides and nitrides will also precipitate in the matrix. With increasing aging time, the M_2X phase decomposition occurs and is replaced by MX, Z, and Laves phases [15]. In the typical 9-12% Fe-Cr alloys, i.e., 9Cr-1Mo (T91) and 12Cr-1moVW (HT9), the Laves phases consist of Fe_2Mo, Fe_2W and $Fe_2(Mo,W)$ [16]. They are the predominant precipitates in the temperature regime of 450 to 650 ℃, forming at the prior austenite grain boundary and the lath boundaries, which would be one of the originations of the embrittlement of the materials. Another important precipitate at temperatures in the range 400 to 550 ℃ is the coherent Cr-rich α' precipitate, which is well known as the cause of the 475 ℃ embrittlement of the Fe-Cr F/M steel [17,18]. Although the phase boundary of the α and α' phases has not been well defined, the typical Cr content for the formation of α' precipitates is larger than 12% [1,19]. Table 2.1 summaries the main precipitates that will form after normalizing and tempering, long-term aging, and creep testing in the temperature range of 400-750 ℃.

Generally, high-temperature thermal aging effect on the tensile strengths of 9-12% Cr alloys is relatively small when testing at room temperature [1]. Huang et al. investigated the reduced activation ferritic-martensitic (RAFM) steels (9%Cr) which were thermally aged at 600 ℃ to 650 ℃ for 1100h and 3000h. They found that the yield strength changed slightly, and the upper shelf energy of the aged steels decreased with increasing aging time (as shown in Fig. 2.2). The DBTT shifting to higher temperature is mainly caused by the formation of Laves phase during thermal aging, which is the deteriorated impact to the mechanical properties of the steels [20]. The degradation of the creep resistance of the 9-12% Cr alloys at elevated temperatures was also attributed to the formation of Z-phase and Laves phases, which is favored by the depletion of the (Nb,V) X particles during the long-term creep [21].

2.3. Radiation effects on the microstructure of Fe-Cr alloys

Irradiation-induced defects, such as precipitates, dislocation loops, cavities, etc. can work as the obstacles for the motion of dislocations, resulting in the degradation of mechanical properties of Fe-Cr alloys. It has been proved that irradiation dose, temperature, dose rate, have a significant effect on microstructures. For better understanding how the microstructures affect

Table 2.1 Summary of the precipitates in the normalized-tempered, aged, and creep-rupture tested high chromium F/M steels. Reproduced from [1].

Precipitates	Crystal structure and lattice parameter	Typical composition	Distribution
$M_{23}C_6$	FCC, a=1.066 nm	$(Cr_{16}Fe_6Mo)C_6$ $(Cr_4Fe_{12}Mo_4Si_2WV)C_6$	Coarse particles at prior austenite grain and martensite lath boundaries and fine intra-lath particles.
MX	FCC, a=0.444-0.447 nm	NbC, NbN, VN, (CrV)N, Nb(CN) (NbV)C	Undissolved particles and fine precipitates at martensite lath boundaries
M_2X	Hexagonal, a=0.478 nm c=0.444 nm	Cr_2N, Mo_2C, W_2C	Martensite lath boundaries (Cr_2N and Mo_2C); prior austenite grain boundaries (Mo_2C); intra-lath (Mo_2C and W_2C); δ-ferrite in duplex steels [$Cr_2(CN)$ and $(CrMo)_2(CN)$]
Laves phase	Hexagonal a=0.4744 nm c=0.7725 nm	Fe_2Mo, Fe_2W, $Fe_2(MoW)$	Prior austenite grain and martensite lath boundaries and intra-lath; δ-ferrite in duplex steels
Z-phase	Tetragonal a=0.286 nm c=0.739 nm	(CrVNb)N	Large plate-like particles in the matrix after creep straining at 600 ℃
η-carbide	Diamond cubic a=1.07-1.22 nm	M6C $(Fe_{39}Cr_6Mo_4Si_{10})C$	Prior austenite grain and martensite lath boundaries and intra-lath
Vanadium carbide	FCC a=0.420 nm	V_4C_3	Low number density in matrix
Chi(χ)	BCC a=0.892 nm	$M_{18}C$ or $Fe_{35}Cr_{12}Mo_{10}C$	Intra-martensite lath; δ-ferrite in duplex steels
α' precipitate	BCC a=0.287 nm	Cr-rich precipitates	In the matrix

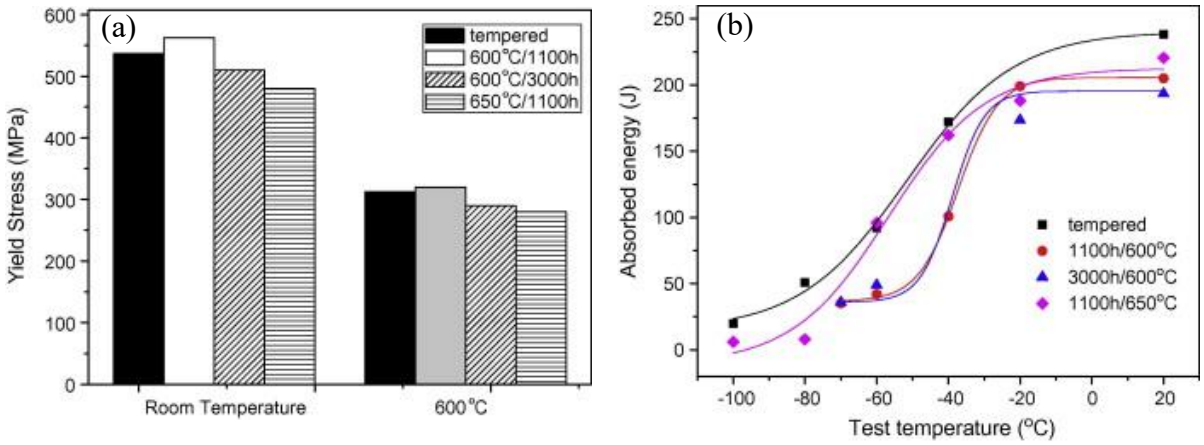

Fig. 2.2 (a) Yield strength and (b) Charpy impact curves of as-tempered and aged CLAM steel. Reproduced from Ref. [20].

the mechanical properties under ion irradiation and using ion irradiation to predict neutron irradiation effects, it is imperative to investigate the evolution of the microstructures of Fe-Cr alloys under different irradiation conditions.

2.3.1. Precipitates

Most of the precipitates can be formed during thermal aging as mentioned the section 2.2, while irradiation has a significant effect on precipitation through three mechanisms, i.e., radiation induced phases, radiation-modified phases, and radiation-enhanced-phases [22]. Radiation-induced precipitation refers to those that cannot be formed under thermal aging but occur after irradiation, and radiation-modified precipitation means modifying the composition of the precipitates by incorporation of the solute atoms. These two mechanisms are related to the radiation-induced segregation. High temperature irradiation drives the fluxes of point defects to the sinks such as dislocation loops, cavities, grain boundaries, etc. Accompanying with this process, the solutes coupled with the point defects will move to the sinks and form the accumulation of solute atoms, which can significantly change the local chemical distribution [23]. The radiation-induced segregation finally induces a new phase or modifies the preexisting phase, known as radiation-induced precipitation and radiation-modified precipitation, respectively. G phase is a kind of precipitate forming in the irradiated materials due to irradiation induced segregation. At a fixed dose rate, the number density of G phase decreased while the size increased with the increasing irradiation temperature. And the precipitate size also increased as the irradiation dose increased [24].

The changes of precipitation during irradiation can also be a result of radiation enhanced diffusion (RED) of solute atoms, which can cause radiation-enhanced precipitation. It typically takes a long time for a second phase to achieve equilibrium under thermal aging. Irradiation accelerates the formation of these phases due to enhanced diffusion of the solute atoms by increasing the concentration of point defects. The α' precipitates can be induced by this mechanism.

For binary Fe-Cr alloys under thermal aging or neutron irradiation, the Cr-rich α' precipitates are one of the main second phases. Although these precipitates are extremely small in size (~2 nm), their large number density still contributes to a pronounced hardening effect [25], which is the cause of embrittlement phenomenon in irradiated Fe-Cr alloys. For commercial bcc Fe-Cr alloys, such as HT9 and T91 with Cr content $\leq$ 12%, α' precipitates

were mainly observed after neutron irradiation, while ion irradiation generally did not induce these coherent precipitates due to the difference of dose rate between neutron and ion irradiations [24,26]. The formation of α' precipitates is highly affected by the irradiation conditions, such as temperature, dose and dose rate since these parameters impact the competition between irradiation-enhanced diffusion and ballistic dissolution. For neutron irradiation, the α' precipitates were observed in Fe-Cr alloys with Cr content larger than 9 at. % at around 300 ℃. With increasing Cr content > 12 at. %, the phase can be formed at elevated temperatures around 400-450 ℃. But there are still confusions regarding the location of the solvus boundary between single phase (α) and two phase ($\alpha + \alpha'$) regimes. A dose rate effect on the formation of α' precipitates was observed when comparing the neutron and ion irradiation with dose rate of ~10^{-7} and ~10^{-4} dpa/s, respectively [26]. The relatively high dose rate of ion irradiation reduced the time for Cr atoms diffusing to form α' precipitates and enhanced the point defect recombination rate and ballistic dissolution rate, thereby causing reduced α' precipitate formation for ion irradiation conditions [27].

2.3.2. Dislocation loops

The displacement damage induced by the high-energy neutrons can result in larger amount of defect clusters consisting of interstitials and vacancies. At irradiation temperatures below 0.3 T_m, where T_m is the melting temperature of the material, the interstitials are first activated and diffuse to form the dislocation loops. While at higher temperature larger than 0.2 T_m, the mobility of the vacancies increases, and vacancy-type dislocation loops are formed. There are two common dislocation loops with the Burgers vectors of a<100> and a/2<111> in the both ion and neutron irradiated pure Fe and Fe-Cr F/M steels [28–31], both of which are perfect loops since the high stacking fault energy of bcc Fe-Cr alloys inhibits the formation of faulted loops. The a<100> loops are sessile while the a/2<111> loops are glissile, thus the number ratio of these two types will have an important effect on the mechanical properties of the Fe-Cr alloys.

After neutron irradiation under ~450 ℃, Zheng et al. have found that a<100> loops are predominant in the F/M HT9 and T91 alloys at high doses (above 4 dpa), and the number density of the dislocation loops increased with the increasing temperature. However, higher temperature (>~450 ℃) did not favor the formation of dislocation loops, and dislocation lines with Burgers vector of 1/2<111> were observed [32]. The total number density of the

dislocation loops also increased with the increasing irradiation doses as reported for HT9 and T91 in the literatures [33–36].

2.3.3. Cavities

Cavity is a general term that describes either a void or a bubble. A void contains no gas atoms or is in an underpressurized state, while a bubble is in pressurized state with gas atoms inside, such as helium formed during the transmutation reactions in nuclear reactors [37]. The void generally did not appear below 0.3 T_m due to the low mobility of the vacancies and their recombination with interstitials [1]. At the temperature range of 0.3-0.6 T_m, the vacancy accumulation due to irradiation-induced segregation can result in void swelling that will finally cause volumetric expansion, a deterioration on the dimension of the component materials [11]. At higher temperatures > 0.5 T_m, the He-vacancy complexes can migrate to the grain boundaries and cause intergranular fracture under the stresses.

The helium production from the (n, α) reactions in the neutron environment has a pronounced effect on both the microstructure and mechanical properties on the Fe-Cr alloys. He atoms cannot dissolve into the matrix due to zero solubility, thus stabilizing the vacancies by forming He-vacancy clusters. The strong binding energy of the vacancies to He reduces the critical size for the growth of the cavities [38], which is favorable for the formation of large amount of small helium bubbles.

The void swelling, $\frac{\Delta V}{V}$, is always used to evaluate the effect of the cavities on the change of the macroscopic dimensions, where V is the original volume of the material and ΔV is the increased volume due to expansion. Fig. 2.3 compares the swelling behaviors of several typical austenitic and F/M steels with the increasing dose [39]. It is clear that above ~10 dpa, the austenitic steels swell rapidly, while the F/M steels have significantly lower void swelling in a wide range of the damage level. This better void swelling resistance of bcc alloys can be explained by the lower dislocation bias and higher sink strength.

2.4. Radiation effect on the mechanical properties of Fe-Cr alloys

Microstructural evolution under irradiation has been heavily studied on the Fe-Cr alloys, with the final purpose to understand how these microstructures affect the macroscopic properties. The tensile strength, ductility, fracture toughness, fatigue and irradiation creep are essentially needed to evaluate the mechanical properties of the Fe-Cr alloys used in the

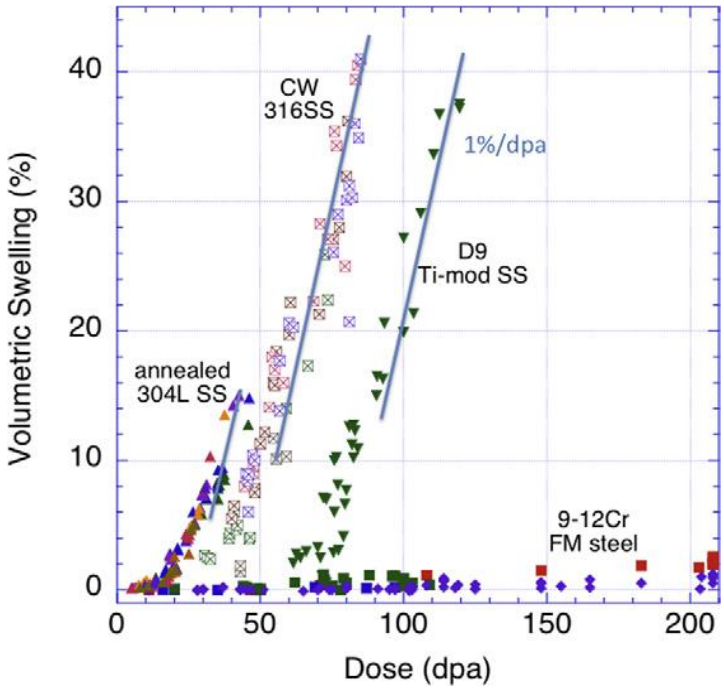

Fig. 2.3 Comparison of the swelling behavior of austenitic and ferritic/martensitic steels. Reproduced from Ref. [39].

irradiation environment. Among these properties, the tensile properties are the most commonly measured due to the simple testing process, and they can be used to predict the other mechanical properties.

2.4.1. Tensile properties

The microstructures are affected by the irradiation conditions, and so are the mechanical properties. The neutron irradiation temperature has a strong effect on the strength of the F/M steels. Below $0.35T_m$, the irradiation-induced interstitial and vacancy loops can result in hardening. In the temperature range of 0.35-0.4 T_m, the hardening effect is mainly from the larger loops, dislocation networks and irradiation-induced or -enhanced precipitation. At elevated temperature > 0.4 T_m, the diffusion is accelerated and the defects that induced by irradiation can anneal out, along with rapid coarsening of the precipitates.

The anticipated operational temperature window for FeCr F/M steels used in nuclear reactors is limited to 350-550 ℃ [40–42], due to low temperature hardening/embrittlement and high temperature creep loss. As shown in Fig. 2.4, neutron irradiation induced hardening is pronounced at relatively low temperatures (less than 350-400 ℃), while high temperature (>~450-500 ℃) produces insignificant radiation hardening [43]. The yield strength gradually decreases with the increasing irradiation temperature, followed by a rapid decrease near 350-400 ℃. The lowest irradiation hardening appears near 400 ℃, beyond which no significant hardening is observed. Fig. 2.5 exhibits the dependence of yield strength on irradiation dose for FM steels [43]. Pronounced irradiation hardening is observed at very low doses of ~0.1-0.2 dpa and the yield strength increases rapidly with dose within ~10 dpa. After ~10-15 dpa, the increase of irradiation hardening slows down until a near-saturation is approached at higher doses due to the saturation of irradiation induced microstructures. For the reduced activation ferritic martensitic (RAFM) steels the saturation occurs after ~15 dpa, while for the conventional 9%Cr FM steels, irradiation hardening continues to increase up to ~40 dpa.

For bcc alloys under irradiation, the typical stress-strain curve is characteristic of a rapid load drop after yielding and a low uniform elongation, i.e., there is a smaller segment of work hardening comparing with the austenitic steels [44]. The loss of elongation or ductility is primarily attributed to irradiation hardening, which is an important issue for use of FM steels in rectors. Fig. 2.6 shows the irradiation dose effect on the elongation of FM and ODS steels [43]. Near the same dose interval where irradiation hardening rapidly increases, ~0.1 dpa, the uniform elongation dramatically drops for FM steels. After about ~0.5 dpa, the FM steels

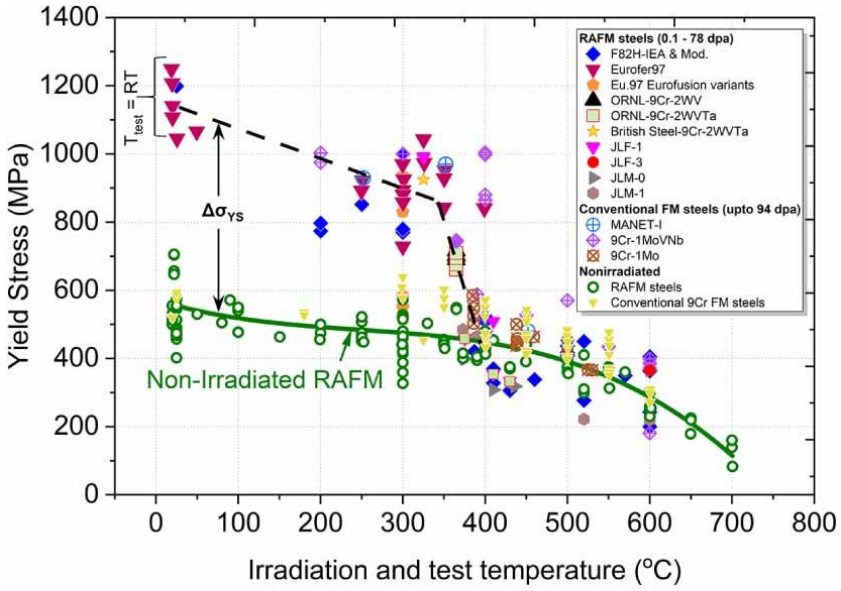

Fig. 2.4 The yield strength evolution with neutron irradiation temperature for FM steels. Reproduced from Ref. [43].

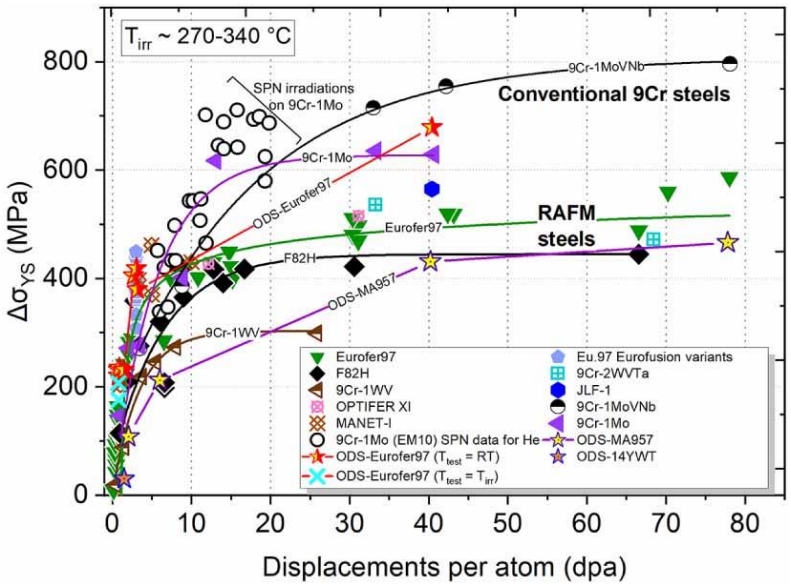

Fig. 2.5 The dependence of irradiation hardening on irradiation doses for FM and ODS steels. Reproduced from Ref. [43].

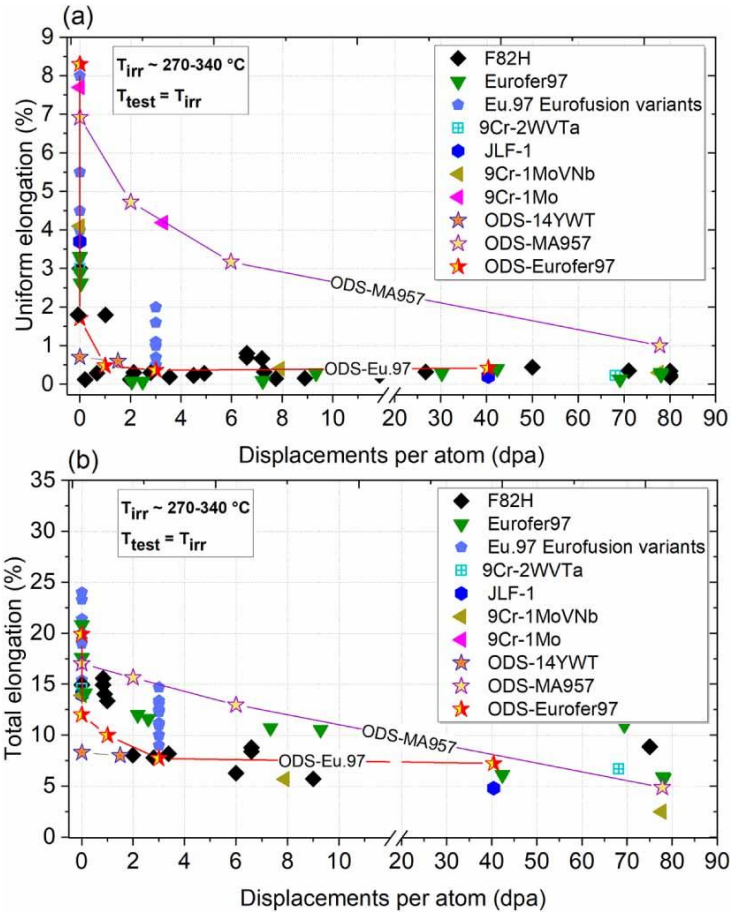

Fig. 2.6 The (a) uniform elongation and (b) total elongation of FM and ODS steels under neutron irradiation. Reproduced from Ref. [43].

generally exhibit negligible uniform elongation, indicating pronounced plastic instability at higher doses. For the total elongation as shown in Fig. 2.6b, although a significant decrease occurs in the dose regime of 0-3 dpa, the elongation is overall typically > 5%.

As confined by the radioactivity of the bulk materials, the tensile tests were generally preformed at the same temperature with the neutron irradiation. Therefore, the evolution of the tensile properties was affected not only by the change of microstructures but may also be affected by irradiation-accelerated thermal aging.

2.4.2. Impact and fracture toughness

The most serious problems faced by ferritic/martensitic steels is the effect of neutron irradiation on the fracture behavior [1], which is manifested as an increase of the ductile to brittle transition temperature (DBTT) and a decrease of the upper shelf energy (USE) in a Charpy test. A Charpy test is used to evaluate the irradiation effect on embrittlement by measuring the total energy for a crack to be initiated and propagated from the notch to a complete fracture. Irradiation-produced dislocation loops, precipitates, cavities can cause pronounced hardening effect and resultant embrittlement. The hardening is closely associated with the increase of flow stress which causes a shift in the DBTT [45]. Besides, the transmutation production, helium, which contributes to the hardening, also exacerbate the DBTT shift. The Charpy test is not proper for an engineering design, instead, the fracture toughness test where a critical load to extend a pre-existing crack is measured, is more important than the total energy for a crack propagation which happens in a Charpy test. Besides, the DBTT are generally affected by various factors, such as specimen geometry, specimen sizes, notch acuity, etc., which induces more complications in evaluating the fracture properties [46]. However, the Charpy is an easy way to compare the relative fracture resistance among different materials and provide qualitative predictions on the fracture toughness based on the Charpy impact properties.

It was found that the shift of DBTT occurred at even very low doses [47]. As shown in Fig. 2.7a, there is a ~40 ℃ DBTT shift for the F/M steel MANET II after irradiating to 0.042 dpa at 250 ℃. A slightly higher dose and temperature (0.13 dpa and 400 ℃) contribute to a larger shift of DBTT. Fig. 2.7b presents a clear DBTT shift and a decreased USE after irradiation [48] for 12Cr-1MoVW alloy. Comparing with the unirradiated specimens, the damage level of 10 dpa at 365 ℃ caused a DBTT shift of about 160 ℃. Irradiation to 17 dpa did not produce further DBTT shift, indicating that a saturation of hardening may occur after ~10 dpa. For the

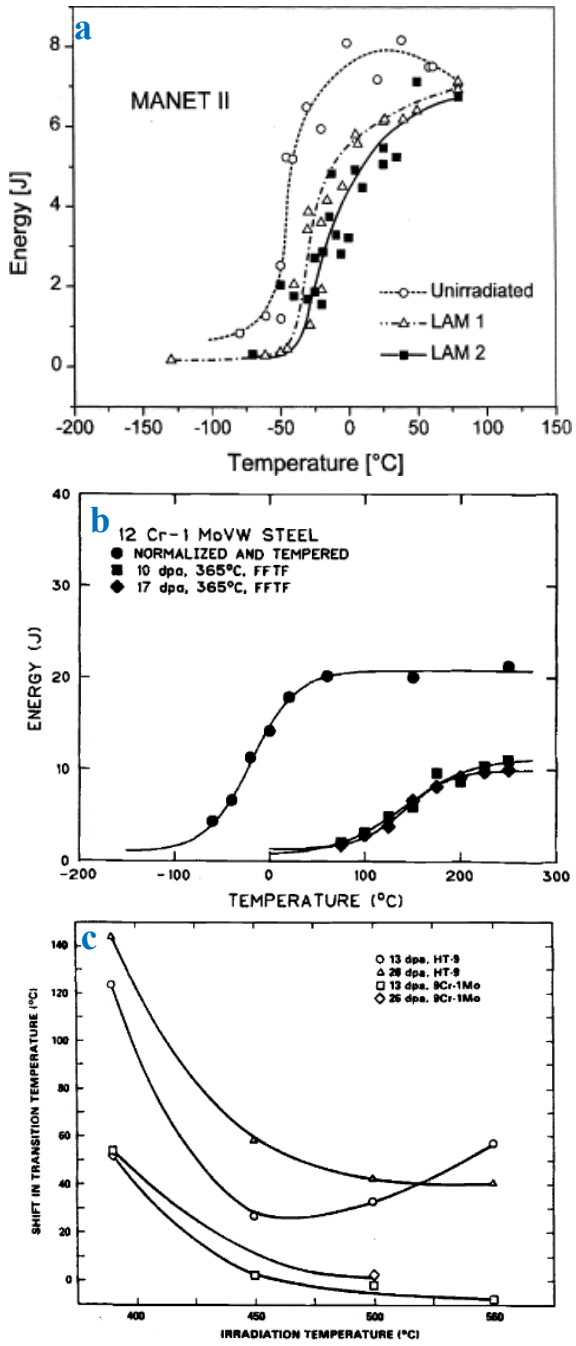

Fig. 2.7 (a) Charpy curves for MANET II irradiated to 0.042 dpa at 250 °C (LAM 1) and to 0.13 dpa at 400 °C (LAM 2). (b) Charpy curves for 12Cr1MoVW steel irradiated to 10 and 17 dpa at 365 °C. (c) The DBTT shift variation with irradiation temperature for 9Cr-1MoVNb and 12Cr-1MoVW steels. Reproduced from Ref. [47–49]

irradiation temperature effect on DBTT shift, Fig. 2.7c shows a clear decreasing trend for the 9Cr-1MoVNb steels, but with little difference between 13 and 26 dpa [49]. The DBTT shift even went to zero at temperatures larger than 450 ℃ due to the vanished hardening at higher temperatures [50]. In contrast, the 12Cr-1MoVW steels showed a more pronounced difference of DBTT shift between two doses at all temperatures. And the shift even increased for 13 dpa above 450 ℃, which was attributed to the coarsening of the precipitates [51].

2.4.3. Irradiation creep

For the long-term operation of reactors, it is impossible to exchange the main structural components, therefore the creep property is extremely important under the harsh neutron irradiation and thermal environment. The thermal creep becomes important for irradiation at temperatures higher than 0.5Tm, while the irradiation creep can occur at lower temperatures. For both time-dependent plastic deformation phenomena, the dislocation climb and glide play an important role in the deformation processes.

There are several possible mechanisms for irradiation creep: swelling-driven creep (I-Creep) [52], stress induced preferential absorption (SIPA) creep [53–55], and preferred absorption glide (PAG) [56]. The fundamental of these mechanisms is the annihilation of the irradiation-produced point defects, resulting in the dislocation climb and glide.

2.5. Ion-irradiation simulation of neutron irradiation

To design the materials used in the next generation fission and advanced fusion reactors, the most ideal way is to investigate the neutron irradiation effect on the candidate materials in real reactors or in test reactors. However, the damage rate in either reactor type is too low to induce irradiation damage in a relatively short period, thus inhibiting the purpose to understand the materials degradation in advance before any possible accident occurs. For example, a typical light water reactor would induce a damage level of 100 dpa to the component materials in the core in the operation lifetime. This will take tens of years for the test reactors to achieve the same dose, due to the low damage rate of 3-10 dpa/year. Other issues on the neutron irradiation are the paucity of the available test reactor for the irradiation, the high radioactivity of the materials after neutron irradiation, and the high cost of such experiments.

Ion irradiation is an alternative way to accelerate the study of irradiation effect on both microstructures and mechanical properties. The high damage rate (typically 10^{-3} to 10^{-4} dpa/s)

can produce the target dose in minutes to hours, which is much faster than test reactors. Meanwhile, ion irradiation generally results in no or little radioactive productions, and the control of the irradiation conditions such as temperature, dose, and dose rate, is easier than test reactors. But there are still several drawbacks for ion irradiation. The charged particles, e.g., electrons, hydrogen, and heavy ions, cannot penetrate as deep as the neutron in materials, resulting in a limited damage volume for the post-irradiation characterization especially for mechanical testing, in which the bulk testing method is not appropriate. The gradient damage level with depth makes it even more complicated to define a characteristic region to study the irradiation effect. Besides, the high dose rate of ion irradiation may produce different microstructures compared with neutron irradiation. And the intrinsic transmutation reaction in neutron irradiation should be accounted for if ion irradiation is used for simulation.

For limited damage volume, alternative micro- and nano-scale mechanical testing methods must be developed and verified [2,3]. The prediction of mechanical properties from microstructure features using proper modeling can avoid directly measuring the properties. There was no observable dose rate effect for the neutron irradiated Fe-Cr alloys, but dose rate in ion irradiation has a significant effect on the void swelling, dislocation loops and precipitates. Therefore, it is necessary to understand how the dose rate affects the microstructures in ion irradiation. Studies have found that the dose rate effect in ion irradiation can be compensated by performing irradiation at higher temperatures to achieve comparable microstructures as in lower dose rate neutron irradiation [57,58]. But for different microstructures (dislocation loops, cavities, precipitates), different temperature shifts are needed. To account for the transmuted H and He in neutron irradiation, simultaneous ion irradiation and H or He implantation can be used. By controlling the ratio of injected He (or H) atoms to the damage level, i.e., the ratio of He/dpa, the dual-ion beam can have a better simulation to the reactor condition.

The limited damage volume and gradient damage level with depth constrain the region where data can be taken for analysis. And the surface effect and injected interstitials can make this analytical region even smaller. The surface can act as sinks for irradiation defects thus altering the formation and growth of the defects [59]. Meanwhile, the injected self ions increase the number of interstitials, which suppresses the void formation and other radiation microstructural evolution processes since the excess interstitials can annihilate with the vacancies [60]. Fig. 2.8 shows the dependence of surface-affected and injection-affected regions on the irradiation temperature and doses. The safe analysis region is reduced at high temperatures and high doses [61].

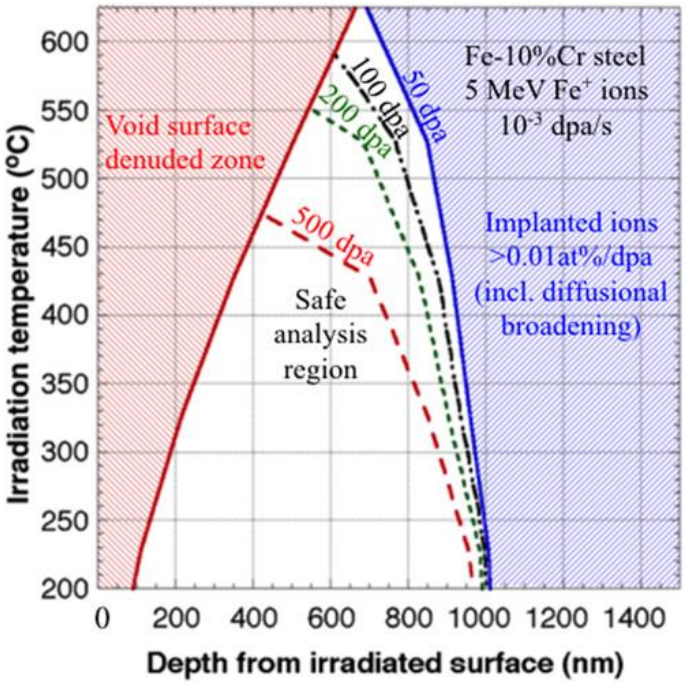

Fig. 2.8 Calculated temperature- and depth-dependent regions affected by the free surface and injected ions for Fe-10Cr steels with 5 MeV Fe^{+} at 10^{-3} dpa/s to dose levels for 50-500 dpa. Reproduced from Ref. [61].

2.6. Micro-tensile testing

High energetic neutron particles can pass through the materials and leave uniform microstructures for the tensile testing. However, the inevitable radioactivity due to transmutation makes it costly to perform bulk mechanical testing such as tensile tests. And the long period needed to achieve the target damage level inhibits the fast investigation on the irradiation effect on mechanical properties. Ion irradiation is a promising alternative way to accelerate such irradiation experiments, but a limited damaged layer brings many complexities to perform tensile testing. In the past decades, small scale testing methods, e.g., micro pillar testing, micro tensile testing, and nanoindentation, have been developed and provide comprehensive understanding of the mechanical response of the Fe-Cr alloys under ion irradiation.

Although macro tensile testing is not available for the ion-irradiated samples due to the need of large-scale specimen, mini tensile bar can be made under the assistance of focused ion beam (FIB) fabrication. It is possible to lift out a tensile specimen in the shallow damaged layer and perform micro-tensile testing in the scanning electron microscope (SEM) or transmission electron microscope (TEM).

Kiener et al. [62] developed a new design for micro-tensile testing using a specifically fabricated sample and sample gripper as shown in Fig. 2.9a. The single-crystal copper sample was fabricated by FIB on a copper needle. This design has been further developed and used to the ion irradiated samples. Vo et al. prepared micro-tensile bar using FIB to study the mechanical properties of HT9 alloys after proton irradiation [63]. And their sample bar is shown in Fig. 2.9b, with the bottom ending attached to the original material. Another configuration of the miniaturized tensile bar is shown in Fig. 2.9c by Miura et al. on Fe and He irradiated F82H alloy [64]. Tungsten deposition was used to fix one side of the bar to a micro-beam and attach the other side to a microprobe which provides tensile loading.

The stress-strain curves of the micro-tensile experiment is quite different with the macro-tensile ones due to reduced testing region with limited grains and dislocations, which is known as “size effect”. The typical plot of stress-strain curves for the micro-tensile testing is shown in Fig. 2.10 [64]. It is clear that the samples failed after a very small strain, with quite lower elongation compared with the conventional tensile testing on large specimens. This reduced elongation in the micro-tensile testing is universal in the literatures. Due to the small specimen

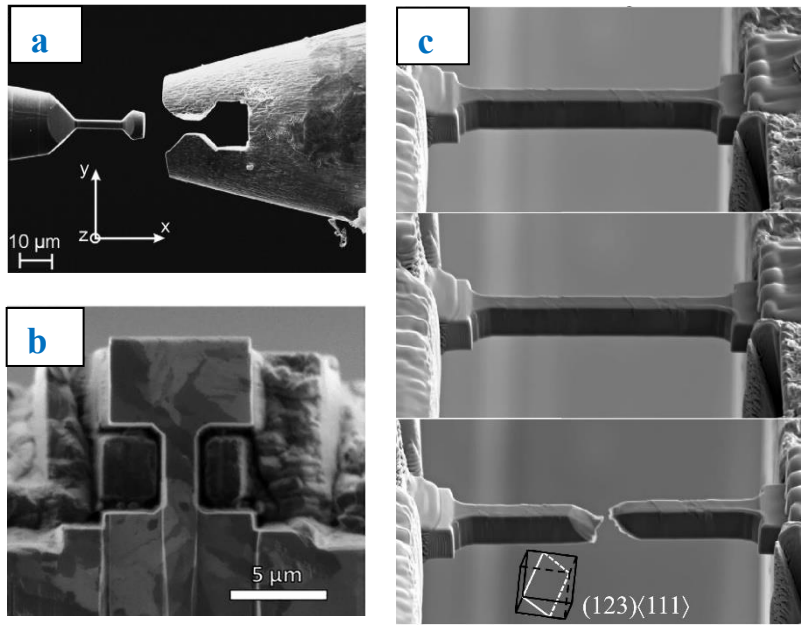

Fig. 2.9 (a) SEM image of a single-crystal copper tension sample (left) and a tungsten sample gripper (right) [62]. (b-c) SEM image of a micro-tensile bar [63,64].

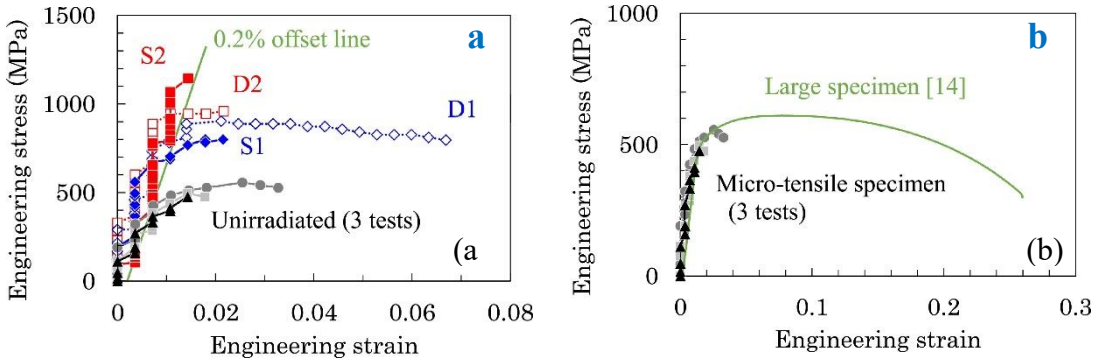

Fig. 2.10 (a) Engineering stress-strain curves for the unirradiated and irradiated F82H. S1 and S2 refer to Fe ion-irradiated samples, and D1 and D2 to the Fe/He ions-irradiated samples. (b) Comparison of the micro-tensile and macro-tensile testing results on the Engineering stress-strain curves. Reproduced from Ref. [64].

size, the density of dislocation and dislocation source is much lower, thus inhibiting the plastic deformation. However, for the strength of micro- and macro- tensile testing, there are many different results. Fig. 2.10b shows that the strength of the micro-tensile specimen is slightly lower than that of the large specimen, and it was attributed to deformable loading direction used for testing. In contrary, Kiener et al. [62] reported higher strength for small specimens, which was caused by the lack of enough dislocations in the testing gauge region compared with the large scale specimens. Vo et al. [63] found that the micros-tensile yield stress is slightly higher than the macroscopic one on the unirradiated samples, while they reported a consistent result on the irradiated specimens. They proposed that irradiation might reduce the size effect.

Micro-tensile testing provides a useful perspective into mechanical studies on irradiated alloys. However, the reduced elongation compared with the conventional tensile testing limits its use to evaluated plasticity. Besides, FIB fabrication work may reduce the yield strength of the sample significantly by introducing surface damage. Johanns et al. studied the in-situ tensile properties of single-crystal Mo alloys and reported that FIB damage played an important role in reducing the measured strength for the pristine samples [65].

2.7. Micro-pillar compression

FIB assisted sample preparation is generally needed for micro-pillar compression testing. A typical micro pilar is shown in Fig. 2.11a [66]. The compression load was applied on the top of the pillar. The in-situ loading under SEM or TEM makes it possible to observe the deformation process simultaneously. During pillar preparation, FIB damage on the samples is not negligible. Ion milling can introduce significant artifacts on the measured strength using small scale mechanical testing methods such as micro compression [67,68] and nanoindentation [69]. For the ion irradiated materials, they are sensitive to the FIB damage, thus a low energy should be used for final stage of ion beam milling. Other issues about the FIB processing include the stress gradient and a consequent strain localization [70,71].

Micropillar testing is also accompanied by the size effect with a typical observation of increased strength with the decreasing characteristic length (the diameter for micropillar), as shown in Fig. 2.11b [66]. It is well known that the plastic deformation is triggered by the motion of the dislocations. But in the miniaturized specimens, there are not enough dislocations thus the stress for the deformation is close to the theoretical strength. For the irradiated samples, irradiation-induced large amount of small defects can create a new small internal material length scale, thus the size effect is reduced until the sample size is comparable to the length

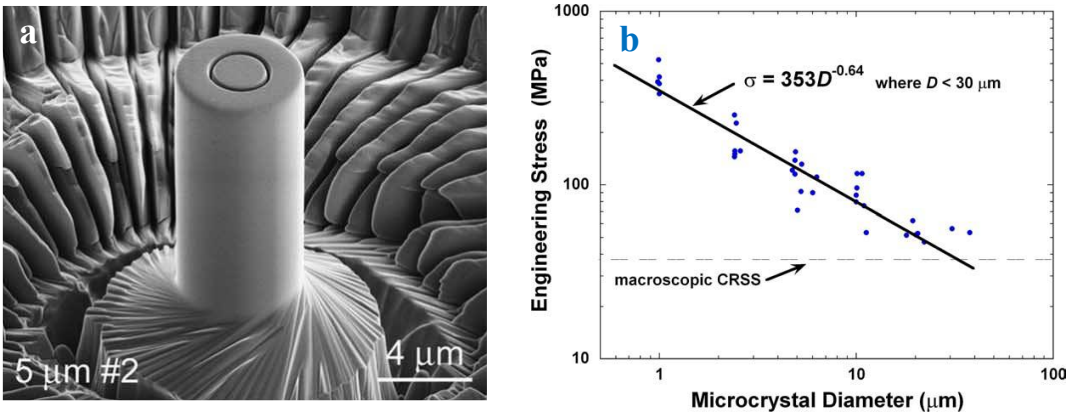

Fig. 2.11 (a) SEM image of the pure nickle micro-pillar with a diameter of 5 μm. (b) The relationship between engineering stress and micropillar diameter. Reproduced from Ref. [66].

scale determined by the grain structure and the radiation defects [4].

In the micropillar testing, the most important parameter to extract is the yield strength since the others, such as total elongation and work hardening capacity, are difficult to be obtained. This testing method can be also performed to investigate the irradiation creep with a constant loading [72].

2.8. Nanoindentation

Compared with the micro-tensile and micro-pillar methods, nanoindentation is a faster and easier way to evaluate the mechanical properties in sub-micro scale. There is no need for FIB preparation on the specimens before performing nanoindentation, thus the experiment process is much more convenient. This depth-sensing indentation method can measure the force and displacement continuously to derive the mechanical properties even at very small depth where the indents are too small to be measured directly.

Fig. 2.12 shows a typical schematic of the load-displacement curve. The P_{max} refers to the peak load, and h_{max} to the peak displacement. h_f is the final depth after unloading.

2.8.1. Fundamental and continuous stiffness measurement

The elastic modulus, E, and the hardness, H, are the two parameters that most measured in the nanoindentation experiments. From the early studies [73–79] on the mechanical properties based on the load-displacement measurement, it has been concluded that the elastic modulus can be determined from the unloading curve since the elastic recovery occurred during this process. And the residual impression kept its geometrical shape even though the recovery occurred. To quantify the modulus, an equation has been proposed,

$$\frac{1}{E_r} = \frac{(1-\nu)}{E} + \frac{(1-\nu_i^2)}{E_i} \tag{2.1}$$

Where E_r is reduced modulus, E is the modulus of the tested material, E_i is the modulus of the indenter. ν and ν_i are the Poisson ratio of the tested material and the indenter, respectively. From the unloading curve, the slope dP/dh at the peak is defined as the experimental measured stiffness, and is associated with the reduce modulus with the following equation,

$$S = \frac{dP}{dh} = \frac{2}{\sqrt{\pi}} E_r \sqrt{A} \tag{2.2}$$

where A is the projected area of the elastic contact. Then sample modulus can be derived according to Eq. 2.1 and 2.2. Then the hardness is calculated according to the simple equation:

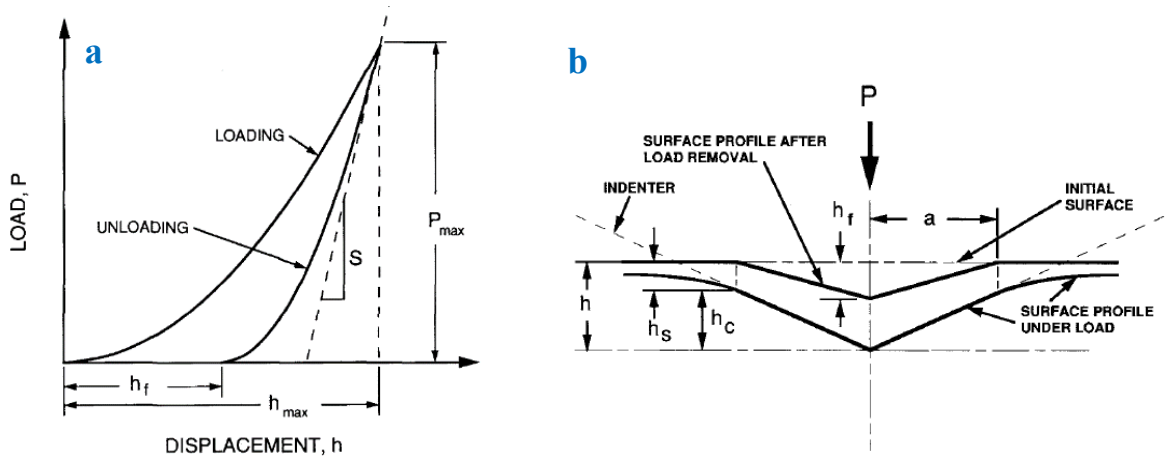

Fig. 2.12 (a) A schematic load-displacement curve. h_f: the residual depth; h_{max}: the peak depth; P_{max}: the peak load; S: the experimental measured stiffness. (b) A schematic cross section of an indent. Reproduced from Ref. [5].

$$H=P/A \tag{2.3}$$

Since the direct measurement of the residual impression especially at shallow depth is difficult, Oliver and Pharr developed a new method to analyze the load-displacement data [5]. This method correlated the contact depth h_c with the contact area A through the geometrical shape of the indenter, and the projected contact area can be directly estimated from the shape function $A(h_c)$. Fig. 2.12b shows a diagram of the cross section of an indent. It is clear that after unloading the final depth decreases but the shape of the indent keeps unchanged. The relation among the total depth, h, surface depth, h_s, and contact depth, h_c, matches the equation $h=h_s+h_c$. The term $h_s=\varepsilon P/S$ here means the distance from the periphery of the contact to the original surface, indicating the elastic recovery. Then the contact depth can be derived according to the equation below,

$$h_c = h - \varepsilon\frac{P}{S} \tag{2.4}$$

where ε is the geometric constant (0.72, 0.75 and 1 for conical, paraboloid and flat punch indenters, respectively). Oliver-Pharr method provides a method to determine the area function without performing the time-consuming imaging process. They assumed that the elastic modulus kept constant during indentation, and the total measured compliance follows the equation,

$$C=C_s+C_f \tag{2.5}$$

where C_s and C_f are the compliance of the specimen and the load frame, respectively. Substituting the Cs by 1/Er, Eq. 2.5 can be written as,

$$C = C_f + \frac{\sqrt{\pi}}{2E_r}\frac{1}{\sqrt{A}} \tag{2.6}$$

Eq. 2.6 tells that by plotting the C vs $A^{-1/2}$, a liner relation should be obtained. And the C_f is the intercept of the linear plot and this parameter is regardless of the reduced modulus. Therefore, if the calibration is done at a modulus-known material (with the measure C and calculated E_r), the contact area can be derived by rewriting Eq. 2.6 as,

$$A = \frac{\pi}{4}\frac{1}{E_r^2}\frac{1}{(C-C_f)^2} \tag{2.7}$$

And then the area function can be fitted to the equation below to derive the relation between contact depth and contact area,

$$A = \sum_{n=0}^{8} C_n(h_c)^{2^{1-n}} = C_0h^2 + C_1h + C_2h^{1/2} + C_3h^{1/4} + \cdots + C_8h^{1/128} \tag{2.8}$$

where C_0 to C_8 are the fitting constant while C_0 should be around the ideal value of 24.56. With the help of Eq. 9, the contact area during indentation at any depth can be obtained, so are the

hardness and modulus of the material according to Eq. 2.1-2.3.

However, the process mentioned above relies on the stiffness derived at the peak load, which means that one indentation test can only acquire one stiffness data, thus only the hardness at peak depth is available. This heavily inhibits the efficiency of nanoindentation work. In contrary, the continuous stiffness measurement (CSM) is much more effective and can record the stiffness data continuous with the increasing indentation depth. The CSM method is accompanied by the superposition of a high frequency amplitude (typically 45Hz with 2nm magnitude).

2.8.2. Indentation size effect

Nanoindentation experiments often exhibit pronounced depth dependence of measured hardness, i.e., the hardness decreases with increasing indentation depth, which is well-known as ISE [80]. The ISE accompanying the nanoindentation testing increases the difficulties to acquire accurate estimates of bulk hardness. It was proposed that the geometrically necessary dislocations (GND), induced by the strain gradients in the shallow indentations, contributed to the increasing hardness [81,82]. And both the statistically stored dislocations (SSD), created by homogenous strain, and GND contributed to the flow stress [83]. Therefore, it is imperative to account for these two dislocation types for comprehensive understanding of the hardening mechanism and indentation size effect.

Nix and Gao [10] developed a model to take ISE into account when evaluating the nanoindentation measured hardness. In this model, there are two assumptions. One is that dislocations that are necessary to accommodate the plastic deformation are all in a spherical volume with a radius equal to the contact radius as illustrated in Fig. 2.13. And the GNDs density can be derived as follow,

$$\rho_G = (3tan^2\theta)/2bh \tag{2.9}$$

where θ is the angle between the indenter surface and the original sample surface, b is the Burger's vector, and h is the indentation depth. This equation physically describes the ISE, i.e., the GNDs density increases with the decreasing depth thus increasing the hardness. The other assumption is that the total dislocation density is the linear sum of the density of GNDs and SSDs (ρ_T=ρ_G+ρ_S). The GNDs are responsible to the extra hardening that increases with the decreasing depth, while the SSDs provide the macroscopic hardness when there is no ISE. The hardening effect from both GNDs and SSDs is related to the flow stress based on the equation below,

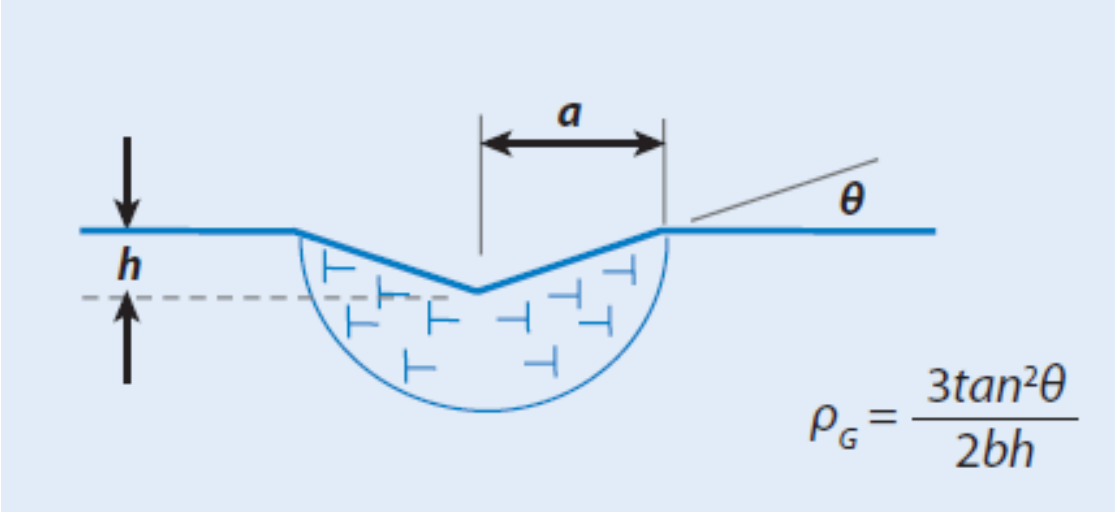

Fig. 2.13 Schematic diagram of the Nix-Gao model. The GNDs are assumed to reside in a hemispherical volume beneath the indenter. Reproduced from Ref. [80]

$$\sigma = \sqrt{3}\alpha G b\sqrt{\rho_T} \tag{2.10}$$

where α is the dislocation barrier strength, G is the shear modulus, and b is the Burger's vector [10]. Tabor's relation [6] is then used to correlate the flow stress to the hardness,

$$H=3\sigma \tag{2.11}$$

Combining the Eq. 2.9-2.11, a widely used Nix-Gao model description of the nanoindentation hardness can be written as

$$\frac{H}{H_0} = \sqrt{1 + \frac{h^*}{h}} \tag{2.12}$$

where H is the measured hardness, $H_0 = 3\sqrt{3}\alpha G b\sqrt{\rho_S}$ is the hardness in the infinite depth, h is the indentation depth and h^* is the characteristic length which is dependent on the materials and the indenter shape. This model has been frequently applied to correct for the ISE and enables an estimate of the bulk equivalent hardness H_0 from raw nanoindentation data. According to Eq. 2.12, by plotting H^2 vs. $1/h$, the intercept is H_0^2 and the slope is related to the ISE scale parameter h^*, just as shown in Fig. 2.14a. The data before about 100 nm was excluded considering the loss of self similarity of the indenter shape and the uncertainties in contact area at very small depths.

Although Nix-Gao model provide a physically meaningful method to extract reasonable bulk equivalent hardness, some researchers have questioned the validity of Nix-Gao model assumptions at shallow indentation depths [80,84–86]. As shown in Eq. 2.9, when indentation depth is small the density of GNDs is extremely large. This close dislocation spacing can induce a high level of mutually repulsive forces between the dislocations, which would drive them to expand beyond the small hemispherical volume [84]. Therefore, the Nix-Gao model may overestimate the density of GNDs that can actually be present at small indent depths and thereby predict a higher modeled hardness than the actual (measured) nanoindentation hardness at very shallow depths. Other investigations argued that the deviation is from the CSM method itself especially in the soft metals at small depths (<100 nm) [87,88]. However, there is not consistent idea about the breakdown of the Nix-Gao model in the shallow depths. More studies on both experiments and simulations should be conducted.

Feng and Nix [89] added a parameter f in Nix-Gao model in order to account for the possible expansion of the volume for GNDs at small depth due to the repulsive forces. Here they proposed that f is dependent on the depth. Their model is based on the equation below,

$$\frac{H}{H_0} = \sqrt{1 + \frac{h^*}{f^3 h}} \tag{2.13}$$

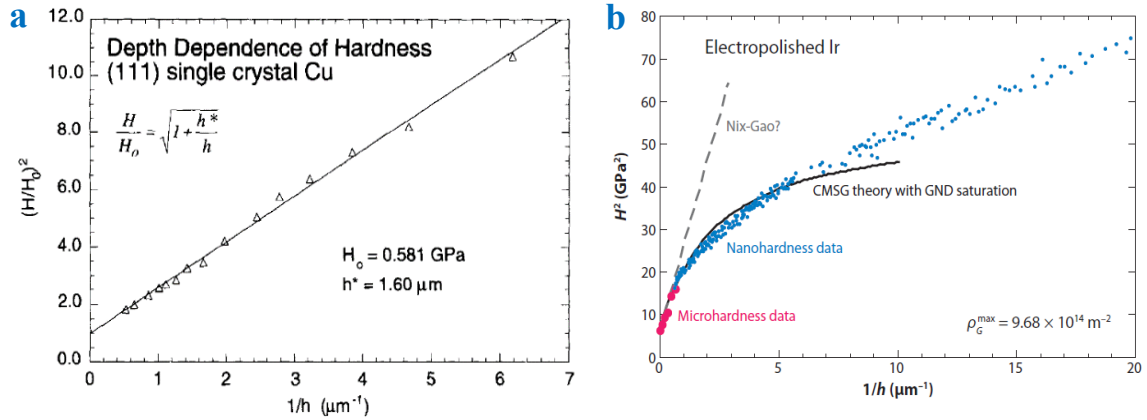

Fig. 2.14 (a) Depth dependence of the hardness of (111) single crystal copper after applying Nix-Gao model [10]. (b) Depth dependence of hardness of Ir. The Nix-Gao model breaks down at small depth [84].

where f is assumed to be $f = 1 + re^{-h/h_1}$, and r and h_1 are fitting parameters. Using this modified model, they found an expansion on the plastic zone radius is up to 66% when the indentation depth approached zero. But a problem about this model is that the function of f is artificially defined, and
the physical meaning of this definition is not clear. There are also other studies that assumed the parameter f is independent on the depth. Durst et al. [88] did not give the specific equation about f but just defined it as 1.9 corresponding to a plastic strain of 1.5%. They proposed that f is material dependent and should be a constant for a specific material. They also found a single f parameter can be used to fitting the nanoindentation data elsewhere in the study of the Ni-Fe alloys [90].

Another modification on the Nix-Gao model was proposed by Huang et al. [85] who introduced a parameter ρ_G^{max} to represent the saturation of GND density below a critical indent depth h_{nano}. They performed both analytical and finite element simulation work on modifying the Nix-Gao model. Although the concept of a maximum density of GNDs is physically reasonable [80], the practical use of their method depends heavily on the empirical value of ρ_G^{max}, which degrades the objective physical value of this modification.

2.8.3. Pileup effect

The Oliver-Pharr method [5] has been widely used to derive the depth-dependent hardness and modulus from load-displacement nanoindentation data from Eq.3-5. This method did not account for pileup effects along the periphery of the indented region, and was derived based on a purely elastic contact model where sink-in is pronounced [91], as described by the factor $\varepsilon P/S$ in Eq. 2.4. However, for the elastic-plastic materials, the pileup is usually observed as shown in Fig. 2.15 [92], and this upward flow of material increases the projected contact area of the sample with the indenter. Such pileups would generally be expected to appear in relatively soft metals (high elastic modulus to yield strength ratio, E/σ_y) with low work hardening capacity. Ignoring the pileup effect results in underestimating the contact area during nanoindentation tests, thus causing an overestimation of hardness and modulus according to Eq. 2.3 and 2.4. The simulation work performed by Bolshakov et al. [91] provides a good criterion to determine the necessity of performing pileup corrections. For materials with a sufficiently high value of E^*/H and little or no work hardening capacity, the pileup is pronounced as illustrated in Fig. 2.16.

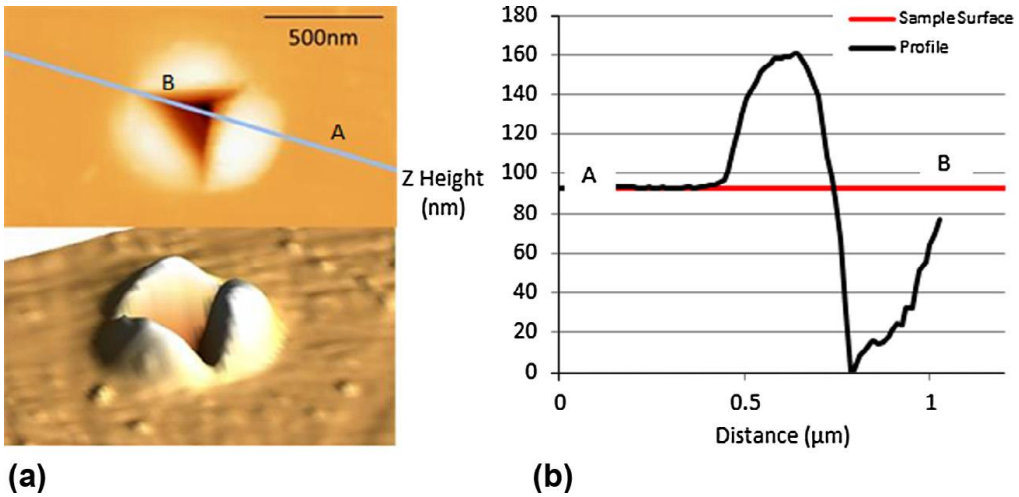

Fig. 2.15 (a) AFM tomography of a 200 nm depth indent with a cube corner tip in an irradiated region of Fe12Cr. (b) The height profile along the line section. Reproduced from Ref. [92].

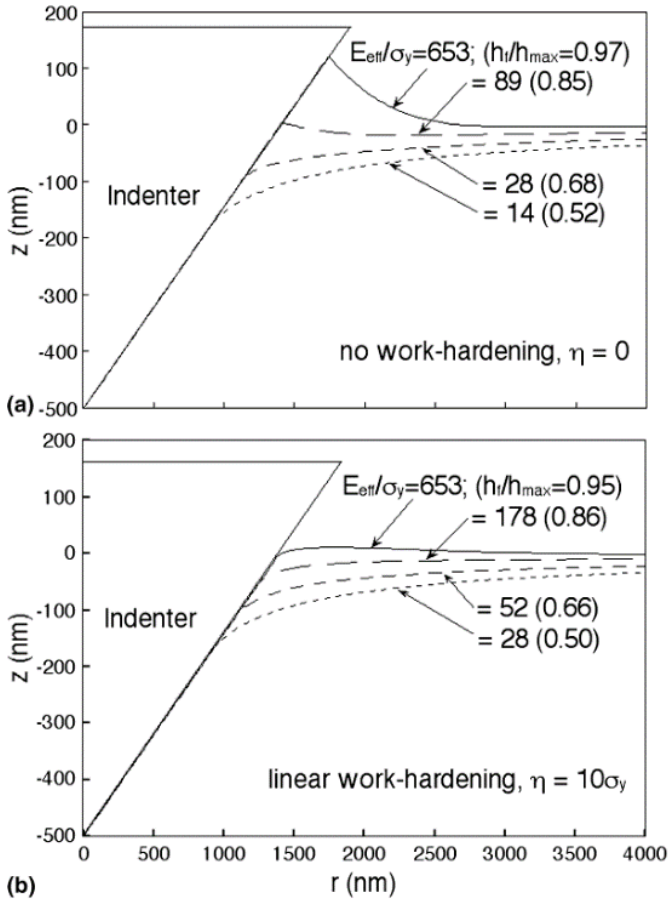

Fig. 2.16 Finite element simulation of contact profiles under load for conical indentation of (a) non-work-hardening materials and (b) linear work-hardening materials with work-hardening rate $\eta=10\sigma_y$. Reproduced from Ref. [91].

A much simpler parameter for the identification of significant pileup effect is the ratio of h_f/h_{max}, where h_f is the final depth after unloading and h_{max} is the maximum depth during loading. A h_f/h_{max} ratio close to 1 and small work hardening strongly promote the occurrence of pileup. Especially, Bolshakov et al. studied the dependence of the ratio of h_f/h_{max} on the normalized contact area, A/A_{sf} , as shown in Fig. 2.17. The term A_{true} refers to the contact area determined directly from the finite element simulation, while $A_{O/P}$ means the calculated contact area at the maximum depth by Oliver-Pharr method. A ratio of A/A_{sf} larger than 1 indicates the pileup effect, while sink-in effect dominates when this ratio is less than 1. They found that when h_f/h_{max} is larger than 0.7, the work hardening capacity plays a significant role in precise evaluation of the contact area whereas pileup effects were minor for $h_f/h_{max} < 0.7$. Therefore, great attention should be paid to the ratio h_f/h_{max} and work hardening characteristic of the materials when using nanoindentation to investigate the mechanical properties.

Considering the effect of pileup, a significant attention should also be paid to the definition of the contact depth. Eq. 2.4 includes the sink-in effect, instead of the pileup. For a better quantification of the depth, the sink-in term, $-\varepsilon P/S$, should be replaced by the pileup induced height. In another word, h_c should be set equal to h followed by pileup corrections. Defining A_c, H_c and E_c as the pileup-corrected contact area, hardness and modulus, respectively, the correction factor C follows the relation below [92],

$$C = \frac{A}{A_c} = \frac{H_c}{H} = \left(\frac{E_c^*}{E^*}\right)^2 \tag{2.14}$$

The way to perform the pileup corrections either through the left side of Eq. 2.14, i.e., correcting the contact area [93,92], or from the right side, i.e., correcting the modulus [94].

Kese et al. [93,95] developed a semi-elliptical method to account for the increased contact area due to pileup. Fig. 2.18 illustrates their method of AFM based calculation for the projected contact area. The contact perimeter is estimated as a semi ellipse with a half-short axis of a_i which is defined as the horizontal distance from the edge of the indent to the actual contact periphery. According to the method by Kese et al., the sum of the pileup projected contact area from three sides of the indent can be written as,

$$A_{pu} = \frac{\pi b}{4} \sum a_i \tag{2.15}$$

where b is the side of the Berkovich indenter equilateral triangle residual impression with the area of $b^2\tan 60^\circ/4$. After accounting for the pileup effect, the corrected contact area can be written as below:

$$A_c = A + A_{pu} \tag{2.16}$$

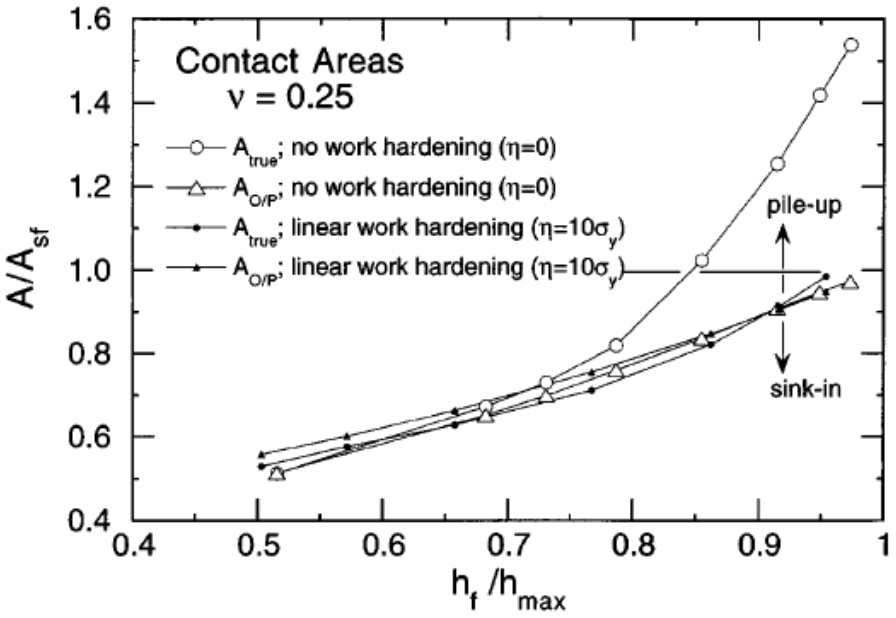

Fig. 2.17 Simulation results of the normalized contact areas variation with the ratio of h_f/h_{max}. Reproduced from Ref. [91].

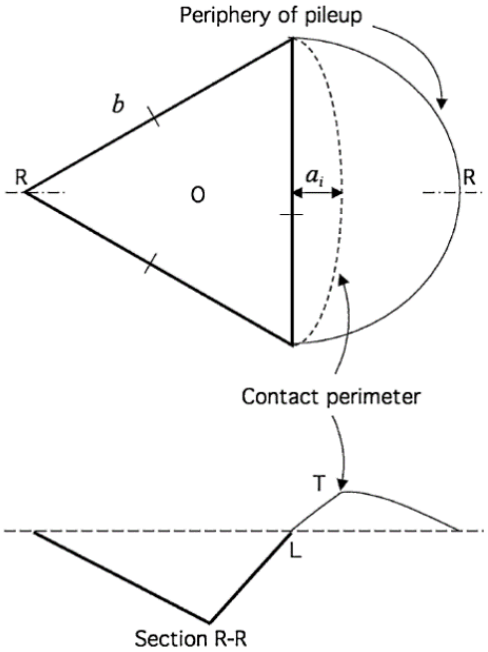

Fig. 2.18 The schematic diagram of the indent and the cross section. The parameter a_i represents the half short axis of the semi ellipse estimated as the contact periphery of the indenter with material. Reproduced from Ref. [93].

where A is the area function calibrated on fused silica before testing. The indenter contact area A is related to b by the following equation:

$$A = \frac{b^2}{4}\tan 60^\circ \tag{2.17}$$

Therefore, combining Eq. 2.15-2.17, the corrected contact area can be described in the following equation,

$$A_c = A + 5.91 h_c \sum a_i \tag{2.18}$$

Combining Eq. 2.14 and 2.18, the hardness and modulus can be corrected for pileup effects in a straightforward way. Hardie et al. [92] also performed pileup correction through the ratio of the calibrated contact area and the corrected area. But they measured A and Ac directly under SEM. This method is much more straightforward while it is not suitable to apply in the CSM method since only the data at the peak depth can be corrected. Since modulus is a constant parameter during nanoindentation, Heintze et al. [94] used ultrasonic pulse-echo technique to correct the modulus and then obtained the correction factor. Their method is based on the equation below,

$$\nu = \frac{1-2(\frac{c_T}{c_L})^2}{2-2(\frac{c_T}{c_L})^2} \tag{2.19}$$

$$E = \rho c_L^2 \frac{(1+\nu)(1-2\nu)}{1-\nu} \tag{2.20}$$

where c_L and c_T are the sound velocity of longitudinal and transverse waves, respectively. ρ is the material density. Eq. 2.20 tells the corrected modulus, then the correction factor can be derived through the Eq. 2.14.

2.8.4. Nanoindentation on ion-irradiated samples

The most important challenge to apply nanoindentation into ion-irradiated samples is the shallow damage layer and gradient dpa level in the materials. It is well known that the plastic zone beneath the indenter is much larger than the indent depth, which means a small indent can sense the different dose and dose rate in the ion-irradiated samples [96,97]. Fig. 2.19 illustrates the deformed region under the indenter. This strain field consists of a core region with a radius of a, the equivalent radius of the indent impression, and the other regions with decreasing strain. The strain region where the 0.2% strain is achieved is defined as the boundary of the plastic region. Johnson et al. [97] proposed an equation to describe the size of the plastic zone as below,

$$\left(\frac{c}{a}\right)^3 = \frac{1}{3tan\theta}\frac{E}{\sigma_{ys}} \tag{2.21}$$

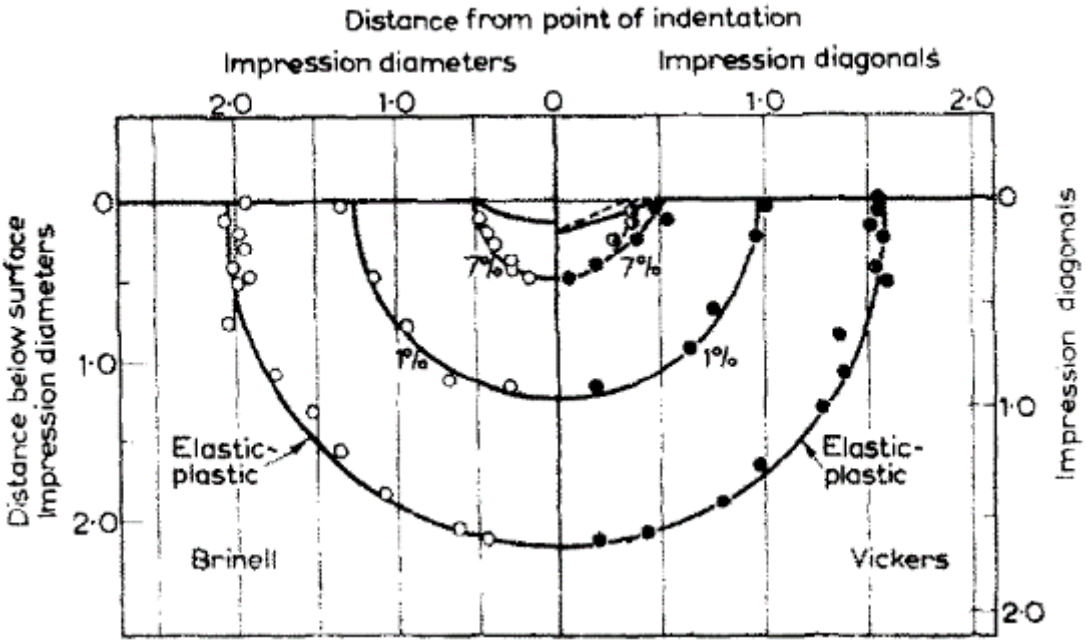

Fig. 2.19 The deformed region under a Brinell-ball and Vickers-pyramid indenters. The hemi circle lines represents different strain levels. Reproduced from Ref. [96].

where c the radius of the plastic zone, θ is the semi including angle of the conical indenter, E is the Young's modulus, and σ_{ys} is the yield stress. It is clear that the plastic zone depends on the material properties, indenter shape, and the indentation depth. It was also found that crystal orientation affects the deformed size beneath the indenter [98].

For the nanoindentation experiment on ion-irradiated materials, a typical plastic zone that extends beyond 5-10 times the indent depth is usually assumed [99,100]. Therefore, the region available for extracting bulk equivalent hardness is limited in several hundreds of nanometers since the heavy ion irradiation generally cause damage layer up to several micrometers. When indenting on the normal surface of the material along the direction of incoming ions as shown in Fig. 2.20a, the indenter can sense a wide range of the damaged layer with inhomogeneous dose profile. Given that the total damaged region is 2 μm (e.g., typically for 8 MeV Fe^{2+} irradiation), there will be only a depth range less than 200-400 nm available for extracting nanoindentation hardness of the irradiated material. Beyond this narrow region, the unirradiated substrate larger than 2 μm starts to contribute to the hardening component. A possible way to avoid the inhomogeneous dose profile is to indent on the cross section of the material, i.e., along the direction vertical to the ion fluence as illustrated in Fig. 2.20b. In this method, the damage level beneath the indenter is much more constant than the normal indentation. Thus, the measured hardness can be better associated with a specific dose and dose rate, which provides clearer understanding of the irradiation effect on the mechanical properties. Although cross section indentation avoids the substrate effect, the indentation depth can not approach to a large extent due to the limited total irradiation region. As is known widely, the size or the equivalent radius of the indent impression is much larger than the indent depth. For a Berkovich indenter, the side length of the triangle indent is about 7.5 times to the indent depth. And the diagonal of Vickers indent is larger than the depth by a factor of 7. Under this circumstance, a 300 nm in indent depth will cause an indent size larger than 2 nm, indicating that only limited indents can be made in the whole damage region to avoid sense the unirradiated region. And the neighboring distance required to avoid the interference further limits the total number of indents.

The reflection of the substrate effect on the nanoindentation measure hardness is the bilinear curve in the H^2 vs. $1/h$ plot. Kasada et al. [101] applied the film/substrate model to the ion irradiated sample, and used the bilinear fitting of Nix-Gao model to extract the bulk equivalent hardness in the irradiate region. Fig. 2.21 shows the Nix-Gao plot with a clear inflection on the irradiated samples at around 330 nm. The multiplication factor between the

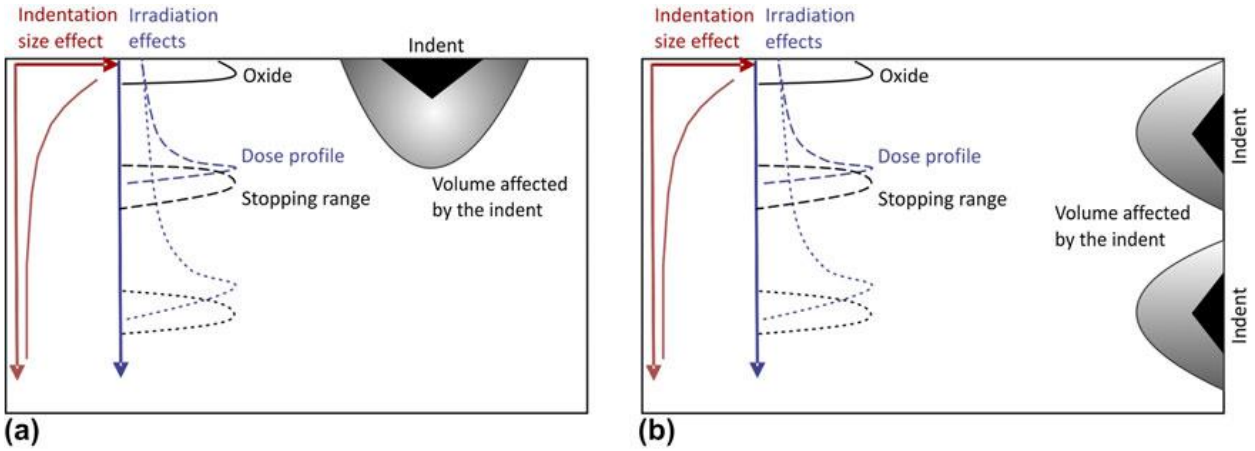

Fig. 2.20 The schematic diagram of (a) normal nanoindentation along the direction of the incoming ion beam, and (b) cross section nanoindentation on the sample surface vertical to the irradiation direction. Reproduced from Ref. [102]

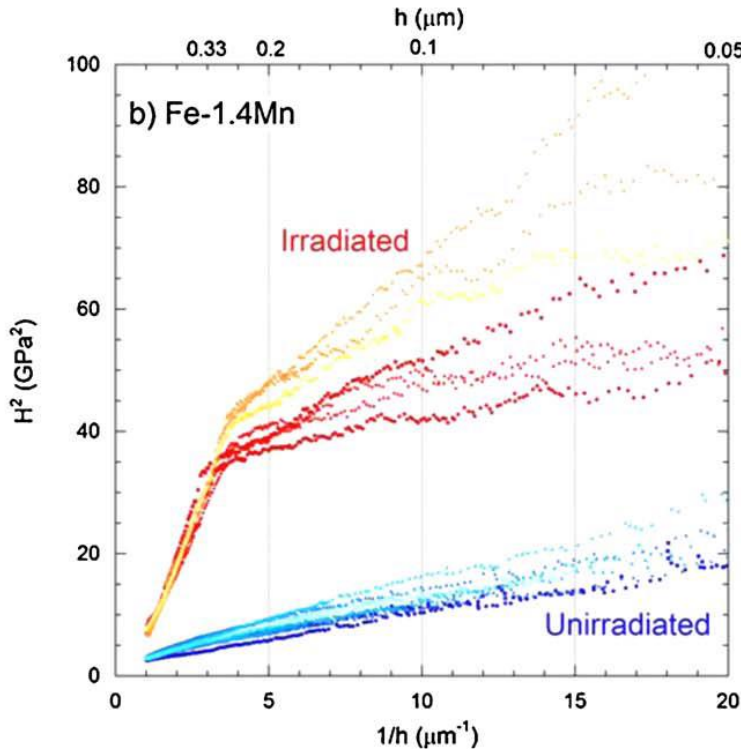

Fig. 2.21 Nix-Gao plot of Fe-1.4Mn before and after 6.4Mev Fe^{3+} ion irradiation at 290 ℃. Reproduced from Ref. [101].

inflection point and the total irradiation depth is rightly in the range of 5-10. By linearly fitting the data in the range less than 330 nm, H_0 and h^* for the irradiated specimen can be obtained from the intercept and the slope of the fitting. While the linear fitting beyond 330 nm results in a combined hardness from both substrate and irradiated part, which has unclear physical meaning. Although the bilinear fitting has been widely used in the ion irradiation study, there are still varied questions about the validity of this method. It was argued that the bilinear characteristics, or the curvatures in Nix-Gao plot, is an artifact originating from CSM technique itself [80], or at least is affected by the CSM method. Investigations on different uniform materials, both control and neutron-irradiated, has observed curvatures at shallow indentation depth, i.e., the experimental data deviates the Nix-Gao fitting [94,103–105]. Therefore, it may be not appropriate to state that the inflection on the Nix-Gao plot is totally form the substrate effect. More studies are needed to quantify the effect of the intrinsic deviation at small depth when using CSM method. Pharr et al. just recommended that non-CSM method should be used for nanoindentation on ion-irradiated samples [80].

CHAPTER 3. MATERIALS AND METHODS

The motivation of this study is to build up the connection between nanoindentation measured hardness and the macro mechanical properties, as well as comprehensively understand the microstructural model predictions of hardening. Therefore, various materials with different heat treatment and irradiations are included in this study. The binary Fe-Cr alloy were thermally aged to investigate the hardening effect from Cr-rich α' precipitates solely. The single ion-irradiated Fe-Cr model alloys were used to study the hardening contributions from both the Cr-rich α' precipitates and dislocation lines/loops. Later the dual ion and neutron irradiated commercial alloy, i.e., T91 and HT9, were studied for the hardening effect of helium bubble, dislocation loops, etc.

3.1. Materials and sample preparation

3.1.1. Thermally aged binary Fe-Cr alloys

High purity Fe and Fe-Cr binary alloys were provided by Dr. Jean Henry of Université Paris-Saclay, France. They were fabricated and homogenized at around 850 ℃ for 1 hour for this study. The chemical composition and grain size of the investigated materials are listed in Table 3.1. The as-received materials were cut into discs with diameter of 3 mm and thickness of 1 mm before thermal aging and mechanical polishing. A portion of the Fe-Cr alloys were then sealed into glass tubes under high purity nitrogen gas atmosphere and subjected to thermal annealing for 100, 300 and 900 hours at 475 ℃. Subsequently, all the as-received and thermally aged samples were mechanically grounded by silica paper, followed by polishing with diamond and colloidal silica suspension of size down to 0.05 μm. Additionally, electropolishing was also performed on some specimens to remove the potential work-hardened surface layer produced by mechanical polishing. Electropolishing was conducted on the 900-hour aged Fe18Cr and 100-hour aged Fe25Cr samples with 4% perchloric acid and 96% ethanol under 30 V, -50 ℃ for 10-30 seconds.

3.1.2. Ion irradiated binary Fe-Cr alloys

The high purity Fe18Cr binary alloys were fabricated and provided by CEA, under the European Fusion Development Agreement (EFDA) program. Before irradiation, mechanical grounding with silica papers was performed, followed by polishing with colloidal silica

Table 3.1 The chemical composition and grain size of the as-received materials.

	Cr	C(ppm)	S(ppm)	O(ppm)	N(ppm)	P(ppm)	Grain size(μm)
Fe	<2 ppm	4	2	4	1	<5	183
Fe3Cr	3.05 wt.%	<4	<2	<6	<2	-	390
Fe5Cr	5.40 wt.%	4	3	6	2	5	68
Fe8Cr	7.88 wt.%	<6	<1	<6	<2	-	320
Fe10Cr	10.10 wt.%	4	4	4	3	<5	82
Fe12Cr	11.63 wt.%	<5	<2	<4	-	-	500
Fe14Cr	14.25 wt.%	5	7	4	5	<10	141
Fe18Cr	17.97 wt.%	7	2	6	5	-	650
Fe25Cr	24.97 wt.%	4	1	3	3	-	570

suspension of size down to 0.05 μm to achieve a mirror surface.

The polished Fe18Cr specimens were irradiated in the Michigan Ion Beam Laboratory (MIBL) with the 3 MeV Tandem particle accelerator Wolverine. A defocused beam of 8 MeV Fe^{2+} ions was used for irradiation at temperatures of 300, 350, and 450 °C, and fluences of 8.8×10^{14} and 8.8×10^{15} ions/cm^2. Table 3.2 presents all the irradiation conditions. The temperature during irradiation was measured by the thermocouple attached to part of the samples, and simultaneously monitored by a 2D thermal imager to guarantee the temperature variation less than 6 °C. Fig. 3.1 shows the SRIM calculated damage profile for the Fe-Cr alloys. A wide damaged region of ~2 μm was achieved for this study. The doses of 0.37 and 3.7 dpa were determined in the mid-range (~1 μm) as shown in the shadow region. The calculation was conducted using the SRIM code in full-cascade mode using the damage energy method (as recommended by Ref. [106]) with a displacement energy of 40 eV.

3.1.3. Dual ion and neutron irradiated T91 and HT9

Alloy T91 and HT9 after dual ion and BOR 60 neutron irradiation were received from University of Michigan. The dual ion irradiated specimens were in bar shape with 10 mm × 1mm × 1mm for L×W×H, and the BOR 60 specimens were small discs with diameter of 3 mm and thickness of 0.5 mm. The details about the samples can be found elsewhere [24,107,108]. Table 3.3 shows the chemical compositions of T91 provided by Pacific Northwest National Laboratory (PNNL) and Luvak Inc. [107], and those of HT9 taken from Ref. [24] . For the ion irradiation, the HT9 and T91 specimens were irradiated at MIBL with co-injected Fe ions and helium ions to produce the displacement damage and cavities for simulating the process in neutron irradiation. 9 MeV Fe^{3+} ions with a dose rate of ~7.5×10^{-4} dpa/s and 3.42 MeV He^{2+} ions were used to produce target dose at around 1000 nm depth. Table 3.4 presents all the irradiation conditions. Fig. 3.2 shows the calculated damage profile using SRIM with the quick Kinchin-Pease mode. This method induced less than ~10% discrepancy in calculation of vacancy production compared with Full-cascade method for Fe ion irradiation on pure iron [106]. Since the discrepancy is minor and to keep consistent with the dose calculations by collaborators in the same project [24,36,109,110], we used the quick Kinchin-Pease method to calculate the nominal target dose on T91 and HT9 materials. A displacement of energy of 40 eV was used. The temperature control for dual ion irradiation is similar to the procedure as described in section 3.1.2. Table 3.5 summarizes the target irradiation conditions for BOR 60

Table 3.2 The irradiated conditions for Fe-Cr alloys.

Final dose (dpa)		0.37			3.7
Temperature (°C)	300	350	450	350	450
10^{-3} dpa/s	√	√	√		
10^{-4} dpa/s	√	√	√	√	√
10^{-5} dpa/s			√		

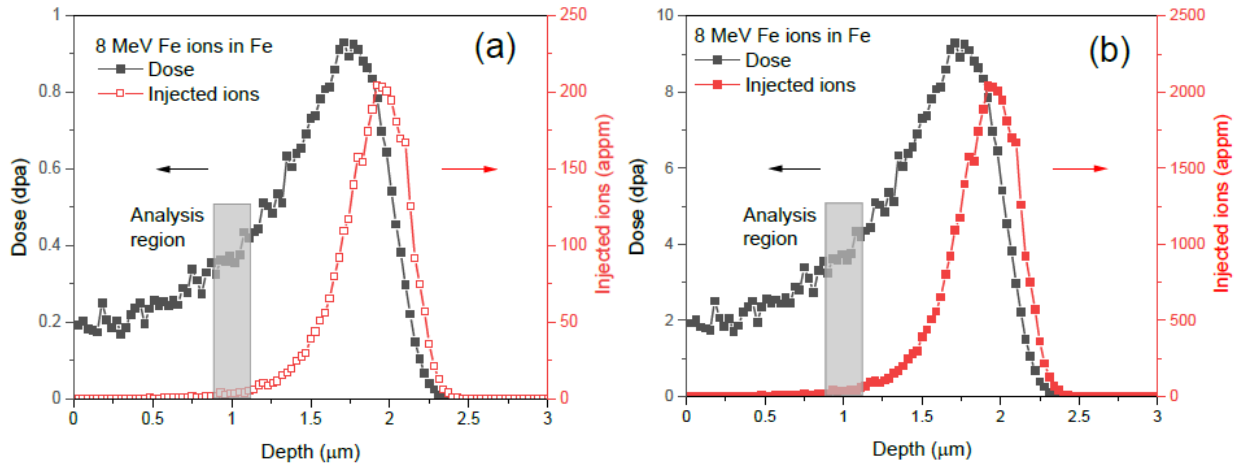

Fig. 3.1 SRIM calculation of the damage profile for 8 MeV Fe^{2+} ions irradiated Fe-Cr alloys with fluence of (a) $8.83x10^{14}$ ions/cm^2 and (b) $8.83x10^{15}$ ions/ cm^2. The shadowed region is used to determine the dose and for microstructure analysis.

Table 3.3 The chemical compositions (wt.%) of as-received T91 and HT9. The balance composition is Fe.

Materials		C	N	Al	Si	P	S	Ti	V	Cr	Mn	Ni	Cu	Nb	Mo	W
T91	PNNL	.08	.054	-	.11	-	-	-	.21	8.8	.37	.09	-	.072	.89	-
	Luvak	.091	.052	.004	.25	.007	.002	.003	.23	8.76	.37	.10	.062	.086	.86	.004
HT9		.21	.01	-	.21	.008	.003	-	.33	11.8	.50	.51	-	-	1.03	.50

Table 3.4 The dual ion irradiation conditions for the T91 and HT9.

Materials	Irradiation temperature (℃)	Dose (dpa)	He (appm)	He/dpa ratio
T91	445	16.6	72	4.3
	520	16.6	72	4.3
HT9	445	72	309	4.3
	520	16.6	72	4.3

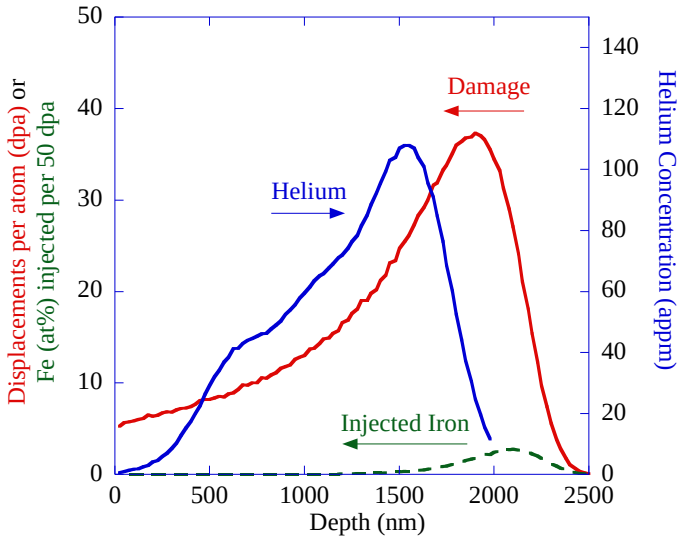

Fig. 3.2 The SRIM calculation of the damage profile for HT9 sample irradiated with 9 MeV Fe^{3+} and 3.42 MeV He^{2+} ions to 16.6 dpa.

Table 3.5 The BOR 60 neutron irradiation conditions for the HT9 and T91.

Materials	Irradiation temperature (°C)	Dose (dpa)
T91	376	18
	462	17
HT9	459	31
	462	17

samples. The neutron irradiation was performed at BOR 60 fast fission reactor with dose rates of 6-9 × 10^{-7} dpa/s. Each neutron irradiation contained several cycles. The temperature variation was controlled with 10 ℃ and the target doses were calculated by the integration of the displacement cross section and the reactor neutron energy spectrum [107].

3.2. Methods

3.2.1. Mechanical testing

For thermally aged FrCr alloys, The nanoindentation hardness was measured at room temperature with an iMicro (KLA, former Nanomechanics) nano indenter with a Berkovich tip. Before testing, indenter tip calibration was performed on a fused silica sample using the Oliver-Pharr method [5]. Both constant strain rate (CSR) and constant loading rate (CLR) methods were performed on multiple alloys to compare the measured hardness obtained from these different testing processes. For the CSR method, the nanoindentation tests were performed with continuous stiffness measurement (CSM), which can record the modulus and hardness continuously during the loading portion. Twenty-five indents were performed as a 5×5 square matrix pattern for each specimen to obtain the average modulus and depth-dependent hardness with a peak loading penetration depth of 1000 nm. Three strain rates were investigated: 0.05, 0.2 and 0.5 /s, with the superposed CSM oscillation of 2 nm at 45 Hz. Tests were also performed with CSM oscillation frequency of either 110 Hz for the highest strain rate to investigate potential artifacts on the measured stiffness (elastic modulus) associated with interference between the lock-in amplifier and some component of the semi-static loading. The CLR tests were performed using a constant loading rate of 0.2 mN/s, and 10 indents were conducted for each target load in the range of 2 mN-12 mN. The distance between neighboring indents was set as 40 μm for both the CSR and CLR tests to avoid interference from adjacent indents. Nanoindentation data obtained at depths below 100 nm were generally excluded from analysis due to relatively large statistical variability, most likely due to slight surface roughness variations [80] and reverse indentation size effects [101]. For the grain orientation study, EBSD was used to identify sample grains with low index orientations, which were marked and then tested by nanoindentation at a constant strain rate of 0.05 /s. For the metals investigated in this study, the indentation contact depth (h_c) was set equal to the total depth (h), considering that there were no sink-in effects.

Vickers hardness was measured at room temperature with a Buehler Tukon model 1102 microhardness tester with 1 kg dead-weight load with 10 s dwell time to investigate its

correlation with the nano hardness measurements. Both indent diagonals were measured for each indent at a magnification of 50X and automatically converted to Vickers hardness using instrument-supplied software. The Vickers hardness values were obtained by taking the average of 10 indents on each sample.

For single ion irradiated Fe18Cr alloys and dual ion irradiated T91 and HT9, iMicro nano indenter were also used with the same constant strain rate (0.05 /s) test method as the thermally aged samples. For neutron irradiated T91 and HT9, nanoindentation was performed with a G200 nano indenter at the Low Activation Materials Development and Analysis (LAMDA) Laboratory.

3.2.2. Atomic force microscopy

To quantify the amount of plastic-flow pileup associated with the indentations, additional nanoindentation tests with peak depths of 200, 400, 600, 800 and 1000 nm were conducted using the CSM method at a constant strain rate of 0.05 /s. Five indents were performed in a line for each depth with an indent spacing of 40 μm. Atomic force microscopy (AFM) was used to characterize the surface topography and measure the pileup height along each side of the residual impression.

3.2.3. Atom probe tomography

Atom probe needles were lifted out and sharpened using focused ion beam (FIB) techniques with a FEI Nova 200 instrument. The APT dataset acquisitions were performed with a CAMECA LEAP 4000X HR atom probe using a 50K base temperature, 20% pulse fraction and a detection rate of 0.5 %, and the datasets were collected using voltage mode for better spatial resolution. A solute concentration-based cluster searching algorithm was developed by our group and applied to characterize the α' precipitates. The threshold Cr concentration was set as 30 at. % to reduce the effect of natural fluctuation. The size, number density and volume fraction of α' phase were obtained from this method. The cluster and matrix Cr concentrations reported here are the core and lowest value measured from the proximity histograms generated with Integrated Visualization and Analysis Software (IVAS).

3.2.4. Transmission electron microscopy

For Fe ion-irradiated Fe18Cr alloys and dual-ion irradiated T91 and HT9 alloys, the TEM

specimens were prepared with focused ion beam (FIB) using a Zeiss Auriga scanning electron microscope at the Institute for Advanced Materials and Manufacturing (IAMM). Electron beam scattering diffraction (EBSD) was performed to guarantee that the FIB lamella was lifted out near [100] zone axes. The initial trenching voltage of Ga ions was 30 kV, followed by milling with 2 kV as the final polishing energy to reduce the FIB damage. To achieve a high-quality TEM specimen, the FIB polished specimens were subsequently electropolished with 3% perchloric acid and 97% ethanol under 48 V, -65 °C for 20 milliseconds. For BOR 60 reactor irradiated T91 and HT9 alloys, the FIB work was performed by FEI Quanta 200i at LAMDA.

The JEOL 2100F TEM at LAMDA was used to characterize the dislocation loops on the investigated materials. The precipitates and radiation induced segregation was characterized by EDS mapping and energy dispersive spectroscopy on Talos TEM. A Zeiss Libra 200 TEM was used to characterize the irradiation-induced cavities using the under- and over- focus technique. The thickness of the investigated samples was estimated by electron energy loss spectroscopy (EELS).

There are two types of dislocation loops in the irradiated bcc alloys that are widely reported in the literature: <100> and ½<111> loops. In the current study, the TEM specimens were all tilted to [100] zone axis and imaged at STEM-BF conditions, which is an efficient way to identify the type of dislocation loops based on the prior studies [111,112]. Under [100] zone axis, 2/3 of the total <100> loops can be imaged as edge-on loops, while all the ½ <111> loops are visible if they exist. The images were taken from the sample surface down to beyond the irradiated region. Multiple images of each specimen in the mid-range were used for the quantitative analysis.

CHAPTER 4. RESULTS

4.1. Nanoindentation testing protocol on Fe and Fe-(3-25wt%)Cr alloys

The first research objective of this study is to develop a protocol for nanoindentation test on the ion-irradiated Fe-Cr alloys. Many prior published studies lack systematical research considering the effect of test procedures and data analysis method on the nanoindentation results, which can cause a significant inconsistency and errors in extracting accurate mechanical properties from nanoindentation tests. Especially for the ion irradiated materials with a shallow damaged layer, nanoindentation tests are of great importance since the conventional tensile tests are not suitable to acquire the bulk properties. In this Chapter, a variety of binary Fe-Cr model alloys subjected to thermal aging with chromium content from 3 wt.% to 25 wt.% were investigated using nanoindentation. The effect of test strain rates, test method, electropolishing and pileup on the nanoindentation results were carefully analyzed for a better understanding of accurate extraction of bulk mechanical properties.

4.1.1. Constant strain rate tests

Nanoindentation testing with a constant strain rate of 0.05 /s was performed on high purity Fe and Fe alloys containing 3-25 wt. %Cr in the as-annealed and aged conditions. To quantitatively compare the hardness, the Nix-Gao model as expressed in Eq. 1.1 was used to extract bulk equivalent hardness from the nanoindentation data. The ideal relationship of H^2 with $1/h$ should be linear according to the Nix-Gao model since the local hardness of the as-received and aged samples is uniform at length scales >~10 nm. However, there are clear curvatures for all tested materials in the region of shallow depth (h<~150nm; 1/h>0.006/nm) as shown in Fig. 4.1. This near-surface curvature is a potential issue when trying to accurately quantify hardness behavior at indent depths below ~150 nm and will be discussed later in this paper. In our linear fits of Nix-Gao plots of H^2 vs. $1/h$ we evaluated all data points in the range of h>100nm.

Fig. 4.2 summarizes the bulk equivalent hardness and characteristic ISE length extracted from the Nix-Gao fitting in Fig. 4.1. A sharp increase of hardness was observed in Fig. 4.2a for the Fe18Cr and Fe25Cr from the as-received condition to 300 h aging. For aging beyond 300 h, both Fe18Cr and Fe25Cr alloys exhibit only a slight additional increase in hardness (<10%). Conversely, 300 h thermal aging shows almost no hardness change for Fe14Cr. The characteristic ISE length scale parameter h^* depends on the sample material and is a useful

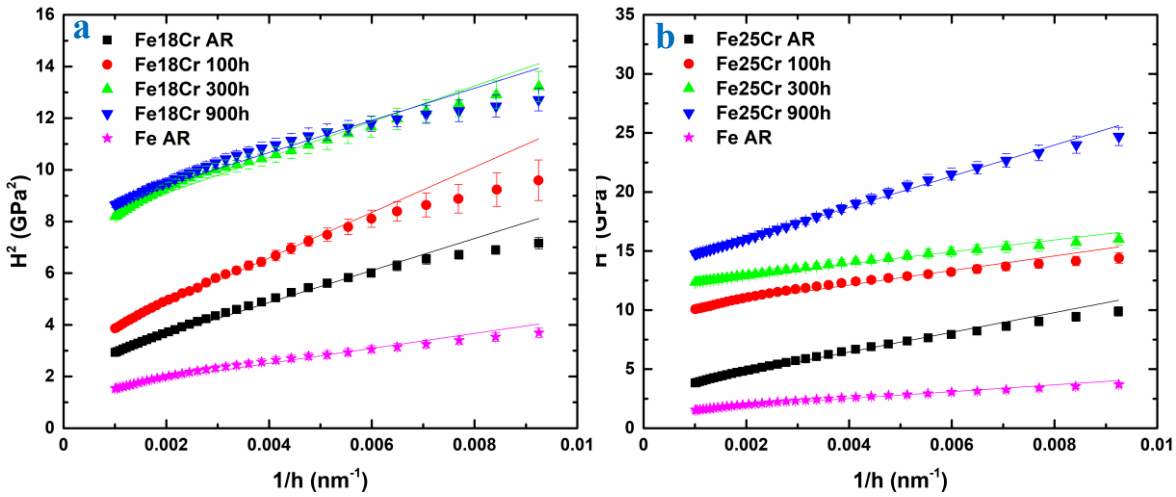

Fig. 4.1 Nix-Gao fitting of the depth dependent hardness for (a) Fe18Cr and (b) Fe25Cr in as-received and thermally aged conditions. The as-received Fe is listed as a reference in both figures.

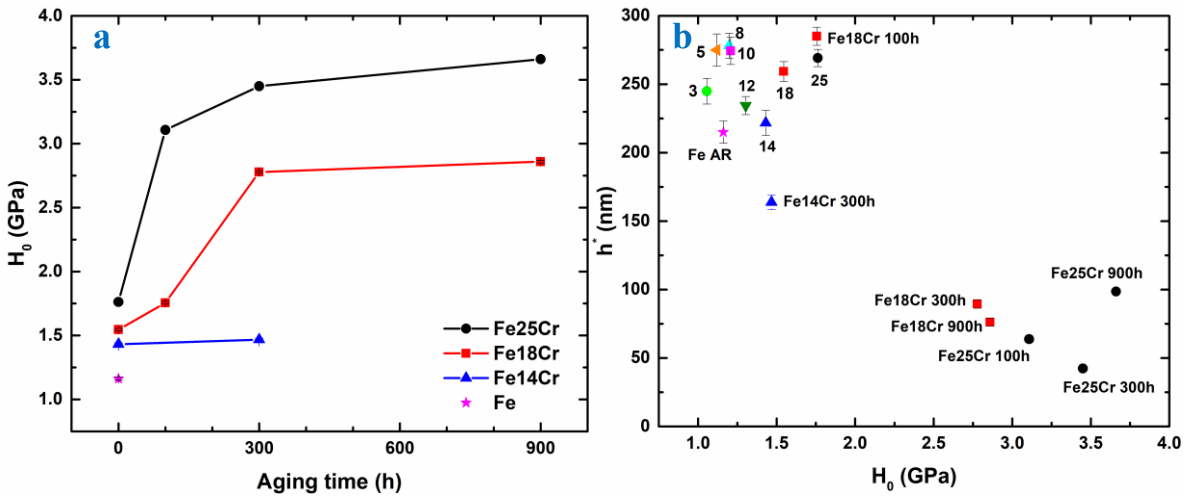

Fig. 4.2 (a) The variation of bulk equivalent hardness with the aging time. (b)The variation of characteristic ISE length with the bulk equivalent hardness of the investigated materials. The as-received Fe-Cr alloys are noted as numbers corresponding to the Cr concentration (wt.%).

parameter to quantify sensitivity to ISE. The variation of characteristic ISE length with hardness of the investigated materials can be observed clearly in Fig. 4.2b. As indicated from Eq. 2.12, higher h^* values require a larger indent depth h to reduce the depth sensitive term h^*/h to a negligible value, i.e., ISE is more prominent for large values of h^*. The value of h^* (ISE sensitivity) generally decreased with increasing hardness. However, there is no universal monotonic variation of h^* with bulk equivalent hardness for all the investigated materials. For example, the measured value of h^* is lower for the relatively soft as-received Fe, Fe12Cr and Fe14Cr materials compared to the relatively harder as-received Fe18Cr and Fe25Cr.

4.1.2. Effect of varying strain rate

In the current study, constant strain rate tests for nanoindentation with CSM method were performed at 0.05, 0.2 and 0.5/s to examine potential strain rate effects for a relatively weak material (pure Fe), intermediate strength conditions (as-received 18Cr and 25Cr alloys), and high strength conditions (aged alloys). A qualitatively similar ISE behavior was observed at all three strain rates for each of the tested materials. Table 4.1 summarizes the bulk equivalent hardness values obtained by applying the Nix-Gao model to the raw nanoindentation data. For pure iron, it is obvious that the hardness increases slightly with increasing strain rate. For Fe18Cr and Fe25Cr, the variation of hardness with aging time is nearly independent of strain rate. Generally, the magnitude of the bulk hardness variations with strain rate are all less than 10%, except for pure iron, for which the largest variation is 15%.

Fig. 4.3 shows the typical H^2 vs. $1/h$ curves of 900 h aged Fe18Cr used for applying the Nix-Gao model to nanoindentation results at strain rates of 0.05, 0.2 and 0.05 /s. By increasing the strain rate, the measured hardness of the investigated material increases correspondingly. However, the Nix-Gao model does not fit well with the experimental results at low indentation depths, manifested as clear curvatures up to indent depths near 250-300 nm. There is no evidence for a dependence of the onset of slope change on strain rate in the Nix-Gao plots for any of the nine investigated materials. Therefore, further experiments on other potential contributing factors, such as electropolishing (to remove near-surface mechanical polishing damage) and indenter pileup effects, were performed to explore potential causes of the Nix-Gao plot curvatures.

Table 4.1 Summary of the bulk equivalent hardness obtained from Nix-Gao model for different constant strain rates. AR refers to the as-received condition, and 900 h refers to the 475 °C aged conditions.

Hardness (GPa)	Fe	Fe18Cr				Fe25Cr			
	AR	AR	100h	300h	900h	AR	100h	300h	900h
CSR (0.05/s)	1.16	1.55	1.76	2.78	2.86	1.76	3.11	3.45	3.66
CSR (0.2 /s)	1.25	1.60	1.88	2.90	2.92	1.79	3.23	3.65	3.63
CSR (0.5 /s)	1.33	1.66	1.91	2.92	3.01	1.82	3.31	3.72	3.68

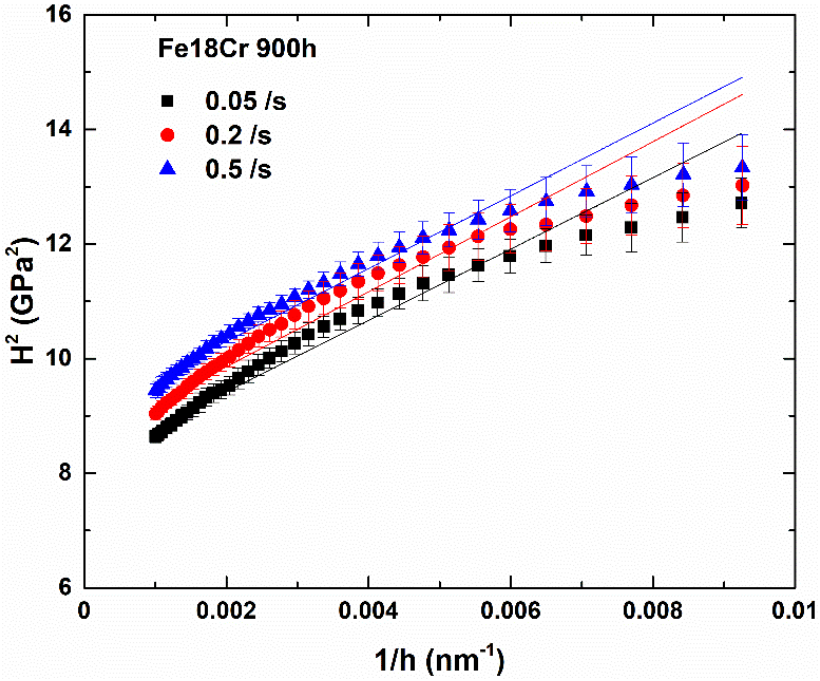

Fig. 4.3 The H^2 vs. 1/h curves of nanoindentation results for Fe18Cr aged for 900 h under different strain rates. The solid lines are linear fittings of the curves.

4.1.3. Constant loading rate tests

Both constant loading rate (CLR) and constant strain rate (CSR) methods have been extensively applied in nanoindentation experiments. In the conventional CLR test method, only a single hardness value is obtained from each indent at the maximum depth [113]. Conversely, with the use of continuous stiffness measurement (CSM) technique in CSR tests, the hardness variation with depth can be recorded continuously during the penetration of the indenter into the investigated materials [5]. Therefore, CSR method has been used increasingly in recent years. CLR method is still frequently applied mainly due to the inability of some nanoindentation instruments to achieve CSR test conditions, and some results that suggest the CSR method introduces increased errors at small depths especially for soft materials [80,87].

In the current research, nanoindentation tests were performed with both CLR (0.2 mN/s) and CSR (0.05/s) methods on as-received and 900 h aged Fe18Cr as well as 900 h aged Fe25Cr specimens. Fig. 4.4a shows that the measured nanoindentation hardness of a tested material for CSR and CLR test methods is comparable at any given depth, with a significant ISE. Compared with the CSR test, the CLR test induced much more statistic variability especially for 900 h aged Fe25Cr with the highest hardness. Due to the discrete and limited CLR data points, direct quantification of the linearity of the Nix-Gao fitting cannot be rigorously assessed for the CLR method in Fig. 4.4b. Further testing is needed to quantify whether any curvature occurs in the Nix-Gao plots for the CLR test method.

Table 4.2 summarizes the measured bulk equivalent hardness and indentation size effect scale parameter (h^*) of the investigated materials obtained from applying the Nix-Gao model. The ISE is distinctly larger for CSR compared to CLR test methods, whereas the bulk hardness values extracted from both methods are comparable to each other (within ~10%, slightly higher hardness for CLR). It is worth noting that the strain rate in the CLR test method varies during nanoindentation. Considering the indentation size effect and applying the Nix-Gao model, the strain rate $\dot{\varepsilon}$ can be described as below,

$$\dot{\varepsilon} = \frac{\dot{h}}{h} = \frac{1}{2}\left(\frac{\dot{P}}{P} - \frac{\dot{H}}{H}\right) = \frac{1}{2}\frac{\dot{P}}{P}\left(1 - \frac{\frac{h^*}{h}}{4\left(1+\frac{h^*}{h}\right)}\right)^{-1} \tag{4.1}$$

where h is the indentation depth, P is the load, H is the measured hardness, and the corresponding rate parameters (change per unit time) are noted as $\dot{h}$, $\dot{P}$ and $\dot{H}$, respectively [114]. During nanoindentation testing with CLR method, the loading rate is constant and the load increases with increasing indent depth; thus the strain rate decreases with indent depth as inferred from Eq. 4.1. In the current CLR tests, $\dot{P}/P$ decreases from 0.1 /s to 0.017 /s in the

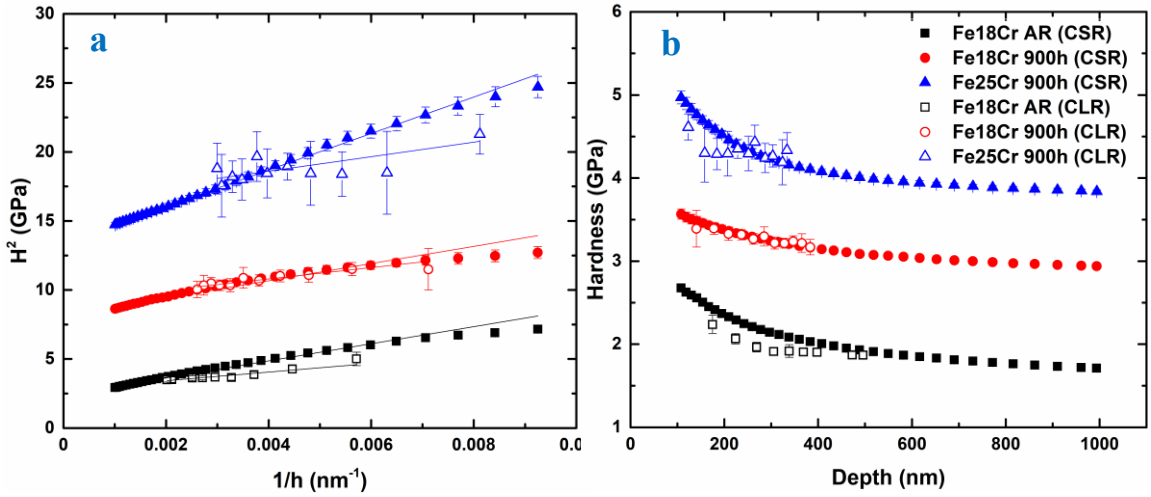

Fig. 4.4 Comparison of constant strain rate and constant loading rate test methods on as received and 900 h aged Fe18Cr. (a) H vs. h plot. (b) H^2 vs. 1/h plot.

Table 4.2 Summary of the bulk equivalent hardness obtained from Nix-Gao model for constant strain rate and constant loading rate test method.

Test method		Fe18Cr		Fe25Cr
		AR	900 h	900 h
H_0 (GPa)	CSR (0.05 /s)	1.55	2.86	3.66
	CLR (0.2 mN/s)	1.67	3.03	4.06
h^* (nm)	CSR (0.05 /s)	259	76	99
	CLR (0.2 mN/s)	111	45	32

first 100-500 nm. Therefore, the comparable results in Table 4.2 from these two methods indicate that the strain rate effect on the mechanical properties of the investigated materials is small (<10 % effect on H_0), in agreement with the strain rate results previously summarized in Table 4.1. This can be attributed to the relatively low room temperature strain rate sensitivity in the Fe and Fe-Cr alloys examined in this study, which will be discussed later. However, due to the change of strain rate with depth, nanoindentation with CLR method on materials with stronger strain rate sensitivity would produce mechanical property data that cannot be directly compared with constant strain rate tensile tests.

4.1.4. Electropolishing and grain orientation effects

In the current research using a Berkovich indenter, the final mechanical polishing was performed using colloidal silica suspension of size 0.05 μm, which is much finer than the relatively coarse particle size (1 μm) used in reference [115]. Two separate batches of samples were electropolished and mechanically polished in order to investigate the possible influence of near-surface mechanical damage on the measured hardness. The nanoindentation testing was conducted at a constant strain rate of 0.05/s on 900 h aged Fe18Cr and 100 h aged Fe25Cr.

Fig. 4.5 compares the effect of electropolishing I and mechanical polishing (M) on the depth-dependent hardness and Nix-Gao plots of the investigated materials. The hardness vs. depth curves in Fig. 4.5a show only a slight difference between electropolished and mechanically polished samples, approaching to the same value as indent depth extends to deeper region. Fig. 4.5b presents the corresponding Nix-Gao fitting curves. It is obvious that an inflection occurs on each of these four curves, around an indent depth of 200 nm. Although the magnitude of the curvature is slightly reduced in the electropolished samples compared to the mechanically polished samples, the data for both polishing conditions are within statistical error of each other and it is evident that electropolishing does not eliminate the curvature at shallow indent depth (~200 nm).

Table 4.3 compares the bulk equivalent hardness extracted using the Nix-Gao model. Electropolished samples produce negligibly (1-2%) lower bulk hardness values compared to mechanically polished samples. Generally, the hardness values from both polishing methods are comparable to each other for the investigated Fe18Cr and Fe25Cr alloy in this study. This indicates that consistent nanoindentation mechanical property results on the electropolished and mechanically polished samples may be produced by the fine mechanical polishing process (using the colloidal silica suspension with particle size of 0.05 μm). Furthermore, the observed

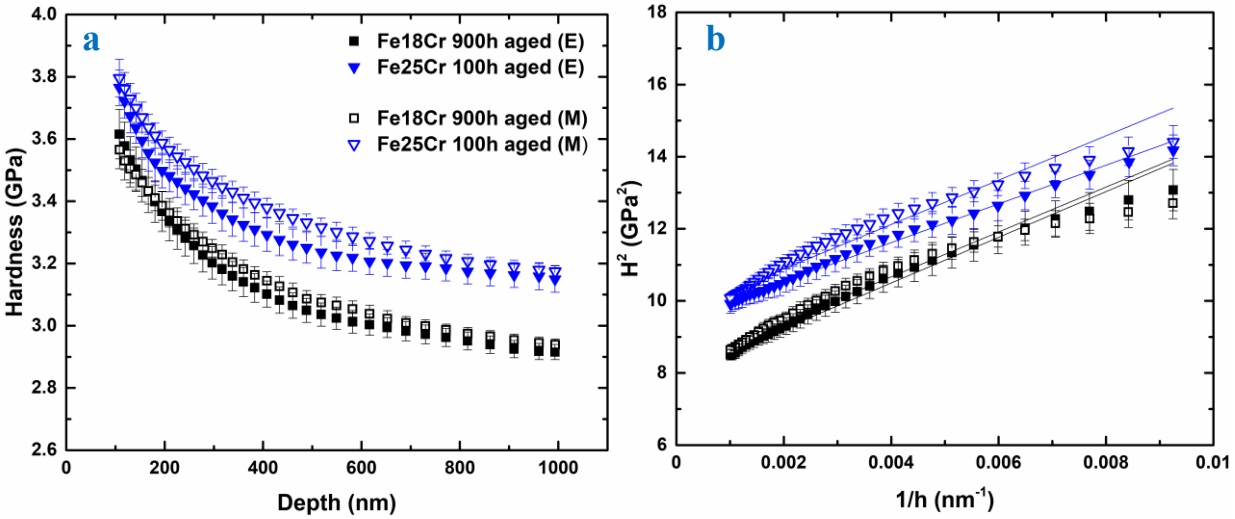

Fig. 4.5 The effect of electropolishing (E) and mechanical polishing (M) on the hardness of 900 h aged Fe18Cr and 100 h aged Fe25Cr. (a) H vs. h plot. (b) H^2 vs. 1/h plot.

Table 4.3 Comparison of electropolishing and mechanical polishing on hardness of 900 h aged Fe18Cr and 100 h aged Fe25Cr.

Hardness (GPa)	Fe18Cr 900 h	Fe25Cr 100 h
Electropolishing	2.86	3.11
Mechanical polishing	2.82	3.08

curvature in the Nix-Gao plots at indent depths near 200 nm does not appear to be attributable to mechanical polishing artifacts.

Another issue related to indentation surface is the grain orientation effect. The grain sizes of most of the investigated materials were large enough to easily contain 25 nanoindentation indents as stated in the experimental section. A potential difference on nanoindentation hardness may occur due to grain orientation as reported in prior studies [116–119]. Therefore, it is necessary to quantify the effect of grain orientation on the nanoindentation hardness for comprehensive understanding of its impact on measured hardness compared to other aspects such as thermal aging, strain rate effect, etc.

In the current study, nanoindentation with constant strain rate of 0.05 /s was performed on Fe18Cr and Fe25Cr for both as-received and 900 h aged conditions. 25 indentations were conducted on each of [001], [101], [111] oriented surfaces, respectively, to produce hardness results with acceptably low statistical errors. Fig. 4.6a presents the depth dependence of the nanoindentation hardness of 900 h aged Fe18Cr sample for a reference. Overall, the hardness for all three grain orientations exhibited the typical ISE behavior where the hardness gradually decreases with increasing indentation depth. The measured hardness is similar for all three surface orientations, especially for [101] and [111] oriented surfaces. Table 4.4 shows that [101] surfaces always exhibit the largest bulk equivalent hardness extracted from the Nix-Gao plot, while the hardness from [001] surfaces is the lowest. There is no significant variation of the bulk equivalent hardness for the three different surface orientations, i.e., all H_0 values were within 5% except the as-received Fe25Cr of which the largest hardness increases from [001] to [101] surface is about 8.6%. The relatively weak orientation effect can be attributed to the biaxial stress state induced under the indenter, combined with the numerous dislocation slip systems that can be activated for the BCC crystal structure. This weak dependence of hardness on crystal orientation in nanoindentation is consistent with the prior studies on both BCC and FCC materials [116,118,120,121]. Thus, grain orientation effects were not carefully monitored in this paper.

4.1.5. Pileup effects

In the current study, a batch of separate nanoindentation experiments were performed on 5 samples: as-received pure Fe, Fe14Cr, Fe18Cr and 100-300 h aged Fe18Cr, which have distinct hardness values. A constant strain rate of 0.05 /s was used for the nanoindentation tests with maximum indent depths of 200, 400, 600, 800 and 1000 nm, in order to characterize the

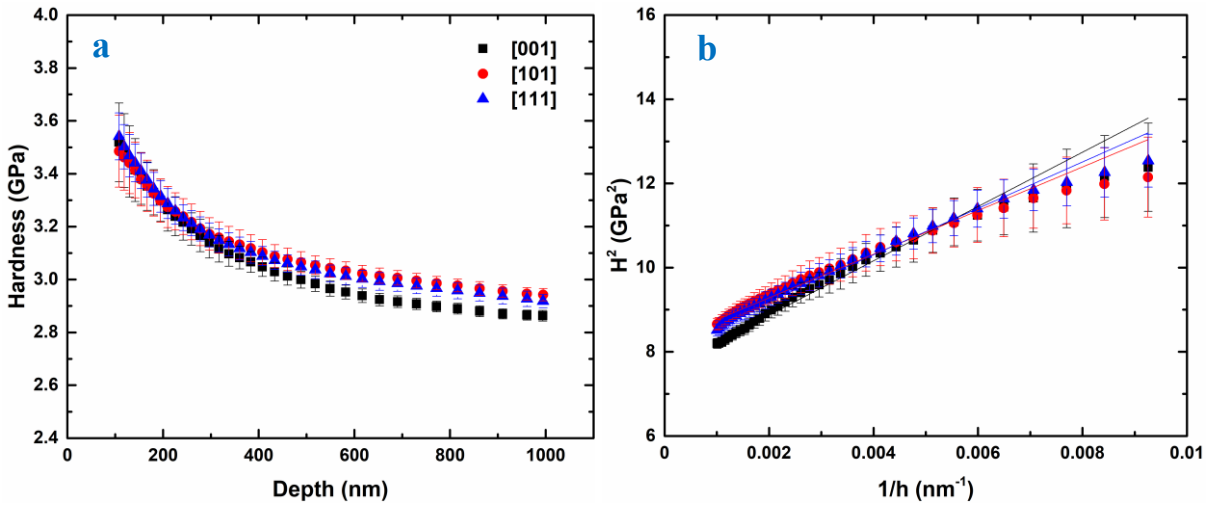

Fig. 4.6 (a) Depth dependence of hardness and (b) the corresponding Nix-Gao plot of 900 h aged Fe18Cr on three grain orientations with the surfaces normal to [001], [101] and [111] directions, respectively.

Table 4.4 Comparison of bulk equivalent hardness of Fe18Cr and Fe25Cr from [001], [101] and [111] orientated surfaces.

Hardness (GPa)	Fe18Cr AR	Fe18Cr 900 h	Fe25Cr AR	Fe25Cr 900 h
[001]	1.50	2.75	1.74	3.60
[101]	1.55	2.87	1.89	3.75
[111]	1.54	2.85	1.81	3.68

variation of pileup height with indent depth. Subsequently, atomic force microscopy (AFM) was used to measure the pileup height Δh of the residual indents produced by different indent depths. Fig. 4.7a shows the typical surface tomography in 300 h aged Fe18Cr after nanoindentation test. It is obvious that the pileup height varies along each side of the indent, revealing some moderate orientation dependence. In all cases, the pileup height was approximately zero at the three indent corners and was maximized near the midpoint along each of the three indent sides. Kese et al. proposed that the contact periphery can be estimated as a semi ellipse [93]. But careful SEM imaging shows that this approximation may overestimate the increased contact area induced by pileup. Fig. 4.8a presents a SEM image of 300 h aged Fe18Cr specimen in our study. The corner-to-corner contact area is included by a white dashed triangle, and the extra area on one side due to pileup is marked by a red dashed curve. This projected area clearly shows that there is little or no pileup effect near the corner region, thus the periphery will not be a semi elliptical shape. Fig. 4.8b shows a better schematic diagram of the plan view and cross section of the indent site. Compared with the semi-elliptical estimation (black dashed line), a sinusoidal approximation (red dotted line) of the contact periphery is more appropriate since a sinusoidal curve accounts for the reduced pileup effect near the corner region. For simplicity, the area under the sinusoidal curve is equivalent to an area in a triangle as marked by the blue dashed line in Fig. 4.8b. From the cross section through the edge and face of the indentation imprints, the pileup height Δh is measured as the vertical distance between the highest point of the pileup and the original surface.

Fig. 4.9 presents the variation of measured pileup height with the indentation depth, with the y axis referring to the sum of the peak pileup heights from the three sides of the indent. Generally, the total pileup height $(\Delta h)_{total}$ increases linearly with indent depth h for all five tested materials. Using this linear relationship between indentation depth and total pileup height, the continuous pileup height during nanoindentation can be obtained easily. Whereas there is a slight (<25 nm) y-intercept offset in the linear fitting curves for all the investigated materials, this may be caused by an error of the AFM measurement for such a minor pileup height at shallow indentation depth. The pileup height of Fe25Cr alloys were also measured for indent depths of 1000 nm.

In this study, the sinusoidal approximation was applied to account for the pileup contact area, which is based on the semi-ellipse method developed by Kese et al. [93]. Thus, Eq. 2.15 has been modified as,

$$A_{pu} = \frac{b}{2} a_i \tag{4.2}$$

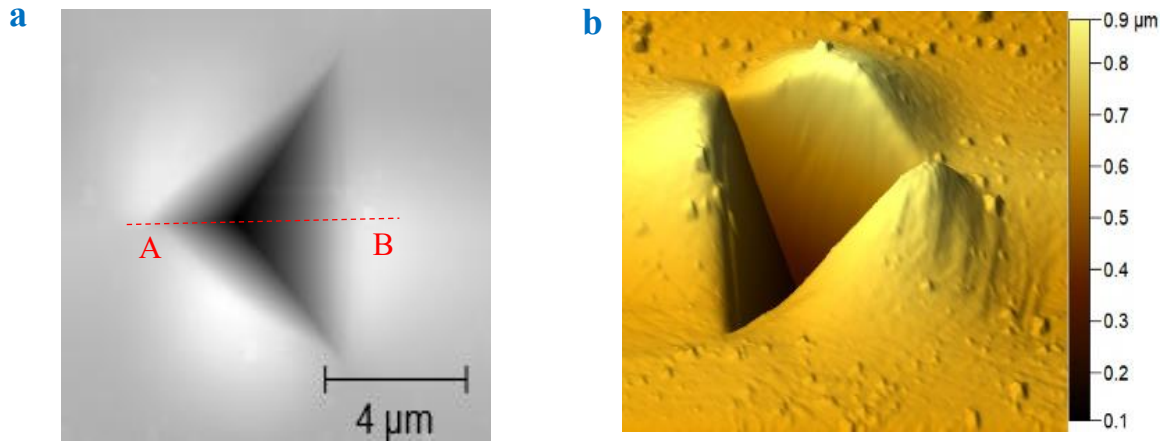

Fig. 4.7 (a) The AFM image of a 1000 nm indent of 300 h aged Fe18Cr. (b) The enlarged 3D tomography.

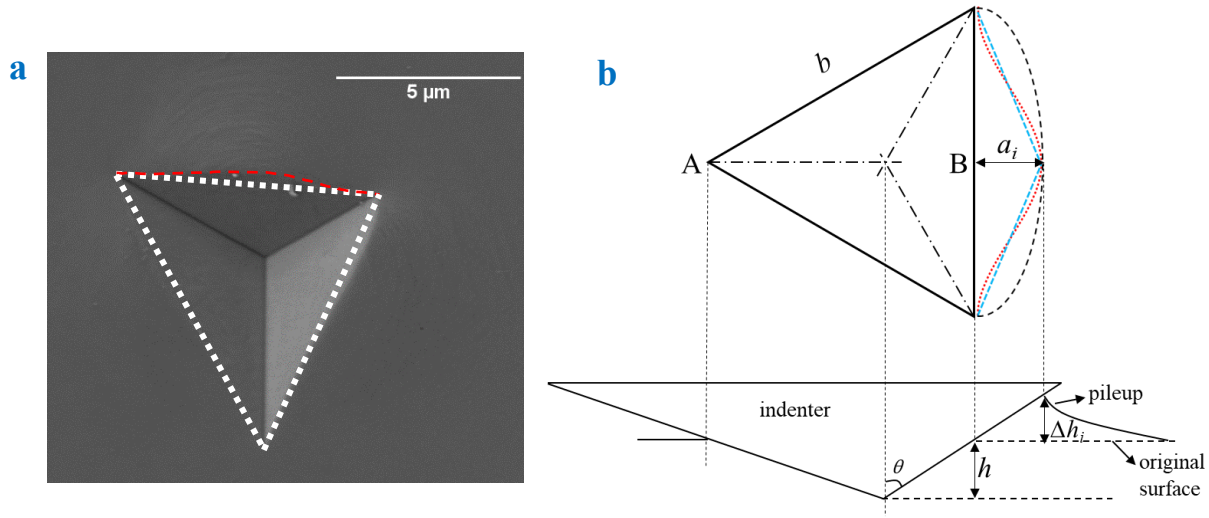

Fig. 4.8 (a) SEM image of an indent from 300 h aged Fe18Cr. The white dashed line refers to the corner-to-corner contact area. The dashed red line refers to the increased contact area due to pileup effect. (b) The schematic diagram of the indent and the cross section. The semi ellipse with short axis a_i refers to the estimated contact periphery of the indenter with material [93]. The red dotted line is a sinusoidal approximation of the contact periphery, while the blue dashed line refers to a triangle approximation.

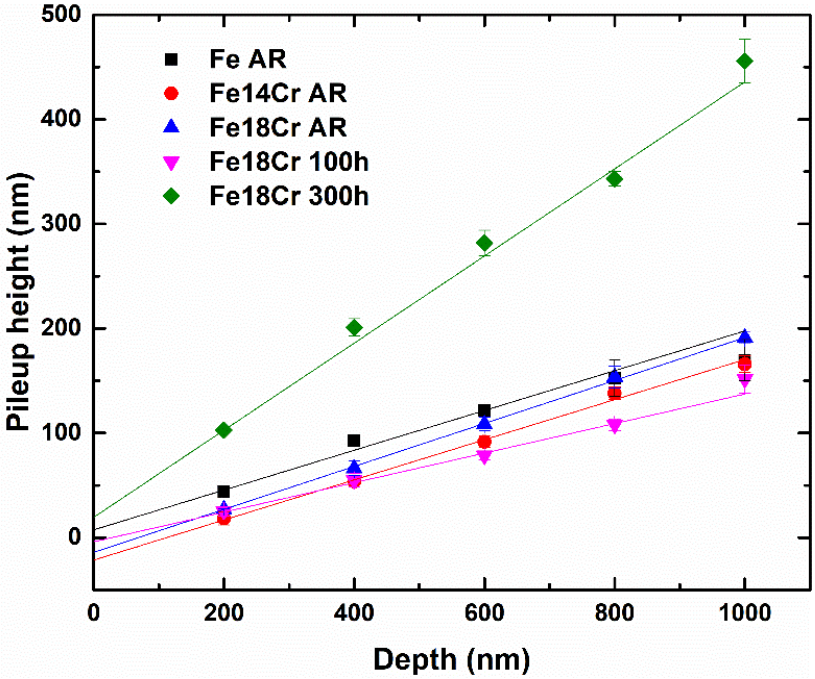

Fig. 4.9 The variation of sum of peak pileup height from three sides of the indent with indentation depth.

In the AFM characterization, the peak pileup height Δh_i was measured on each side of the indent. During nanoindentation, Δh_i and a_i obey the following mathematic relation due to the close contact of the indenter with the sample,

$$a_i = \Delta h_i \cdot \tan 65.3^{\circ} \tag{4.3}$$

where 65.3° is the face angle of Berkovich indenter. Therefore, combining Eq. 2.16, 2.17, 4.2, and 4.3, the corrected contact area can be described in the following equation,

$$A_c = A + 1.65\sqrt{A}(\Delta h)_{total} \tag{4.4}$$

where $(\Delta h)_{total}$ is described as a function of indentation depth h as shown in Fig. 4.9. Combining Eq. 2.14 and 4.4, the hardness and modulus can be corrected for pileup effects in a straightforward way.

Fig. 4.10 compares the depth-dependent hardness, modulus and Nix-Gao plotting from uncorrected data and pileup-corrected values by applying Eq. 4.4 to the Oliver-Pharr method. The Fe18Cr sample aged for 300 h was taken as an example here, using the raw nanoindentation data with the maximum indent depth of 1000 nm. The slight offset in the linear fitting of total pileup height vs. indentation depth in Fig. 4.9 was considered in the correction process. In Fig. 4.10c, a statistically significant change in the Nix-Gao curve slope (ISE length scale h^*) and y-intercept (bulk hardness H_0) is evident, and a slight curvature at shallow indentation depths (below ~200 nm) still exists in the corrected data. A similar change of hardness, modulus and ISE effect before and after pileup correction was also observed for as-received Fe, Fe14Cr, Fe18Cr and 100 h aged Fe18Cr. In summary, indentation pileup effects produce significant modifications to both the fitted bulk equivalent hardness and the ISE length scale parameter, but do not appear to be responsible for the observed curvature in Nix-Gao plots at indent depths below ~200 nm.

It is worth noting that the pileup height y-intercept offset values in Fig. 4.9 are relatively small (approximately zero, considering statistical uncertainties in the data). To quantify the effect of the apparent offset, a non-offset linear fitting of the pileup height vs. indent depth was constructed based on the zero point and the pileup height value at a final depth, i.e., 1000 nm. The same correction process mentioned above was subsequently performed on the five materials. A summary of the fitted Nix-Gao bulk equivalent hardness values, ISE scale parameters and the measured modulus for the uncorrected and pileup-corrected (with and without offset) evaluations of these five tested material conditions is shown in Table 4.5. Several uncorrected results reported here are slightly different with those in Table 4.1 (which were extracted from an independent series of indentation tests using the same constant strain

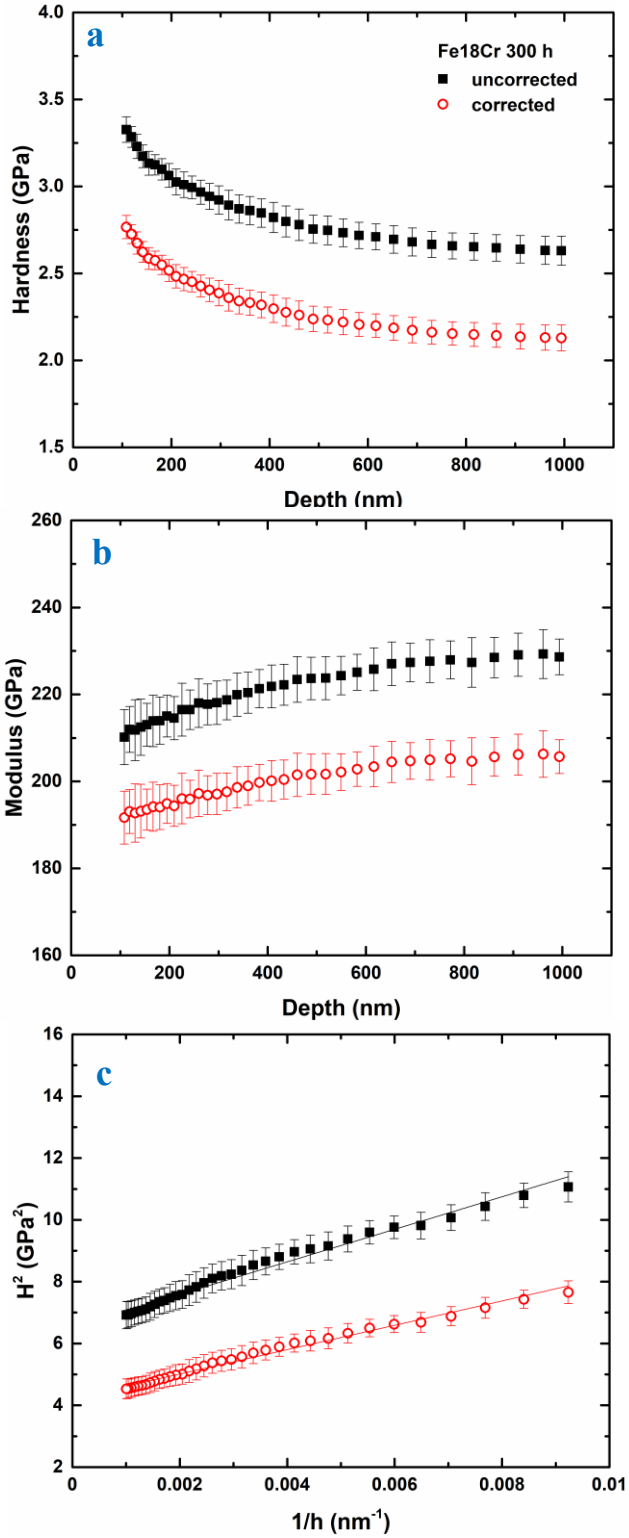

Fig. 4.10 Comparison of the uncorrected and pileup-corrected data of 300 h aged Fe18Cr, by using the actual area function accounting for the pileup. (a) Hardness vs. depth. (b) Modulus vs. depth. (c) H^2 vs. 1/h.

Table 4.5 The comparison of the uncorrected and corrected H_0, E, and h^* using pileup corrections on contact areas. AR refers to the as-received condition, and 100-900 h refer to the 475ºC aged conditions. The units for H_0 and h^* are GPa and nm, respectively.

	Fe	Fe14Cr		Fe18Cr				Fe25Cr			
	AR	AR	300h	AR	100h	300h	900h	AR	100h	300h	900h
Uncorrected H_0	1.09	1.39	1.47	1.55	1.76	2.56	2.86	1.76	3.11	3.45	3.66
Corrected (with offset) H_0	1.03	1.30	-	1.44	1.67	2.25	-	-	-	-	-
Corrected (no offset) H_0	1.03	1.31	1.37	1.45	1.67	2.21	2.47	1.65	2.86	3.14	3.26
$\Delta H_0/H_0$	6%	6%	7%	6%	5%	14%	14%	7%	8%	9%	11%
Uncorrected E	203	205	207	207	216	221	224	210	226	230	230
Corrected (with offset) E	197	201	-	202	211	206	-	-	-	-	-
Corrected (no offset) E	198	198	201	201	211	206	208	202	216	216	218
Uncorrected h^*	385	227	164	246	285	81	76	269	64	42	99
Corrected (with offset) h^*	378	264	-	277	298	71	-	-	-	-	-
Corrected (no offset) h^*	392	222	168	252	291	89	61	262	59	46	105

rate of 0.05 /s). However, this difference is less than 10%, and is considered to be representative of the statistical errors between independent sets of experiments. Table 4.5 compares the corrected results with and without considering the small y-intercept offset. It is apparent that there is almost no difference in the corrected bulk equivalent hardness whether the non-zero offset is considered in the pileup correction for the examined set of Fe and Fe-Cr alloys. This indicates that the quantitative impact of the slight offset in the pileup height relation with depth is practically negligible. The slight offset might be introduced by resolution uncertainties in the pileup height at very small scale. Kese et al. reported a small offset in their measurement of a_i that was attributed to resolution limitations of AFM technique, which can produce some error when measuring pileups under 30 nm [93]. Therefore, quick pileup corrections of the rest of the samples were performed by using the non-offset method, as listed in Table 4.5. The decrease of the pile-up corrected hardness relative to the uncorrected hardness ($\Delta H_0/H_0$) is from 5% to 14% for the examined samples in Table 4.5. In general, the magnitude of the hardness decrease appears to roughly correlate with increased initial hardness. For both Fe18Cr and Fe25Cr samples, aging for 300 h and 900 h resulted in the highest magnitude of hardness decrease, while all the as-received and 100 h aged samples presented lower hardness decrease.

4.1.6. Cr-rich α' precipitates

The APT analysis was performed on 100-900 h aged Fe18Cr and Fe25Cr samples to characterize the size and number density of the α' precipitates (precipitates were confirmed by APT to be absent in the as-received Fe-Cr alloys). The spherical equivalent radius was used to quantify the size of the α' precipitates, which can be derived with the following formula $r = \sqrt{3N / 4\pi\rho Q}$, where N is the number of atoms in the cluster, ρ = 84.3 *atoms/nm*^{3} is the atomic density and Q is the detection efficiency [122]. Table 4.6 presents the APT results of the aged samples. Both the size and number density of the α' precipitates increase with increased aging time up to 300 h, while longer aging results in coarsening (growth in precipitate size with accompanying decrease in number density) for 900 h aged Fe18Cr. In aged Fe25Cr samples, about 20% of the α' precipitates were observed as non-spherical, and the equivalent spherical radius was calculated to simplify the hardening model. After thermal aging, the Cr concentration in the matrix of the aged samples was reduced compared with the as-received samples due to the segregation of Cr to form the α' precipitates. Therefore, the matrix solution

Table 4.6 Number density and radius of α' precipitates as well as the Cr content in the matrix of 100-900 h aged Fe18Cr and Fe25Cr samples.

Materials	Density ($10^{24}/m^3$)		Radius (nm)		Cr in matrix (wt. %)
	Spherical	Non-spherical	Spherical	Non-spherical	
Fe18Cr AR	-	-	-	-	17.97
100h	0.71±0.01	-	1.06±0.01	-	17.67±0.08
300h	3.34±0.04	-	1.56±0.01	-	14.60±0.08
900h	2.41±0.07	-	1.89±0.02	-	12.77±0.01
Fe25Cr AR	-	-	-	-	24.97
100h	3.85±0.17	0.91±0.10	1.44±0.02	1.95±0.03	18.10±0.38
300h	1.71±0.08	0.52±0.04	1.80±0.01	2.82±0.10	14.65±0.10
900h	1.17±0.06	0.30±0.01	2.15±0.02	3.45±0.08	12.90±0.06

hardening component of these aged Fe18Cr samples should be different from the as-received Fe18Cr, which will be discussed later in this paper.

4.2. Microstructure evolution and mechanical properties of ion irradiated Fe-Cr

4.2.1. Dislocation microstructure after 0.37 dpa

Fig. 4.11 shows the TEM cross-section overview of a typical irradiated specimen in this study (450 ℃, 10^{-5} dpa/s, 0.37 dpa). There is a denuded zone with little defects in the first ~800 nm, which may be caused by the diffusion of the interstitials to the specimen surface. At depth beyond ~1.2 um, as shown in Fig. 4.11, the dislocation loop density increases rapidly in the region corresponding to the implanted Fe ions with a peak injection appearing at ~2 um. The injected interstitials can work as nucleation sites for the dislocation loops thus introducing artifacts in quantitative analysis. To avoid the specimen surface effects and the effect of injected ions, the microstructures were only analyzed at the mid-range of irradiation depth from 800 to 1200 nm [61]. Meanwhile, the irradiated microstructures were only observed in the irradiated region. Beyond this ~2.2 um region, the background is free of defects, which demonstrates that electropolishing eliminated the FIB damage in the whole sample foil.

For specimens irradiated to 0.37 dpa, Fig. 4.12 exhibits the evolution of microstructures under different temperatures and dose rates. For direct comparison, only mid-range images were shown with the same scale bar.

At a dose rate of 10^{-3} dpa/s, the pre-existing dislocation lines were observed for 300 and 350 °C irradiations, with a density of 1.33×10^{14} m^{-2} and 2.86×10^{13} m^{-2}, respectively. The edge-on dislocation loops appeared at 450 °C after irradiation to 0.37 dpa, as illustrated by the red arrows. Besides the dislocations, the black dot defects started to nucleate in the matrix and around the dislocation lines at 350 °C, which was also observed at 450 °C.

When reducing the dose rate to 10^{-4} dpa/s, the temperature for the appearance of black dot defects shifted to 300 °C. The dislocation line density keeps the same order as those specimens irradiated at 10^{-3} dpa/s. At an elevated temperature of 450 °C, the small defects on the dislocation lines nucleated to dislocation loops as shown by red arrows in Fig. 4.12f. The alignment of the dislocation loops at 450 °C indicates that the black dot defects at 300 and 350 °C are likely the precursors of dislocation loops.

At the lowest irradiation dose rate of 10^{-5} dpa/s, more complicated microstructures were observed for 450 °C, which consisted of edge-on dislocation loops (red arrows), black dot

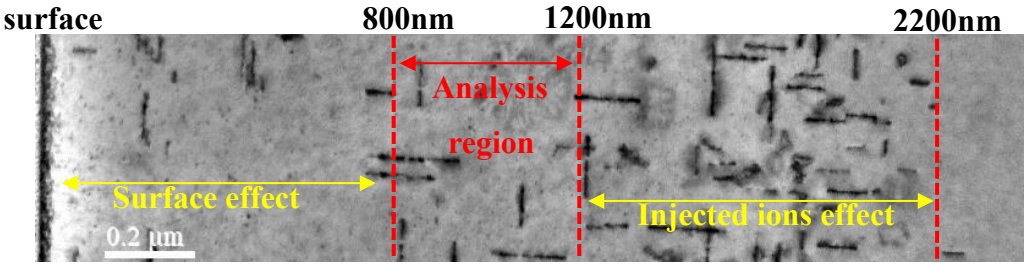

Fig. 4.11 STEM-BF image of the whole irradiated region. The irradiation condition is: 450℃, 10-5 dpa/s, 0.37 dpa.

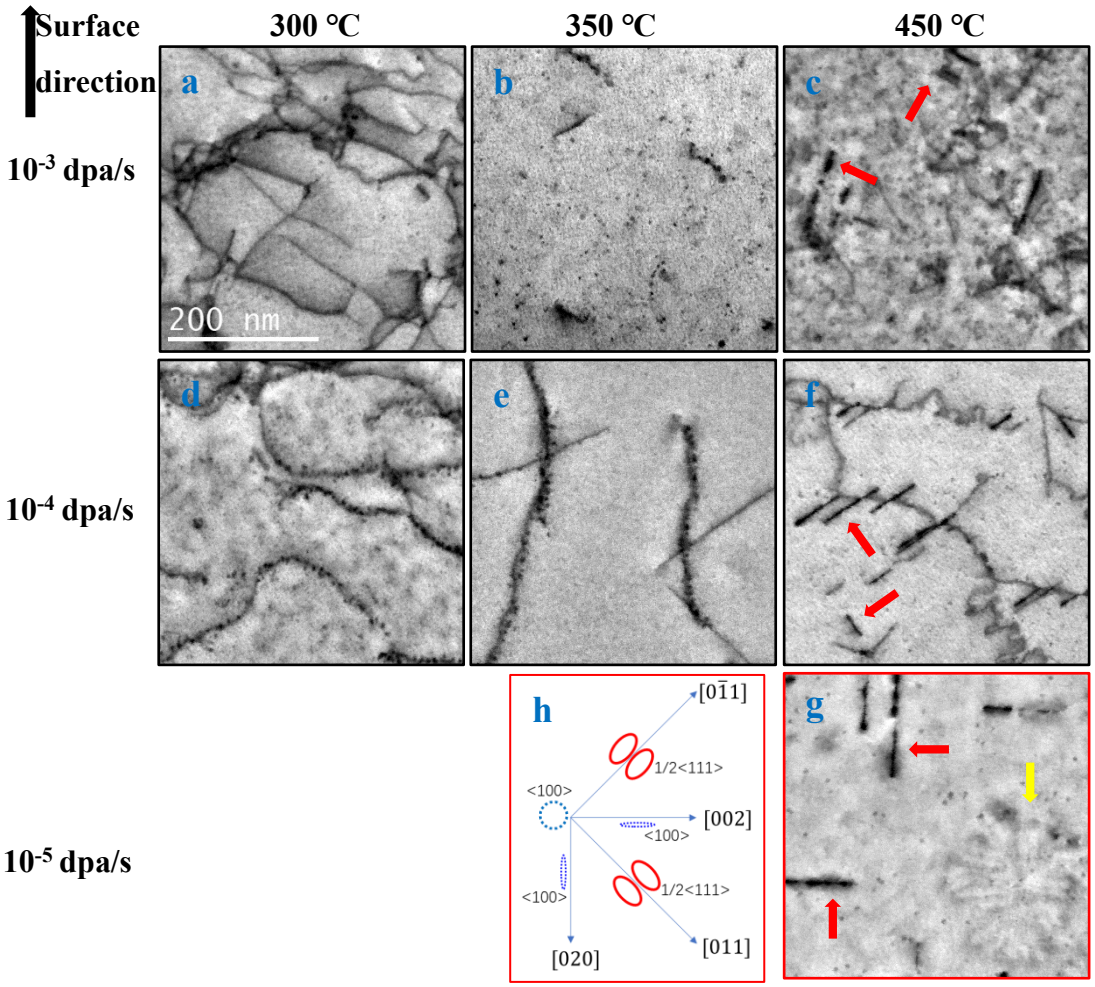

Fig. 4.12 The dislocation line/loop evolution with irradiation temperatures and dose rates. The damage dose is 0.37 dpa. All the images were taken from 800 nm to 1200 nm below the sample surface with the same scale bar. The dislocation-loop map is only corresponding to the specimen 450 °C : 10^{-5}dpa/s.

defects and petal-shaped dislocation loops (yellow arrows). However, pre-existing dislocation lines were observed at all the irradiated specimens except for the one 450 °C : 10^{-5} dpa/s (irradiation temperature : dose rate). The absence of dislocation lines may be caused by annealing under high temperature and low dose rate irradiation.

Overall, the dislocation loops only occurred at the highest temperature, while lower temperatures induced only dislocation loop precursors. The type of the dislocation loops can be identified by the dislocation-loop map as shown in Fig. 4.12. The corresponding STEM-BF image is the specimen 450 °C : 10^{-5} dpa/s. The vertical and horizontal dislocation loops in Fig. 4.12g are evidently the <100> loops as indicated in the map, while the petal-shape dislocation may refer to the open-shape <100> loops. At this mid-range region, no 1/2<111> loops were observed. Since the line dislocation network was not characterized before irradiation for each sample, it's hard to quantify the irradiation effect on the dislocation lines. However, these characterized dislocation lines indeed contribute to the hardness of the irradiated materials. We will not discuss the evolution of the dislocation line in the later sections, but only consider it for correlation between hardness and microstructures.

Fig. 4.13 presents the number density and size distribution of <100> dislocation loops at 450 °C with different dose rates. The error bar on the density refers to the non-homogenous distribution of the dislocation loops in the 800-1200 nm region. With the increasing of irradiation dose rates, the number density of <100> loops slightly decreases and then increases subsequently, with little statistical difference if considering the error bars, as shown in Fig. 4.13a. In contrast, the loop size is significantly affected by the change of irradiation dose rate. As indicated by Fig. 4.13b, the small dislocation loops were dominant at lower dose rates, while the loop growth seems to occur at 10^{-5} dpa/s since the size spectrum is much broader.

The black dot defects were observed at all the irradiation conditions except at the lowest temperature and the highest dose rate at 0.37 dpa. Fig. 4.14 presents the number density and size of the black dots under different temperatures and dose rates. With the increasing of temperature, the amount of black dots generally decreases, which may be attributed to the formation of dislocation loops at higher temperature. At 450 °C, lower dose rate promoted the nucleation of the black dots, while the trend is totally reversed at 350 °C. For the black dot size, the change with both temperatures and dose rates are minor. There is only a slight increase of dot size at 350 °C for lower dose rate possibly due to the longer irradiation time at this condition. However, at 450°C, the dot size almost kept the same value regardless of the dose rates when considering the error bars.

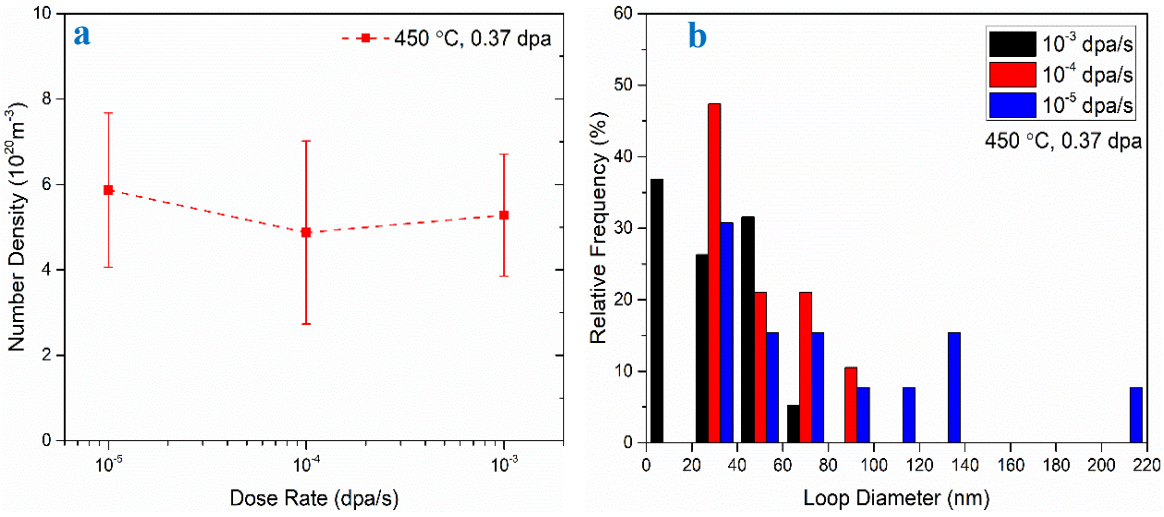

Fig. 4.13 (a) The number density and (b) size distribution of <100> dislocation loops at 450 ℃ under different dose rates.

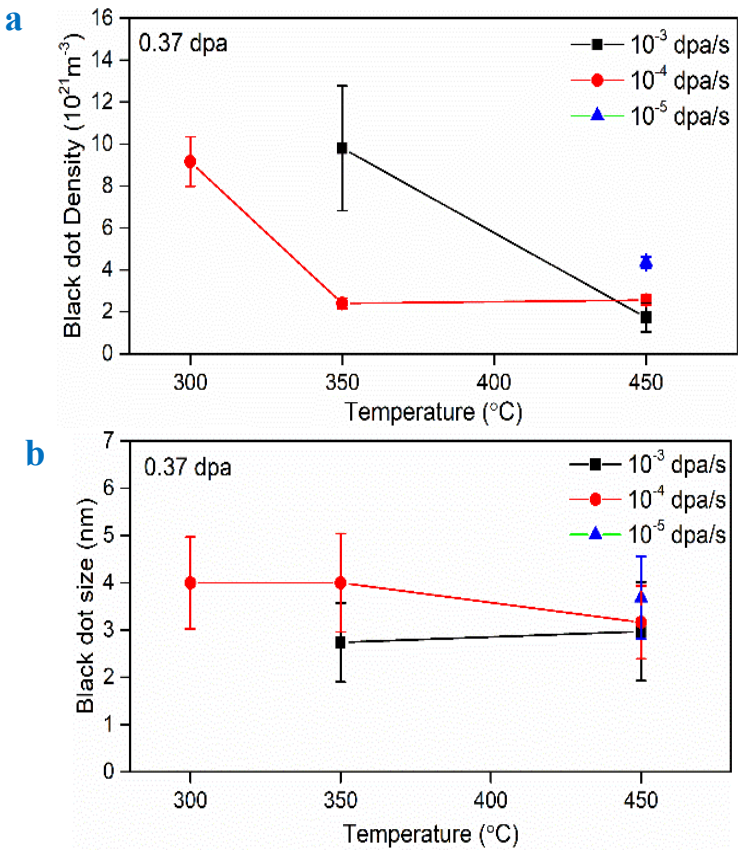

Fig. 4.14 The evolution of number density and size of the black dot defects with temperatures and dose rates at 0.35 dpa.

4.2.2. Dislocation microstructure after 3.7 dpa

Two more specimens were irradiated to a higher midrange dose of 3.7 dpa at 350 and 450 °C at a dose rate of 10^{-4} dpa/s. Fig. 4.15 shows the STEM-BF images of the dislocation distribution. Similar to the results under 0.37 dpa, only pre-existing dislocation lines with decorated black dot defects were observed at 350 °C under 3.7 dpa. According to the dislocation loop map, <100> loops were clearly imaged at 450 °C, with a slight shift to larger size compared with irradiations to 0.37 dpa as shown in Fig. 4.16a. At this higher irradiation dose, no 1/2<111> loops were observed at the 800-1200 nm region, which is consistent with the results at 0.37 dpa. Fig. 4.16b shows that at higher dose, the black dot density is much more sensitive with temperature, while the size is not significantly affected by the temperature at either 0.37 or 3.7 dpa as shown in Fig. 4.16c. At 350 °C, since there is no formation of dislocation loops, the black dot density increases with the increasing dose. However, the possible transformation of black dots to the dislocation loops under higher irradiation dose at 450 °C may be responsible for the decreasing of the black dot density for 3.7 dpa vs. 0.37 dpa.

Table 4.7 summarizes the quantitative analysis results of the dislocation line, loop and black dot. Since the loop size in the 800- 1200 nm region varies widely, the weighted average size was calculated based on the relative frequency in Fig. 4.13b and Fig. 4.16a.

4.2.3. Cr-rich precipitates

APT analysis was performed on the irradiated Fe18Cr samples to characterize the size and number density of the Cr-rich α' precipitates. The pristine sample were also confirmed by APT to be absent of α' precipitates. Table 4.8 presents the APT results of the investigated samples, which is reproduced from our prior study [123]. After irradiation, the α' precipitates were observed in all samples excluding the one irradiated at 300 °C, 0.35 dpa, 10^{-3} dpa/s. The Cr concentration in the matrix of the irradiated samples was reduced compared with the pristine samples due to the segregation of Cr to form the α' precipitates. Therefore, the matrix solution hardening component of these irradiated samples should be different from the as-received samples, which will be discussed later in this thesis.

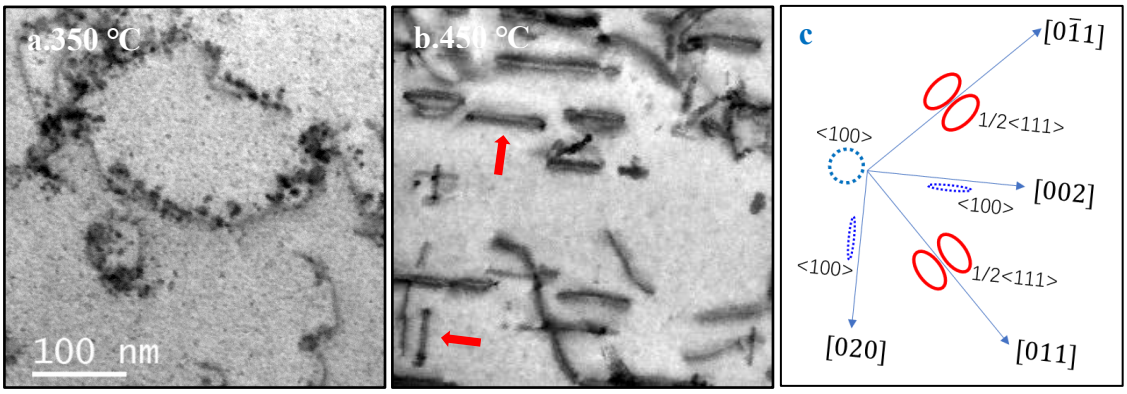

Fig. 4.15 The dislocation distribution for 3.7 dpa and 10^{-4} dpa/s at (a) 350 °C and (b) 450 °C. Only local images from 800-1200 nm region were shown. (c) The corresponding dislocation loop map at [100] zone under STEM condition.

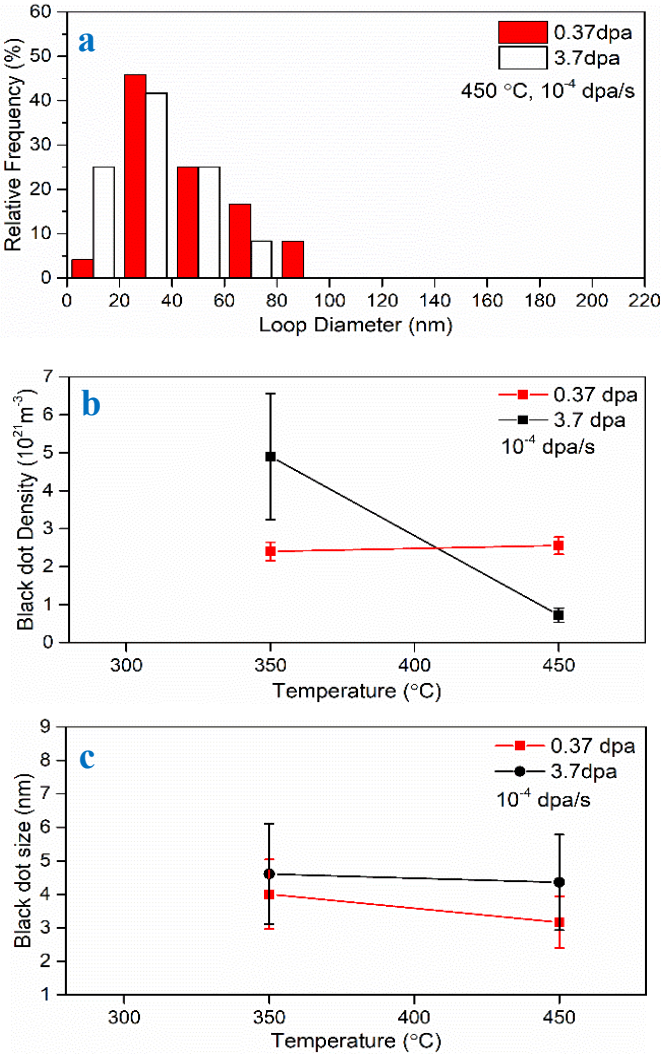

Fig. 4.16 (a)The dislocation loop size distribution under 450 °C, 10^{-4} dpa/s to 0.37 and 3.7 dpa. The black dots (b) density and (c) size evolution with irradiation temperature under 0.37 and 3.7 dpa.

Table 4.7 Summary of the density and size of dislocation line, loop, black dots in the mid-range irradiation region.

Dose (dpa)	0.37							3.7	
Dose rate (dpa/s)	10^{-3}			10^{-4}			10^{-5}	10^{-4}	
Temperature (°C)	300	350	450	300	350	450	450	350	450
ρ_{line} ($\times10^{14}m^{-2}$)	1.33	0.27	1.75	1.23	0.25	1.08	-	0.36	0.34
$\rho_{<100>}$ ($\times10^{20}m^{-3}$)	-	-	5.26±1.43	-	-	4.87±2.14	5.87±1.84	-	7.83±3.69
$d_{<100>}$ (nm)	-	-	32.37±3.39	-	-	43.56±3.93	75.40±2.95	-	30.92±3.26
ρ_{dots} ($\times10^{21}m^{-3}$)	-	9.80±2.98	1.73±0.70	9.17±1.18	2.40±0.24	2.56±0.23	4.36±0.27	4.90±1.66	0.72±0.19
d_{dots} (nm)	-	2.74±0.84	2.97±1.05	4.00±0.97	4.00±1.04	3.17±0.77	3.38±0.87	4.61±1.50	4.36±1.43

Table 4.8 Number density and radius of α' precipitates as well as the Cr content in the matrix of the irradiated Fe18Cr samples (Reproduced from Ref. [123]).

Dose (dpa)	Dose rate (dpa/s)	Temperature (°C)	Density ($10^{24}/m^3$)	Radius (nm)	Cr in matrix (at. %)
Pristine	-	-	-	-	19.05
0.37	10^{-3}	300	-	-	
		350	3.90 ± 1.24	1.10 ± 0.02	17.2 ± 0.2
		450	2.25 ± 0.35	1.35 ± 0.13	17.4 ± 0.7
	10^{-4}	300	2.17 ± 0.61	1.08 ± 0.03	17.6 ± 0.3
		350	4.82 ± 1.77	1.12 ± 0.02	16.6 ± 0.7
		450	3.49 ± 0.27	1.42 ± 0.03	16.0 ± 0.5
	10^{-5}	450	4.36 ± 1.46	1.57 ± 0.02	13.5 ± 0.2
3.7	10^{-4}	350	4.02 ± 0.71	1.29 ± 0.01	15.4 ± 0.5
		450	0.94 ± 0.06	2.01 ± 0.08	16.3 ± 0.3

4.2.4. Nanoindentation hardness

Fig. 4.17a shows the typical nanoindentation measured hardness vs. depth curves for the Fe18Cr samples irradiated at 450 °C, 0.37 dpa with different dose rates, as well as the pristine sample. The indentation size effect (ISE) is clearly manifested as the decreasing hardness with the increasing depth. For data analysis, the H^2 vs. inverse depth curves was produced from Fig. 4.17a, and an inflection was observed on the curves around 250 nm as shown in Fig. 4.17b. Nix-Gao fitting was used to obtain the bulk equivalent hardness from H^2 vs 1/h curves according to Eq. 2.12. And the bulk equivalent hardness H_0 can be described as the intercept of linear fitting results of the H^2 vs. 1/h data. However, for the nanoindentation experiment on ion-irradiated materials, a typical plastic zone that extends beyond 5-10 times the indent depth is usually assumed [99,100]. In the current study, the region available for extracting bulk equivalent hardness is limited in less than 200-400 nm due to a total damaged region of 2.2 μm. Beyond this shallow 200-400 nm region (~250 nm for 450 °C irradiated samples in Fig. 4.17), the unirradiated substrate larger than 2.2 μm starts to contribute to the hardening component, which is reflected by the inflection on the curves in Fig. 4.17b. Therefore, the film/substrate model by Kasada et al. [101] was applied to only fit the data points before the inflection point.

Table 4.9 summarizes the bulk equivalent hardness from the nanoindentation tests and Nix-Gao fitting. The negligible influence of the dose rate on the hardness of irradiated samples is evident. Under 0.37 dpa, the bulk equivalent hardness for 300 and 450 °C irradiated samples regardless of dose rates are close to each other, which will be discussed by the correlation with the microstructures later.

4.3. Ion irradiation as a possible surrogate of neutron irradiation

4.3.1. Cavities and swelling

The TEM under- and over- focus technique was used to characterize the cavities in the T91 and HT9 samples. For the ion irradiated samples, the quantitative analysis was conducted at depths 800-1200 nm beneath the specimen surface. For the neutron irradiated sample, several random regions were selected to obtain the average cavity density and size. The characterization results are shown in Fig. 4.18 and Fig. 4.19. All the images are shown in under-focus conditions for better contrast. To distinguish the cavities, the quantitative analysis was performed on cavities with diameter larger and less than 2nm separately. In this study, for simplicity the cavities < 2nm will be referred to “small cavities”, and the ones > 2 nm will be

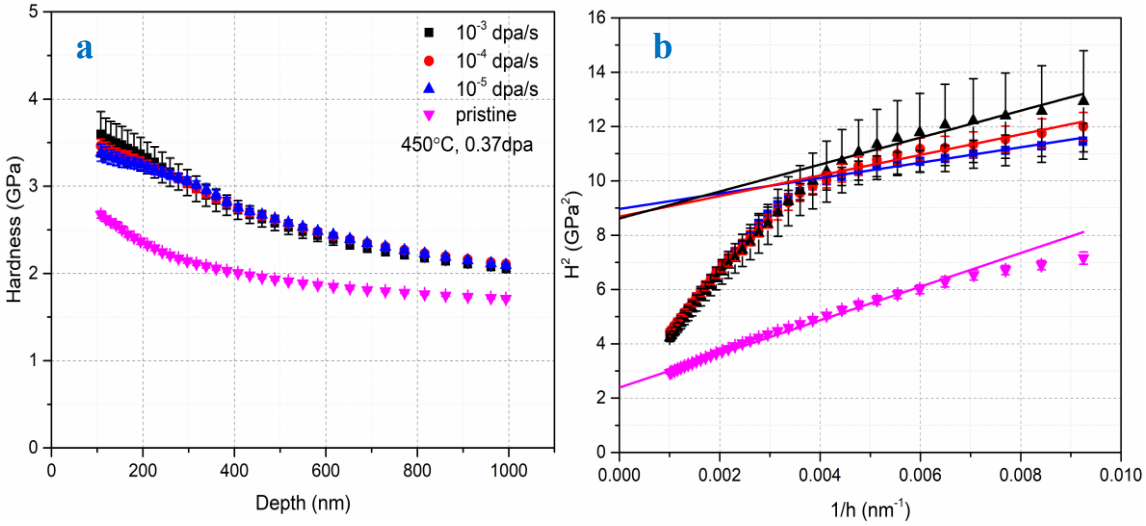

Fig. 4.17 The nanoindentation results of Fe18Cr irradiated at 450 C, 0.37 dpa with different dose rates. (a) Hardness vs. depth. (b) Nix-Gao fitting of the depth dependent hardness.

Table 4.9 Summary of the bulk equivalent hardness (GPa) of the investigated Fe18Cr alloys from nanoindentation measurement.

Final dose (dpa)		0.37		3.7	
Temperature (°C)	300	350	450	350	450
10^{-3} dpa/s	3.04	2.40	2.94		
10^{-4} dpa/s	2.94	2.49	2.95	3.05	2.65
10^{-5} dpa/s			2.99		

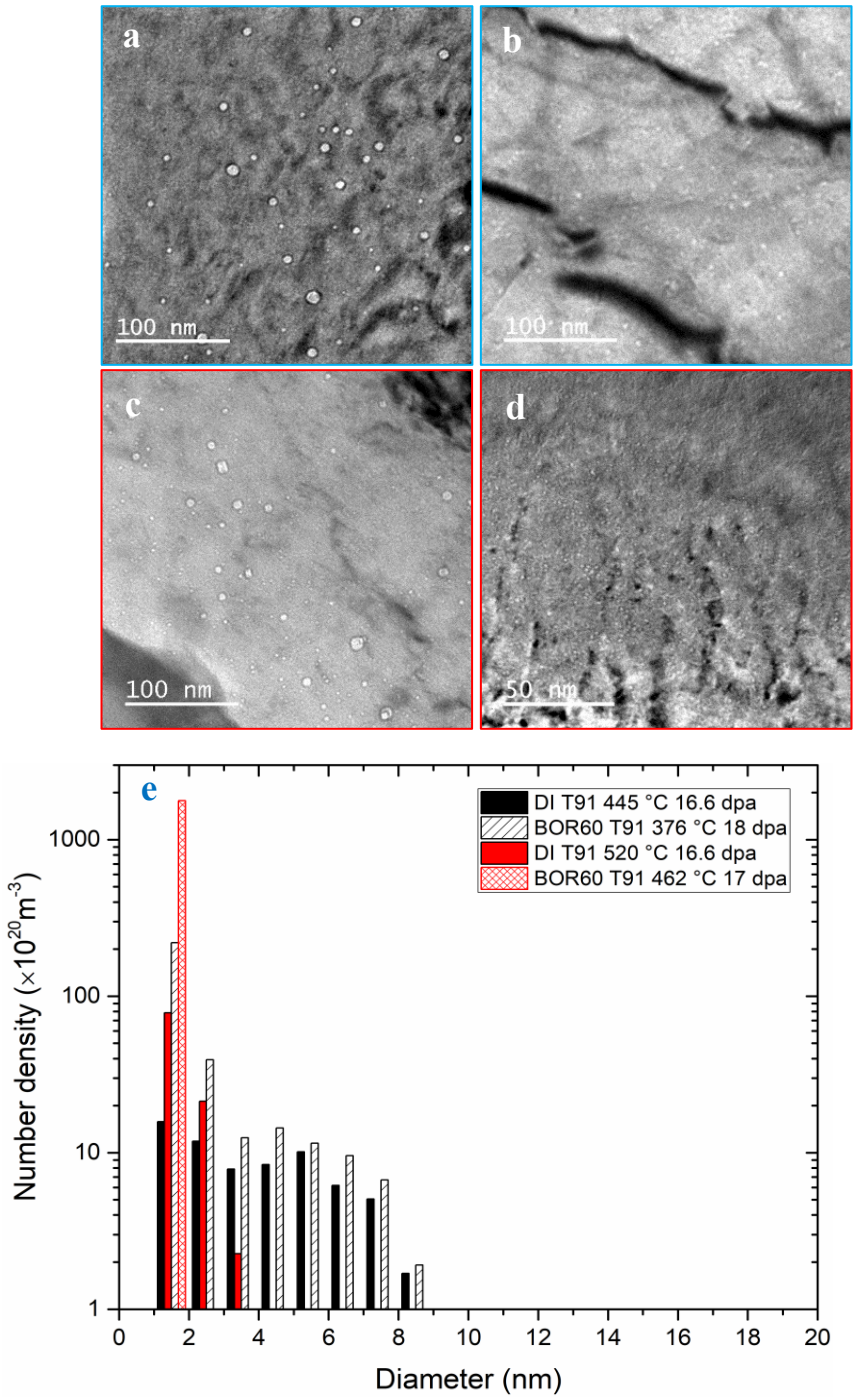

Fig. 4.18 Cavities distribution in dual ion and neutron irradiated T91 alloys. (a) dual ion T91:445℃:16.6dpa. (b) dual ion T91: 520℃:16.6 dpa. (c) neutron T91: 376℃:18dpa. (d) neutron T91: 462℃:17dpa. (e) size distribution of the cavities.

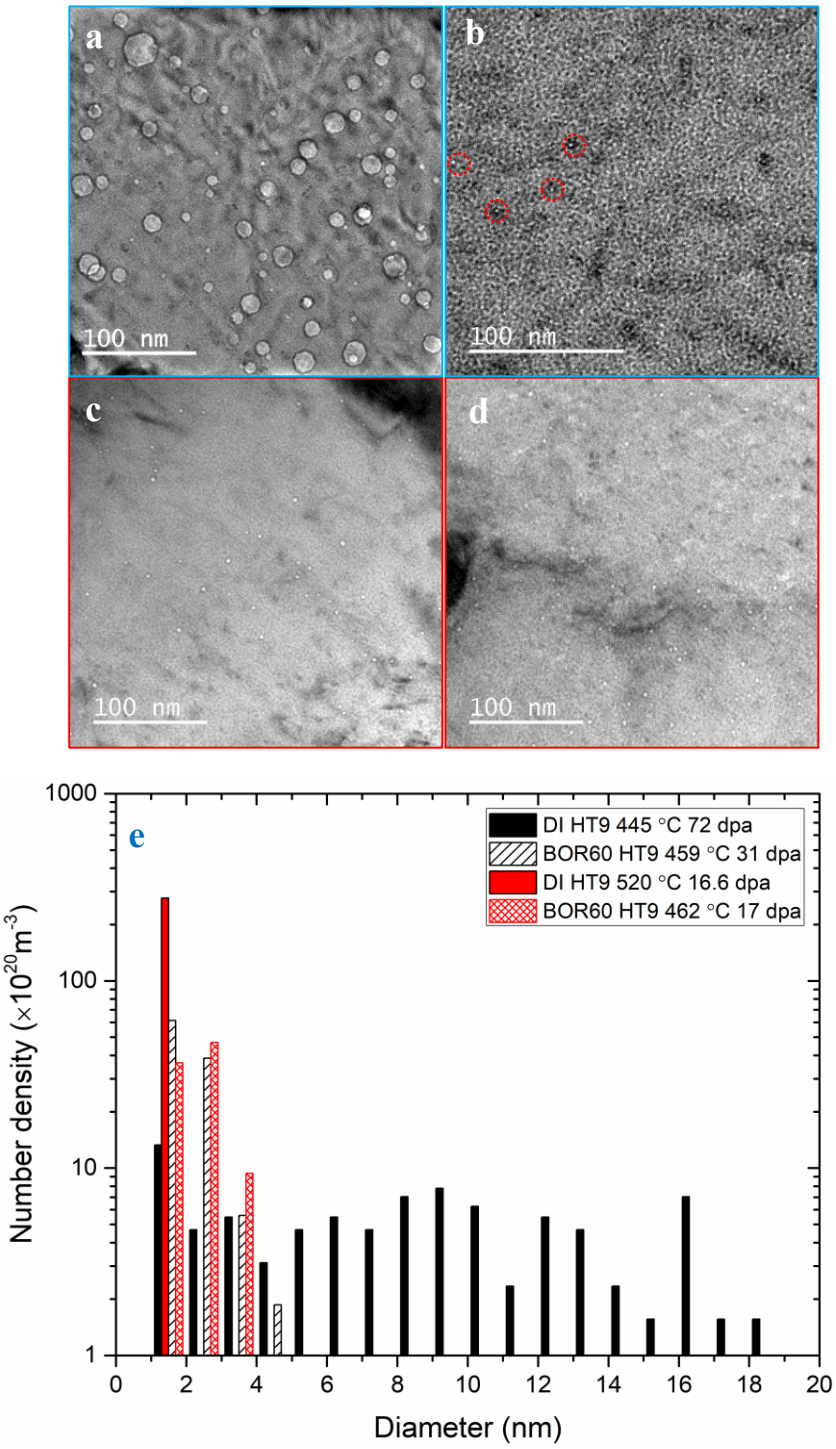

Fig. 4.19 Cavities distribution in dual ion and neutron irradiated HT9 alloys. (a) dual ion HT9:445℃:72dpa. (b) dual ion HT9: 520℃:16.6 dpa. (c) neutron HT9: 459℃:31dpa. (d) neutron HT9: 462℃:17dpa. (e) size distribution of the cavities.

called “large cavities”.

Under dual ion irradiation at 445 ℃ to 16.6 dpa, the T91 sample exhibits a high density of cavities with different sizes as shown in Fig. 4.18a. Generally, the cavities were distributed homogeneously in the matrix. The large cavities have an average diameter of 4.9 ± 0.22 nm, with a high density of 12.8 ± 1.76 × 10^{21} m^{-3}. For the small cavities, the density is only about 1/3 of the large ones. When increasing the irradiation temperature to 520 ℃ , the size of the large cavities strongly decreased to a diameter of 2.41 ± 0.26 nm and the change in cavity density was insignificant. However, the density for small cavities increased by an order of magnitude without pronounced size change compared with T91 at 460 ℃ and 16.6 dpa. The high temperature may promote the diffusion of He-vacancy clusters and induced a large number of small cavities. Fig. 4.18c and 4.18d show the cavities in neutron irradiated T91 samples, with a temperature shift of about 60 ℃ compared with the dual ion irradiation. Under 376 ℃ and 18 dpa, both large and small cavities were observed in the neutron irradiated T91 sample. Compared with Fig. 4.18a for dual ion irradiated T91 at 445 ℃, neutron irradiation at 376 ℃ produced similar density of large cavities, but with almost an order of magnitude higher density of small cavities. Irradiation in BOR 60 reactor at an even higher temperature of 462 ℃ resulted in small cavities with an extremely large density of 1.78 ± 0.46 × 10^{23} m^{-3}, as shown in Fig. 4.18d. The image was enlarged for better presentation. No large cavities were observed at this temperature, which is consistent with the cavity behavior in the dual ion irradiation (at 520 ℃).

Fig. 4.18e shows the cavity size distribution in the dual ion and neutron irradiated T91 samples. It’s clear that low temperatures resulted in a wider distribution of the cavity diameter, regardless of irradiation type. For T91, dual ion irradiation at 445 ℃ produced a similar size distribution as neutron irradiation at 376 ℃. However, the 520 ℃ irradiation with Fe and He ions created a slight size increase of the cavities, in contrast with the solely small cavities for neutron irradiation.

For HT9 after dual ion irradiation at 445 ℃ to 72 dpa, predominantly large cavities are observed with a density of 7.89 ± 1.74 × 10^{21} m^{-3}, as shown in Fig. 4.19a. The diameter increased up to 10.2 nm due to the high dose. Small cavities were also observed in this condition but with relatively low density. At 520 ℃ and 16.6 dpa, there were only small cavities in the HT9 sample, as shown in Fig. 4.19b by red circles. The image was presented in a higher magnification for better clarification. Similar with the T91 samples, HT9 irradiated at 520 ℃ produced 20 times higher density of small cavities than the low temperature irradiated samples.

For neutron irradiated HT9 samples, Fig. 4.19c and d show the cavity distribution at 459 ℃ (31 dpa) and 462 ℃ (17 dpa), respectively. Both samples show the comparable size of the large cavities (2.58 vs. 2.63 nm), which is totally different from the dual ion irradiated HT9 sample with no large cavities (520 ℃). The density of small cavities for the neutron irradiated samples is less than the 520 ℃ dual ion irradiated ones. The presence of large cavities and decrease of small ones may be caused by the coalescence of small cavities to large ones under neutron irradiation due to the lower damage rate. Fig. 4.19e presents the size distribution of the cavities in HT9 samples. The cavities in dual ion irradiated HT9 sample at 445 ℃ to 72 dpa exhibit a wide range of sizes. This indicates that the accumulation of the damage dose may enhance the coalescence of cavities in the whole matrix. For the neutron irradiation to two different doses and at a close temperature (459 and 462 ℃), the size distribution matches well regardless of doses (17 vs. 31 dpa). It can be referred that the irradiation temperature is the dominant factor in the formation and growth of cavities for the investigated irradiation conditions.

Table 4.10 and 4.11 summarize the quantitative results of the cavities under dual ion and neutron irradiation in the investigated T91 and HT9 samples.

4.3.2. Dislocation microstructures

To clarify the dislocation loop type in the investigated materials, the dislocation-loop map method was used. Either [100] or [110] zone axis was tilted under TEM to characterize the <100> and 1/2<111> loops, which are the two dominant dislocation types in bcc iron alloys. Fig. 4.20 shows the diagram of the possible loops under [100] and [110] zone axes. By comparing this diagram with the corresponding TEM images, the dislocation loop can be distinguished by the alignment and shape.

Fig. 4.21 shows the dislocation distribution in the dual ion and neutron irradiated T91 samples. The images only present the microstructures in the safe region for ion irradiation, namely 800-1200 nm beneath the irradiated surface. The simplified maps were inserted into each image for better understanding. Pre-existing dislocation lines were observed in all the investigated materials, with a density on the order of 10^{14} m^{-2}. For dual ion irradiated T91 at 445 ℃ to 16.6 dpa, both <100> and 1/2<111> loops were characterized, as marked by the yellow and red arrows in Fig. 4.21a, respectively. The mutually vertical <100> loops are distributed in [002] and [020] directions, while the long axis of the 1/2<111> loop is aligned along the $[0\bar{1}1]$ direction. It's evident that the <100> loops are the dominant type, with both

Table 4.10 The cavity number density and size under dual ion irradiation for T91 and HT9 samples.

Materials	Temperature	Dose	Cavity size >2nm		Cavity size <2nm		void swelling
	℃	dpa	Average diameter (nm)	Number density ($\times10^{21}m^{-3}$)	Average diameter (nm)	Number density ($\times10^{21}m^{-3}$)	
T91	445	16.6	4.90 ± 0.22	12.8 ± 1.76	1.63 ± 0.07	3.86	0.049%
	520	16.6	2.41 ± 0.26	9.42 ± 1.02	1.50 ± 0.04	35.5 ± 12.8	0.014%
HT9	445	72	10.17 ± 1.04	7.89 ± 1.74	1.46 ± 0.16	1.33 ± 0.30	0.788%
	520	16.6	-	-	1.38 ± 0.26	27.7 ± 4.20	0.0042%

Table 4.11 The cavity number density and size under neutron irradiation for T91 and HT9 samples.

Materials	Temperature	Dose	Cavity size >2nm		Cavity size <2nm		void swelling
	℃	dpa	Average diameter (nm)	Number density ($\times10^{21}m^{-3}$)	Average diameter (nm)	Number density ($\times10^{21}m^{-3}$)	
T91	376	18	4.18 ± 1.14	11.1 ± 4.15	1.33 ± 0.27	22.1 ± 7.22	0.06%
	462	17	-	-	0.94 ± 0.22	178 ± 46	0.009%
HT9	459	31	2.63 ± 0.12	4.60 ± 1.30	1.57 ± 0.04	6.13 ± 2.06	0.0084%
	462	17	2.58 ± 0.30	4.22 ± 2.20	1.66 ± 0.06	3.28 ± 2.89	0.0044%

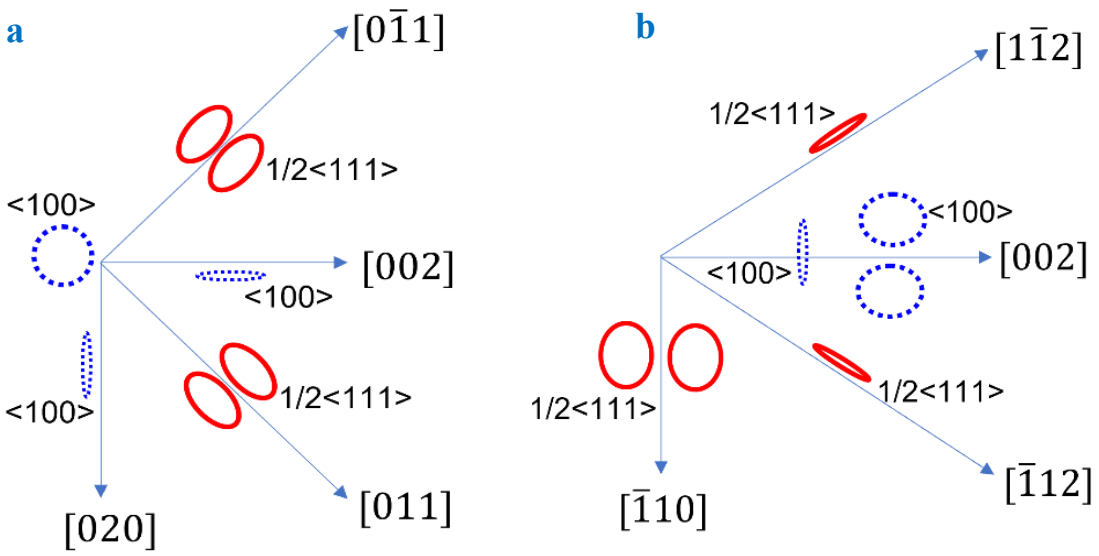

Fig. 4.20 Dislocation-loop map for bcc-Fe under (a) [100] zone axis and (b) [110] zone axis.

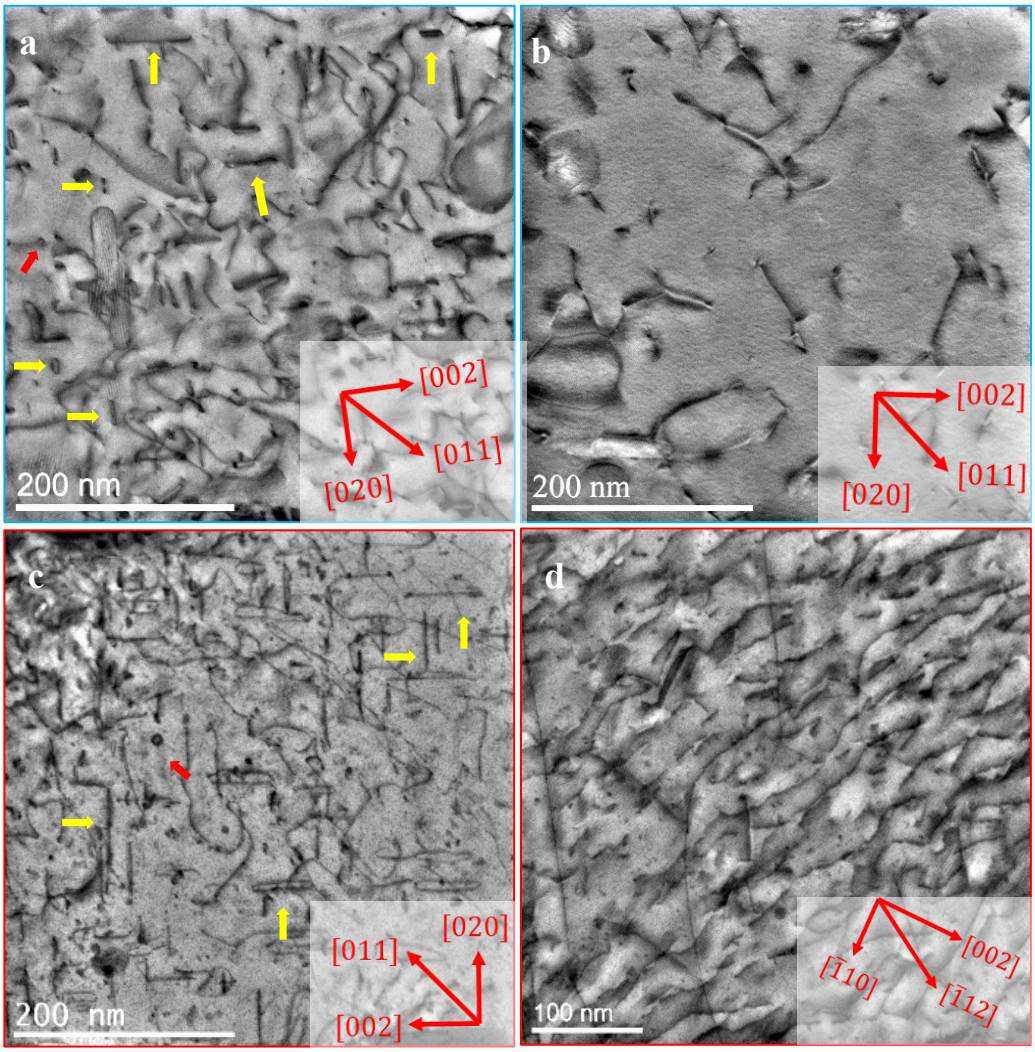

Fig. 4.21 STEM-BF images of the dislocation lines and loops in the dual ion and neutron irradiated T91 samples. (a) dual ion T91: 445℃: 16.6dpa, on [100] zone. (b) dual ion T91: 520℃: 16.6dpa, on [100] zone. (c) BOR 60 T91: 376℃: 18dpa, on [100] zone. (d) BOR 60 T91: 462℃: 17dpa, on [110] zone.

larger density and size compared with the 1/2<111> loops. At a higher irradiation temperature of 520 ℃, however, there are no observed dislocation loops in the T91 sample after 16.6 dpa, with only dislocation lines and segments, as illustrated in Fig. 4.21b. Fig. 4.21c and d show the neutron irradiated microstructures in T91. Dislocation loops were observed in the sample that was irradiated at 376 ℃ to 18 dpa, while only dislocation lines exist for the 462 ℃ irradiation. For a better illustration of the dislocation loops, the 376 ℃ sample was tilted to g = 011 under [100] zone axis. According to the g·b criterion, the edge-on loops represented 2/3 of the total <100> loops, and half of the 1/2<111> loops can be imaged under this condition. Fig. 4.22 compares the dislocation loop evolution between neutron and dual ion irradiation with a temperature shift about 60 ℃. The average <100> loop size increases from 17.3 nm for dual ion irradiation to 30.07 nm for neutron irradiation. However, neutron irradiation at 376 ℃ produced similar 1/2<111> loop size with dual ion irradiated T91 at 445 ℃ and 16.6 dpa. The number densities of both loop types are consistent between the neutron and dual ion irradiations.

For the two dual ion irradiated HT9 samples as shown in Fig. 4.23a and b, dislocation loops were observed but with a totally different ratio of <100> type to 1/2<111> type. Under 445 C and 72 dpa, the high dose may promote the growth of the <100> dislocation loops, with an average size of 34.3 ± 13.1 nm. The error reflects the wide range of the loop sizes. And no 1/2<111> loops were observed at this medium-low temperature and high dose. Fig. 4.23b shows the edge-on and semi-open loops at 520 ℃ and 16.6 dpa, as illustrated by the yellow and red arrows, respectively. The STEM-BF image was taken at [110] zone axis, which is different with the other three samples. Although the loops are all along the $[\bar{1}10]$ direction, they may be distinguished by the shapes. The edge-on loops are more likely the <100> loops, while the semi-open ones may refer to the 1/2<111> category. The <100> loop only accounts for 57% of the total loops compared to 100% under the 445 ℃ and 72dpa. However, dislocation loops were not observed in the neutron irradiated HT9 samples with a temperature shift about 60 ℃ compared to the 520 ℃ ion irradiated one, as indicated in Fig. 4.23c and d. Table 4.12 and 4.13 summarizes the quantitative data for density and size of the dislocation loops and lines in the investigated samples.

4.3.3. Precipitates and radiation induced segregation

The precipitates and radiation induced segregation were characterized by EDS mapping. For dual ion samples, the characterization was performed at the safe analysis region in the

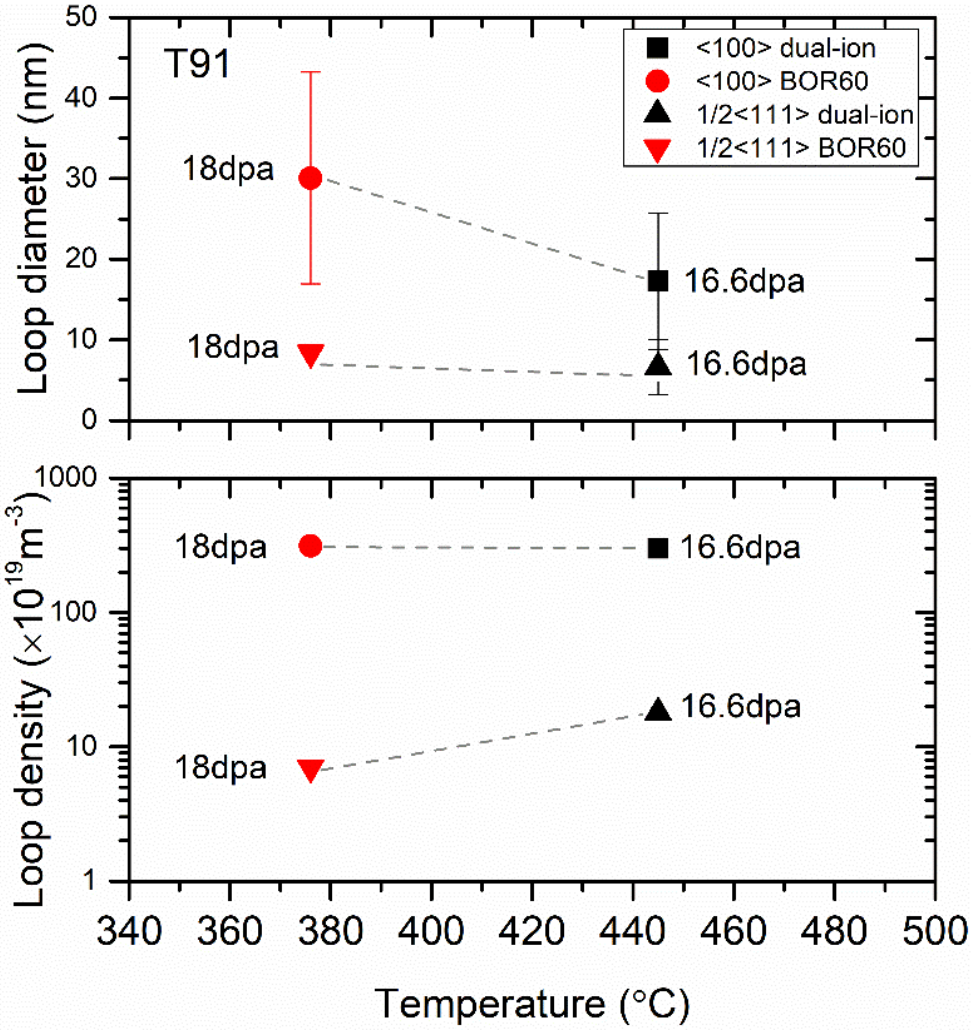

Fig. 4.22 Comparison of loop density and size between dual ion and neutron irradiation for T91 samples.

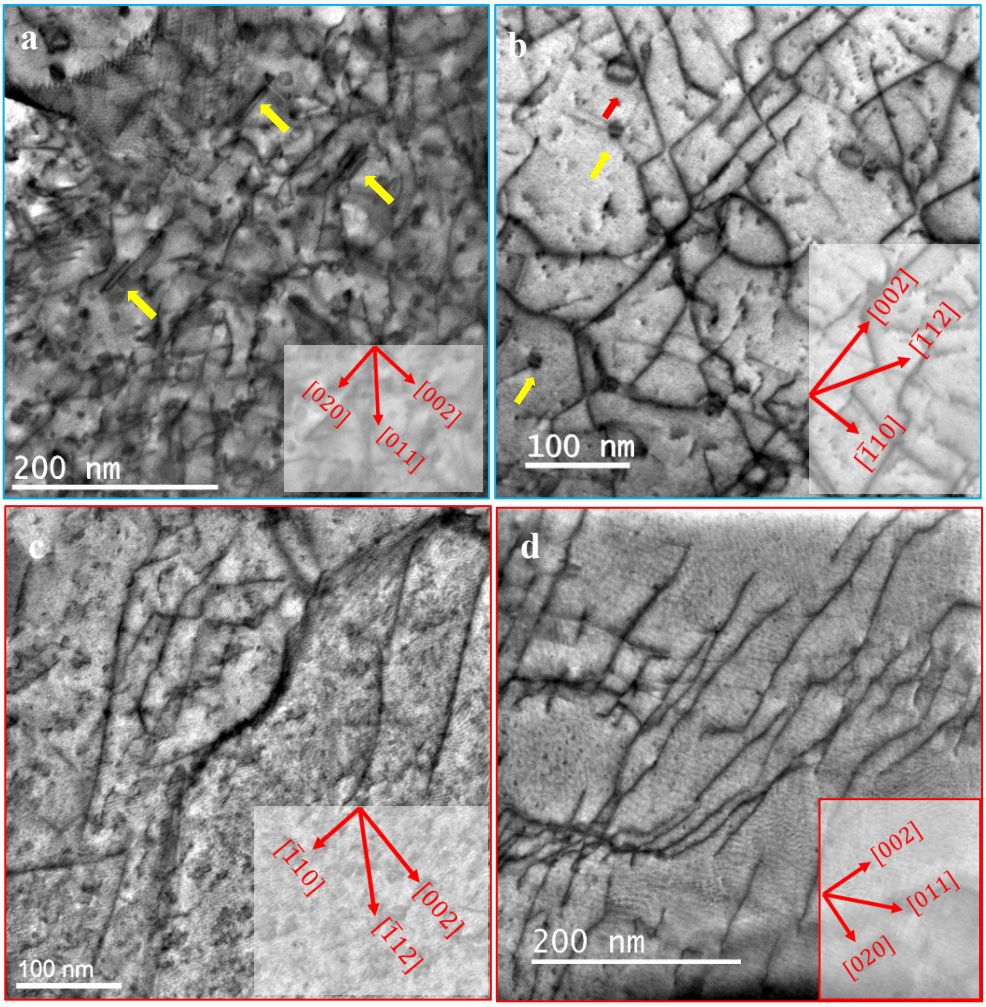

Fig. 4.23 STEM-BF images of the dislocation lines and loops in the dual ion and neutron irradiated HT9 samples. (a) dual ion HT9: 445℃: 72dpa, on [100] zone. (b) dual ion HT9: 520℃: 16.6dpa, on [110] zone. (c) BOR 60 HT9: 459℃: 31dpa, on [110] zone. (d) BOR 60 (C32) HT9: 462℃: 17dpa, on [100] zone.

Table 4.12 The dislocation loop number density and size, as well as the dislocation line density in the dual ion irradiated T91 and HT9 alloys.

Materials	Temperature	Dose	<100> loop		1/2<111> loop		Dislocation line
	℃	dpa	Average diameter (nm)	Number density ($\times10^{21}m^{-3}$)	Average diameter (nm)	Number density ($\times10^{21}m^{-3}$)	Density ($\times10^{14}m^{-2}$)
T91	445	16.6	17.3 ± 8.5	3	6.6 ± 3.4	0.18	4.3
	520	16.6	-	-	-	-	2.7
HT9	445	72	34.3 ± 13.1	1.64	-	-	4.4
	520	16.6	10.4 ± 2.4	0.54	31.0 ± 11.3	0.41	4.8

Table 4.13 The dislocation loop number density and size, as well as the dislocation line density in the neutron irradiated T91 and HT9 alloys.

Materials	Temperature	Dose	<100> loop		1/2<111> loop		Dislocation line
	℃	dpa	Average diameter (nm)	Number density ($\times10^{21}m^{-3}$)	Average diameter (nm)	Number density ($\times10^{21}m^{-3}$)	Density ($\times10^{14}m^{-2}$)
T91	376	18	30.1 ± 13.1	3.1	8.4	0.07	4.0
	462	17	-	-	-	-	4.2
HT9	459	31	-	-	-	-	3.4
	462	17	-	-	-	-	3.6

range of 800-1200 nm, while for the neutron irradiation, the mapping was conducted at random positions. Overall, the pre-existing carbides containing Cr, Mn, V, etc. and V-rich nitrides were observed in all the dual ion and neutron irradiated T91 and HT9 samples. According to the previous studies, the carbides can be inferred as $M_{23}C_6$, and will not be discussed in this study. After irradiation, multiple microstructures were observed: Ni/Si-rich precipitates and G-phase in the matrix and on the grain boundaries, enrichment of Ni and enrichment or depletion of Cr on the grain boundaries, segregation of Ni around the dislocation lines, replacement of Cr by Ni in the carbides, etc. Fig. 4.24 illustrate the distribution of Ni-rich clusters in the dual ion irradiated HT9 at 445 ℃ and 72 dpa. In the irradiated region from the surface to about 2.5 um, a large number of Ni-clusters were observed, while there are clearly no clusters beyond. This demonstrates that the Ni-rich clusters were induced by the irradiation, which will contribute to the irradiation strengthening.

For dual ion irradiated T91 under 445 ℃ and 16.6 dpa, there is no clear Ni precipitation in the matrix, but a slight segregation of Ni and Si may occur on the grain boundary as shown by the yellow arrows in Fig. 4.25. The corresponding T91 sample that was irradiated by neutrons at 376 ℃ and 18 dpa was also included in Fig. 4.25. Neutron irradiation produced a large number of precipitates in the matrix containing Ni, Si, and Mn. The (Ni, Si, Mn)-rich clusters were also observed on the grain boundaries. Generally, the ~60 ℃ temperature shift between dual ion and neutron irradiation didn't result in comparable precipitation phenomenon. Fig. 4.26 compares the EDS mapping of dual ion and neutron irradiated T91 samples with a temperature shift of 58 ℃. For both ion irradiation at 520 ℃ and 16.6 dpa, and neutron irradiation at 462C and 17dpa, Ni-rich clusters were not observed.

For dual ion irradiated HT9 under 445 ℃ and 72 dpa, (Ni, Si, Mn)-rich clusters were observed in the matrix as illustrated by the inserted images in Fig. 4.27. At this low temperature and high dose, no comparison can be made between dual ion and neutron irradiation due to temperature shift. Fig. 4.28 compares the irradiation induced precipitates in HT9 samples under both irradiation types. The dual ion irradiation at 520 ℃ and 16.6 dpa produced (Ni, Si)-rich clusters on the grain boundaries, while no precipitation was observed in the matrix. Mn was not segregated in the same region as Ni and Si; instead, Mn was homogeneously enriched on the carbides. By shifting the ion irradiation temperature about 60 ℃, neutron irradiation to both 17 and 31 dpa induced similar (Ni, Si)-rich clusters as the dual ion irradiation on the grain boundaries. Increasing the dose from 17 to 31 dpa didn't change the element segregation performance for neutron irradiation at the similar temperatures (459 vs. 462 ℃). Since the

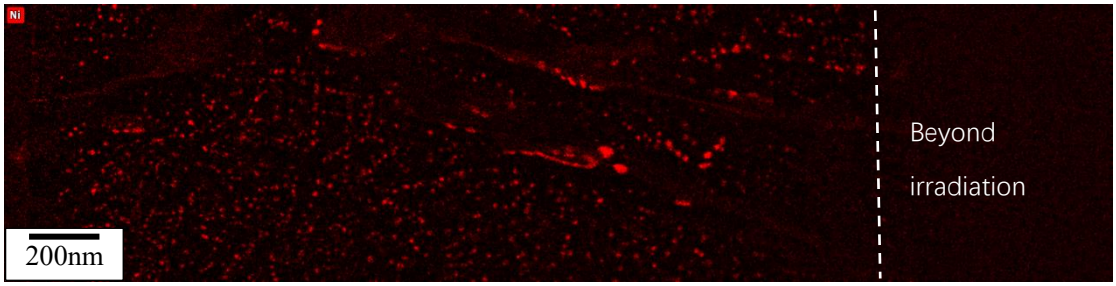

Fig. 4.24 EDS mapping of dual ion irradiated HT9 at 445 ℃ and 72 dpa, showing the Ni-cluster distribution.

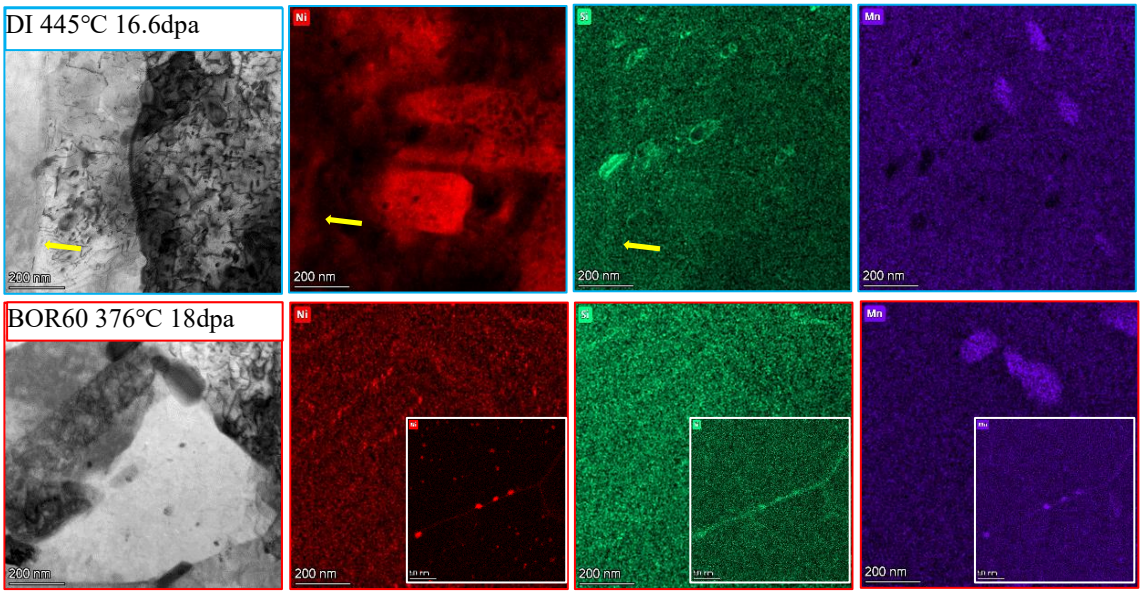

Fig. 4.25 Comparison of Ni, Si, Mn in dual ion and neutron irradiated T91 sample.

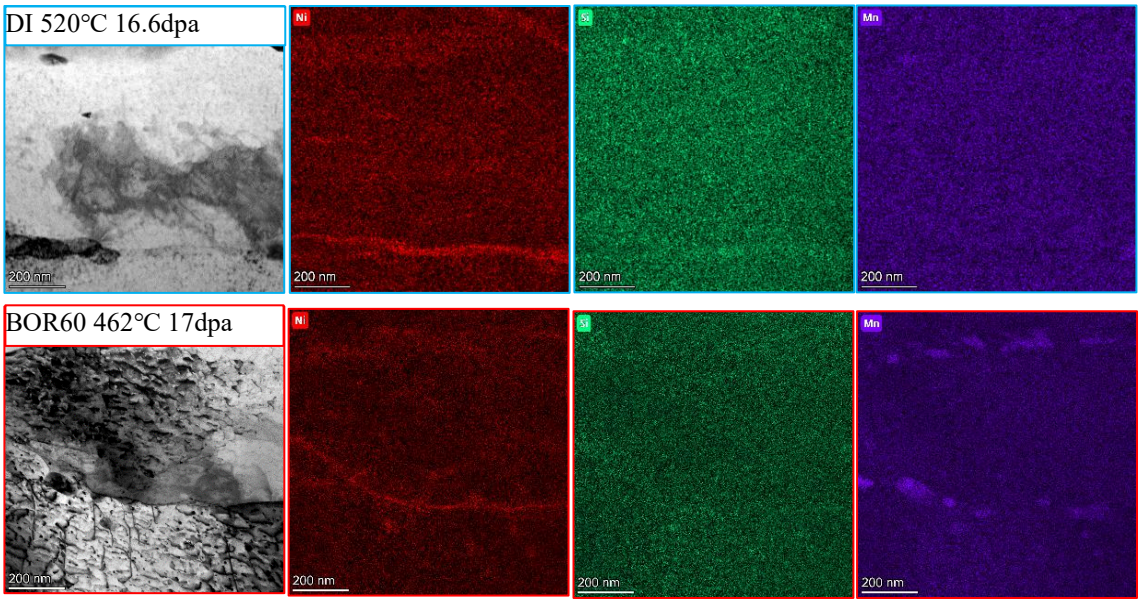

Fig. 4.26 Comparison of Ni, Si, Mn in dual ion and neutron irradiated T91 sample.

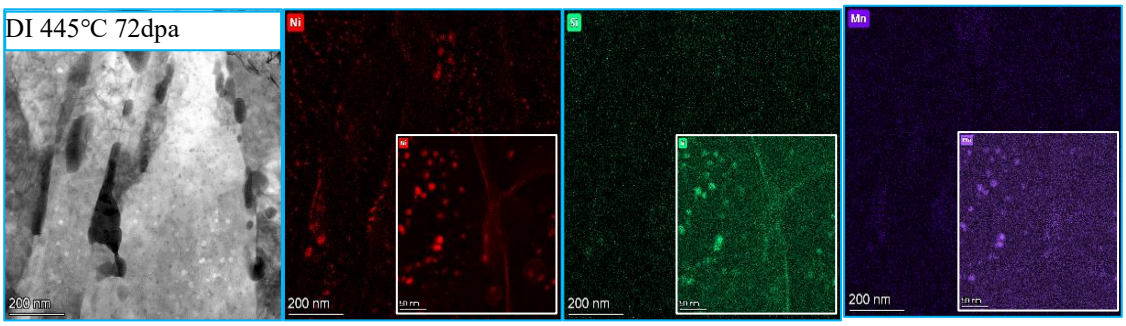

Fig. 4.27 EDS mapping of dual ion irradiated HT9 at 445 °C and 72 dpa.

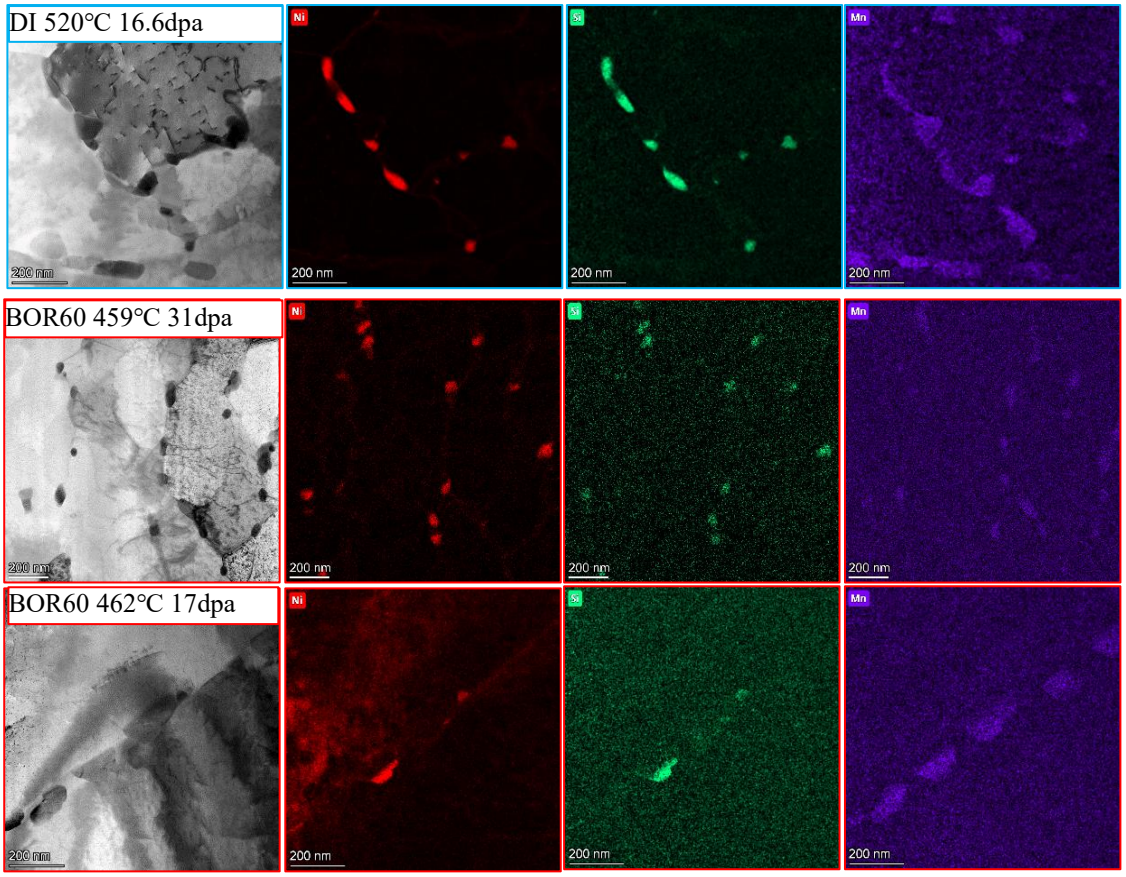

Fig. 4.28 Comparison of Ni, Si, Mn clusters and segregation in dual ion and neutron irradiated HT9 samples.

microstructure characterization for the neutron sample was performed on random regions, it's reasonable the Ni-clusters were not imaged under EDS mapping. Fig. 4.29 shows one STEM-DF image of HT9 under neutron irradiation at 459 ℃ and 31 dpa. The particles with Moire fringes were distributed in the matrix and also on the dislocation lines. Zheng et al. [32] observed the similar features in the neutron irradiated HT9 under 457 ℃ and 14.6 dpa, and clarified that they were (Ni, Si, Mn)-rich G phases. It's inferred that in our study the particles were also G phase. Since the irradiation condition in Ref. [32] is similar to our neutron irradiated HT9 sample at 462 ℃ and 17 dpa, we will simply refer to their quantitative density and size as the data for Ni-clusters.

A typical comparison on the radiation induced segregation between dual ion and neutron irradiation is shown in Fig. 4.30. For HT9 ion irradiated at 520 ℃ to 16.6 dpa, Ni and Si enrichment is observed on the grain boundary, while Mn is depleted at the same region. A consistent segregation of Ni and Si occurred in the corresponding neutron irradiated HT9 at both 459 and 462 ℃. However, neutron irradiation induced Mn enrichment on the grain boundary. This grain boundary enrichment of (Ni, Si) and depletion/homogenous of Mn in dual ion samples, as well as enrichment of (Ni, Si, Mn) in neutron irradiation, were also observed in the other T91 and HT9 samples, as shown in Fig. 4.25-Fig. 4.27. In Fig. 4.26, since Mn segregated on the carbides which were formed on the grain boundary, the enrichment of Mn on the grain boundary is not imaged as clear as expected. However, it can be inferred that the carbides may provide a strong driving force to attract Mn from the grain boundary. Table 4.14 and 4.15 summarize the density and size of the Ni-clusters.

4.3.4. Mechanical properties

Nanoindentation testing was performed on the normal surface of the ion-irradiated samples, and the Nix-Gao model combined with bilinear method were used to extract bulk equivalent hardness of the dual ion irradiated samples [124]. To quantify the effect of pileup, the AFM measurement was conducted on the residual indents and the correction model developed in the prior study [124] was used to improve the accuracy of the measured hardness and modulus. Fig. 4.31 shows the typical Nix-Gao plots of ion-irradiated alloys after applying pileup corrections. There are observable inflections on the T91 irradiated at 445 ℃ and 800H irradiated at 460 ℃, whereas for other alloys irradiated at 520 ℃, there are almost no inflections in the Nix-Gao plot, indicating that the hardening effect is weak at the corresponding irradiation conditions. Even slight irradiation softening at shallow depths occurs for T91

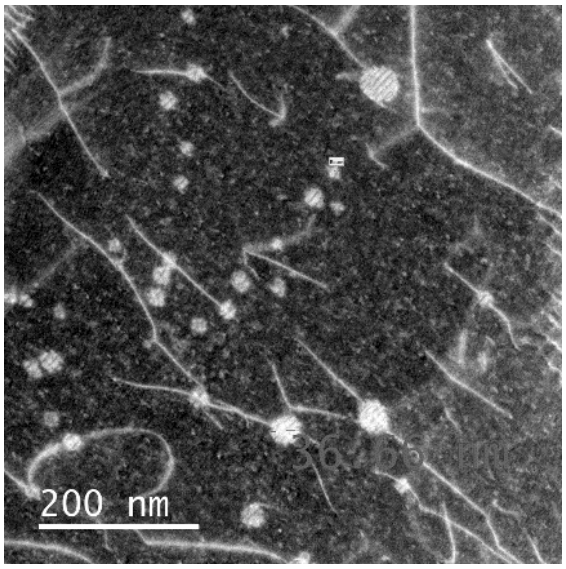

Fig. 4.29 STEM-DF image of neutron irradiated HT9 at 459 ℃ to 31 dpa.

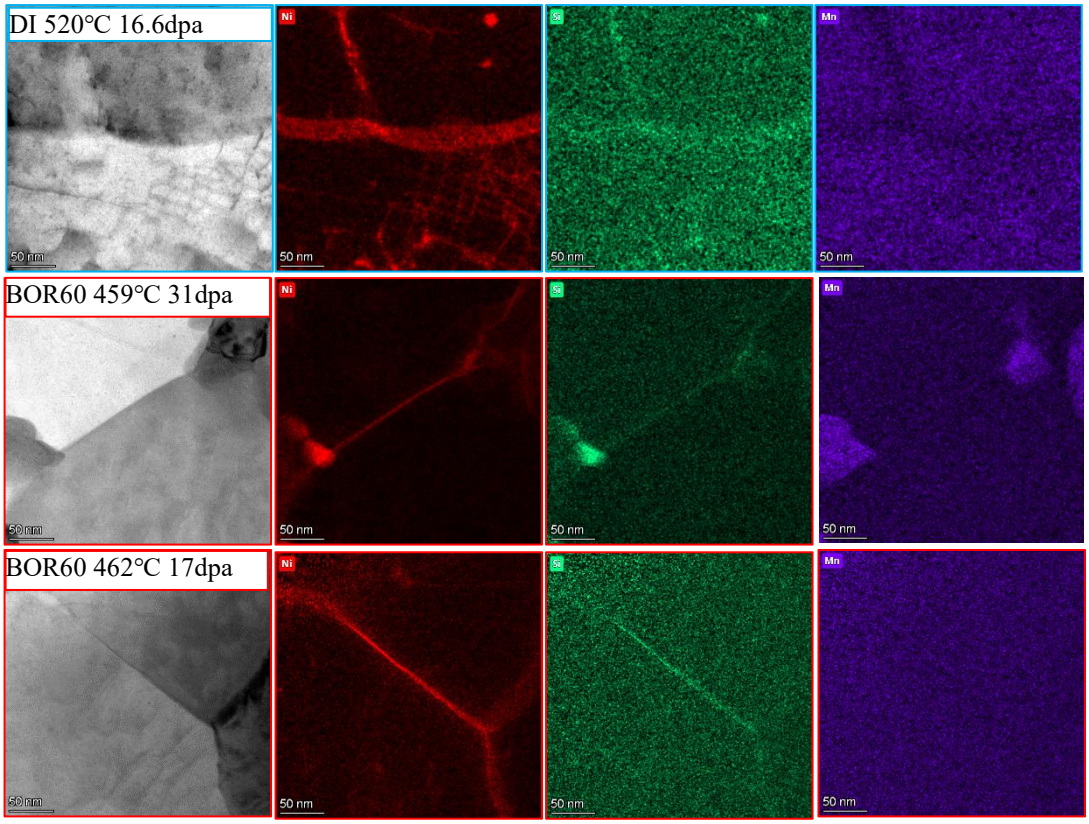

Fig. 4.30 comparison of Ni, Si, Mn segregation on the grain boundary for dual ion and neutron irradiated HT9.

Table 4.14 Size and density of the Ni-rich clusters in the dual ion irradiated T91 and HT9 alloys.

Materials	Temperature	Dose	Ni-rich clusters	
	℃	dpa	Average diameter (nm)	Number density ($\times 10^{21} m^{-3}$)
T91	445	16.6	-	-
	520	16.6	-	-
HT9	445	72	6.3 ± 2.1	5.4 ± 0.4
	520	16.6	-	-

Table 4.15 The Ni-rich clusters size and density in the neutron irradiated T91 and HT9 alloys. (*from TEM images; **from [32])

Materials	Temperature	Dose	Ni-rich clusters	
	℃	dpa	Average diameter (nm)	Number density ($\times 10^{21} m^{-3}$)
T91	376	18	3.7 ± 1.5	5.0 ± 0.2
	462	17	-	-
HT9	459*	31	18.7 ± 7.8	0.7
	462**	17	19.8 ± 2.1	0.7

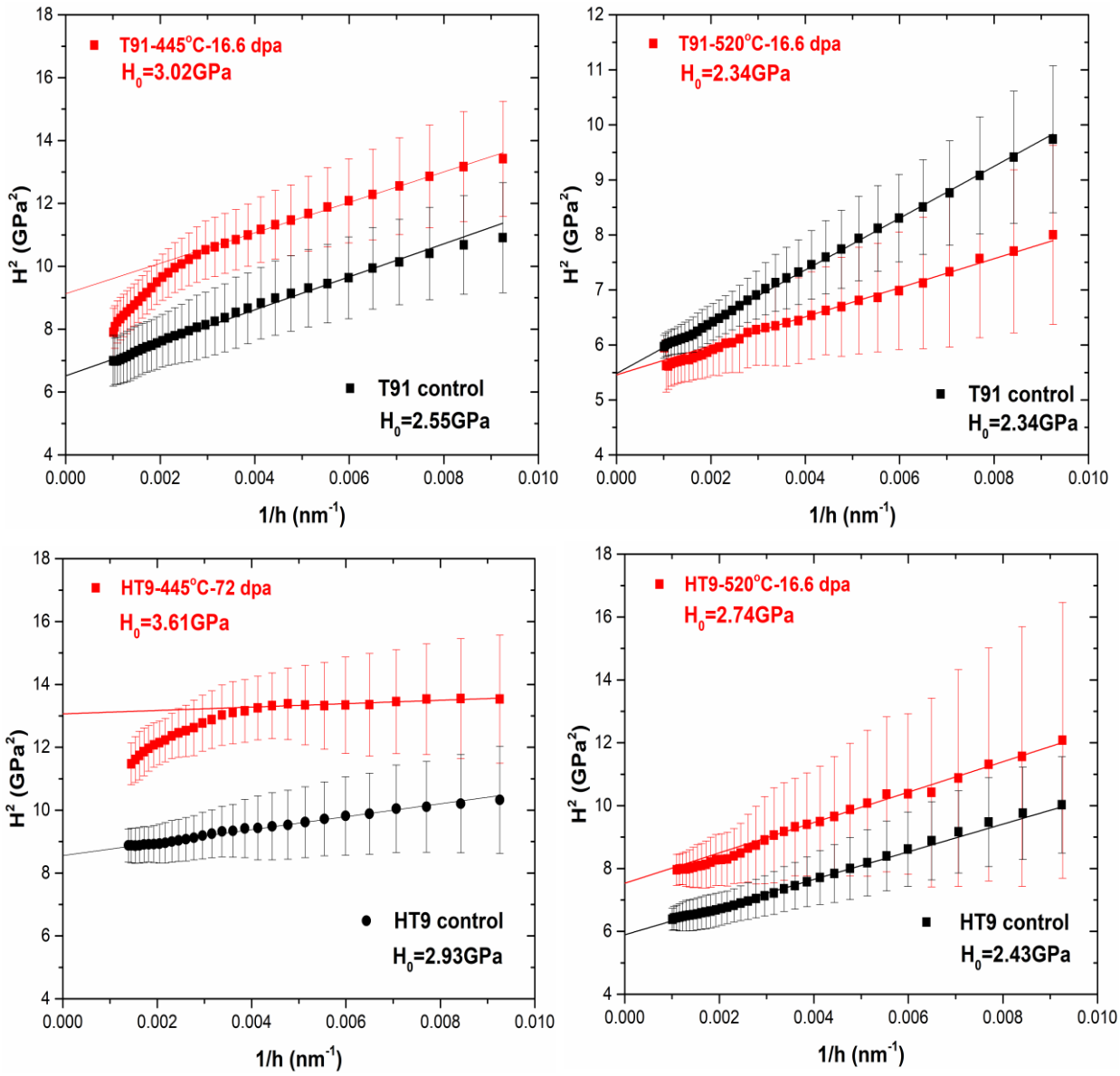

Fig. 4.31 Nix-Gao fitting of the nanoindentation data for the dual ion irradiated T91 and HT9 samples.

irradiated at 520 ℃ to 16.6 dpa. For nanoindentation tests on neutron samples, since the instrument for surface tomography measurement on bulk neutron samples was not available, the pileup was estimated from the dual ion irradiated samples with a temperature shift of ~ 60 ℃. Besides nanoindentation, Vickers hardness tests were applied on the unirradiated region of the dual ion samples and also on neutron irradiated samples. Fig. 4.32 compared the Vickers hardness (H_v) and bulk equivalent hardness (H_0) for the neutron irradiated samples. The data points almost fall on the ideal correlation line, which is considered to be further demonstration of the accuracy of the nanoindentation test protocol used in this study. Table 4.16 and 4.17 summarize the nanoindentation measured bulk equivalent hardness and Vickers hardness of the investigated T91 and HT9 samples in this study.

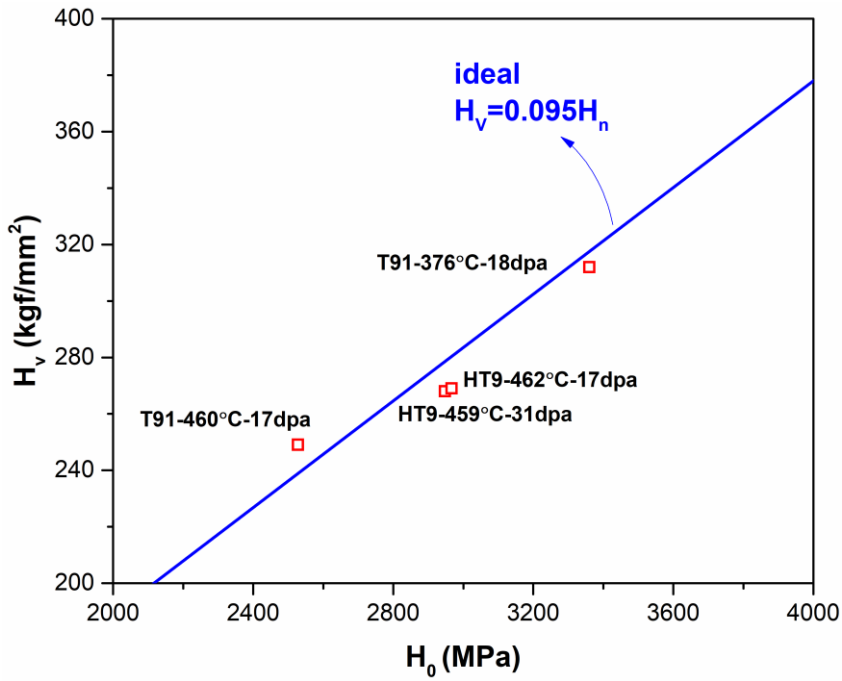

Fig. 4.32 Correlation of Vickers hardness with bulk equivalent hardness for neutron irradiated T91 and HT9.

Table 4.16 Summary of the nanoindentation measured bulk equivalent hardness (H_0) and Vickers hardness of the dual ion irradiated samples. The Vickers hardness for dual ion sample was converted by $H_v = 94.5H_0$. The measured Vickers hardness for the unirradiated region (control) on the same sample is also included in the rightmost column.

Sample	temperature	dose	H_0 (w/o pileup correction)	H_0 (pileup corrected)	pileup correction	$Hv=94.5H_0$	Measured Hv
	℃	dpa	(GPa)	(GPa)		(kgf/mm^2)	(kgf/mm^2)
T91	445	16.6	3.29	3.02	8%	286	-
		control	2.90	2.55	12%	241	247
	520	16.6	2.61	2.34	10%	221	
		control	2.57	2.34	9%	221	235
HT9	445	72	3.82	3.61	5%	341	-
		control	3.16	2.93	7%	277	-
	520	16.6	2.90	2.74	6%	259	-
		control	-	-	-	-	-

Table 4.17 Summary of the nanoindentation measured bulk equivalent hardness and Vickers hardness of the neutron irradiated samples. The estimated pileup correction is from the dual ion samples in Table 4.16 with a temperature shift of ~60 ℃. Both converted Vickers hardness and the measured Vickers hardness are included in the table.

Sample	temperature	dose	H_0 (w/o pileup correction)	Estimated pileup correction	H_0 (pileup corrected)	$Hv=94.5H_0$	Measured Hv
	℃	dpa	(GPa)		(GPa)	(kgf/mm^2)	(kgf/mm^2)
T91	376	18	3.66	8%	3.36	317	312
	462	17	2.82	10%	2.53	239	249
HT9	459	31	3.12	6%	2.94	279	268
	462	17	3.14	6%	2.97	280	269

CHAPTER 5. DISCUSSION

5.1. Nanoindentation test protocol

Nanoindentation tests were initially performed on a variety of as-received and thermally aged FeCr alloys with different Cr content, in order to examine a wide range of hardnesses. The possible effects on the nanoindentation measurement were systematically considered, such as indentation size effect, surface preparation, test methods, grain orientation and pileup. In this section, we will discuss in detail the potential errors in the nanoindentation test and try to develop an accurate way to extract bulk equivalent hardness from nanoindentation data.

5.1.1. Indentation size effect

The indentation size effect has been a long-standing critical issue in nano- and micro-indentation research to extract bulk equivalent hardness for quantitative evaluation [6,80]. Fig. 4.2b exhibits the typical variation of characteristic ISE length scale (h^*) with bulk equivalent hardness. Although exceptions can occur in the material-specific variation of ISE with hardness, an approximately monotonic decrease in h^* with increasing bulk hardness was observed for most of the aged FeCr alloys. Since nanoindentation of most metals is intrinsically accompanied by ISE, obtaining a hardness value at a reference depth or load is generally not representative of the bulk hardness of a given material. Furthermore, it is inappropriate to quantify hardness changes between two different materials or treatments (annealing, irradiation, etc.) without accounting for the ISE, such as directly calculating the ratio or subtraction of hardness at a specific depth on hardness vs. depth curves. For instance, Fig. 5.1a shows the change of raw nanoindentation hardness for Fe18Cr (aged at 900 h minus as-received) obtained by direct subtraction at each depth; the corresponding change in bulk equivalent hardness for these two samples (horizontal dotted line) is included as a reference. It is apparent that for indent depths between 100 and 400 nm, the change of raw nanoindentation hardness exhibits ISE-related errors of 10-30% compared to the change of bulk equivalent hardness extracted by Nix-Gao fitting. Therefore, any attempt to determine the change of bulk hardness values between different materials (e.g., surface-hardened or ion irradiated vs. pristine) directly from raw hardness vs. depth curves will generally cause considerable quantitative errors due to different ISE behavior.

The potential ISE artifacts when quantifying hardness changes should be paid significant attention especially for materials associated with near-surface treatments such as ion irradiation or carburization. Unfortunately, many published studies have used the hardness ratio or change

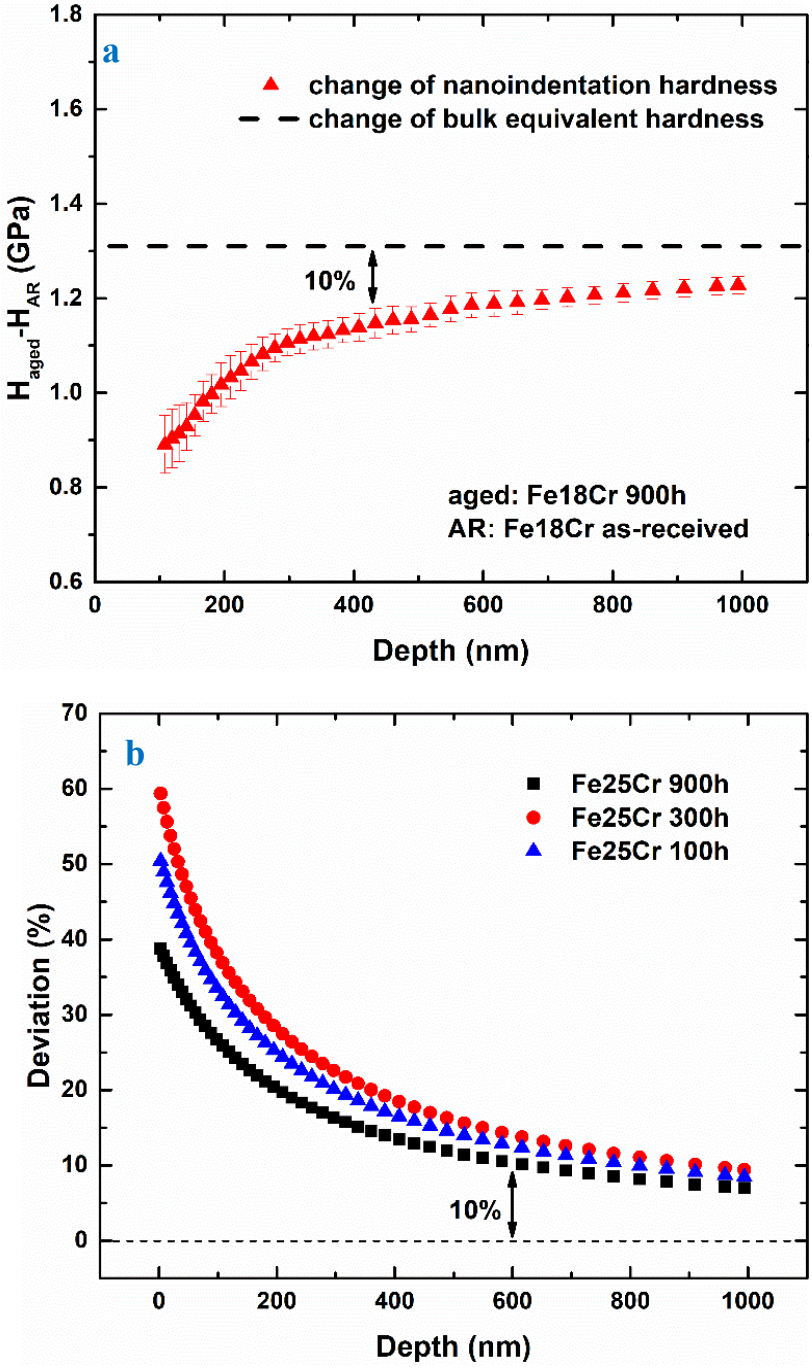

Fig. 5.1 (a) The depth dependence of the change of hardness $\Delta H=H_{aged}-H_{AR}$ calculated from raw nanoindentation hardness at each depth for as-received and 900 h aged Fe18Cr. The change of bulk equivalent hardness for these two samples is plotted as a dashed horizontal line for reference. (b) Deviation of the measured hardness ratio (H_i/H) from the bulk equivalent hardness ratio (H_0^i/H_0) as a function of indent depth (see text accompanying Eq. 5.1).

in hardness value at a specific reference depth as a semiquantitative parameter for evaluating hardness changes [118,125–128]; with this approach, the variable ISE (due to changes in bulk hardness, etc.) will generally introduce significant errors as shown in Fig. 5.1a. It is important to emphasize that the frequent utilization of the ratio of hardness vs. depth for the treated vs. pristine material, such as $H_{irradiated}/H_{un\text{-}irradiated}$, to quantify the hardness increase due to irradiation [129–131] is completely inappropriate. Based on the Nix-Gao model, the ratio of $H_{irradiated}/H_{un\text{-}irradiated}$ can be expressed as below:

$$\frac{H_i}{H} = \frac{H_0^i}{H_0}\sqrt{\frac{h+h_i^*}{h+h^*}} = \frac{H_0^i}{H_0}\sqrt{1-\frac{h^*-h_i^*}{h+h^*}} \tag{5.1}$$

where the subscript/superscript 'i' refers to irradiation (or other treatments such as thermal aging or carburization). Thus, the parameter $(1-\sqrt{1-\frac{h^*-h_i^*}{h+h^*}})$ represents the deviation of the measured hardness ratio from the true bulk equivalent hardness ratio. As previously noted in Fig. 4.2b, the ISE scale parameter (h^*) generally decreases with increasing hardness and therefore considerable errors can arise from this term when the surface-modified hardness is different from the reference hardness of the tested material. This deviation term is shown in Fig. 5.1b for the thermally aged Fe25Cr alloys. For typical ISE scale parameter (h^*) values associated with the aged FeCr alloys, considerable bulk hardness overestimations (10-60%) are introduced compared to the true bulk equivalent hardness ratio for indent depths up to 600-800 nm, depending on the specific alloy. The quantitative error is ~40 to 60% for indent depths near the surface. Therefore, the ratio H_i/H generally cannot provide accurate quantitative estimates of the hardness change due to different characteristic length parameters for the modified and reference material states, i.e., h^* and h^*_i terms in Eq. (5.1); the measured hardness ratio will only equal the bulk equivalent hardness ratio for the unlikely case that $h^* = h^*_i$. Instead of using the quantitatively inappropriate measured hardness ratio, the more physically relevant Nix-Gao model or its subsequent refinements should be used for accurate evaluation of hardness in order to correct for the effect of ISE on raw nanoindentation hardness.

5.1.2. Elastic modulus and hardness strain rate sensitivity

Since the elastic modulus is related to the elastic properties of materials, in contrast to the plastic properties which are associated with indentation size effect, the modulus should be constant with indentation depth. According to Eq. 2.2, any significant variation of the modulus with depth may indicate errors in contact stiffness and/or contact area, which may produce

inaccuracy in the hardness calculated by the Oliver-Pharr method [132]. Achieving a relatively constant modulus during nanoindentation is generally considered as an important criterion to evaluate nanoindentation hardness.

The strain rate sensitivity was evaluated under a series of constant strain rate conditions (which is a convenient option for the iMicro nanoindenter). Alternative methods such as strain-rate jump tests can also be used [133], However, since our materials exhibited substantial indentation size effects the hardness in each strain rate segment would vary (decrease with increasing depth), which complicates the determination of the exact hardness values.

Fig. 5.2a summarizes the effect of strain rate on the apparent modulus for as-received Fe18Cr. For the tests using a constant strain rate of 0.05 /s (45 Hz), a slight increase (<10%) of modulus with depth occurred for the Fe18Cr alloy, while a nearly constant modulus was observed at all depths for the other FeCr alloys in this study at the same test conditions, as shown in Fig. 5.3. The cause of the slight anomalous behavior for the Fe18Cr alloy at 0.05/s is unknown, i.e., it does not seem to be associated with thermal drift or controlled experimental parameters. For the tests at 0.2 /s (45Hz), the modulus varied little with the depth, while the tests at a strain rate of 0.5 /s (45 Hz) showed an apparent decrease of modulus with increasing depth for all the tested specimens. The anomalous decrease in modulus at the higher strain rate of 0.5 /s (45 Hz) is attributed to the lock-in amplifier picking up some component of the semi-static loading and (wrongly) assigning it to the displacement amplitude of the dynamic oscillation; thus the oscillation process is not entirely elastic [134,135]. A characteristic symptom of this anomaly is an increasing phase angle with depth that was detected in our data analysis for the default CSM parameters (0.5 /s, 45 Hz, 2 nm amplitude). This is an indicator of a CSM plasticity electronics error [136] and produces an anomalous decrease of stiffness and modulus [5]. One solution to avoid the anomalous decrease of modulus with depth is to use a higher CSM oscillation frequency. Increasing the CSM oscillation frequency to 110 Hz resulted in constant measured modulus vs. depth (110 Hz) for the 0.5/s strain rate test as shown in Fig. 5.2a. Therefore, we conclude that the decreasing modulus with depth for the 45 Hz, 0.5/s data is only a stiffness measurement artifact (lock-in amplifier anomaly) and is not an indicator of an error in the indenter area calibration. Considering Eq. 2.1-2.3 and that the contact depth h_c is set equal to the total depth h, the artifact in stiffness indicated by the CSM plastic error will not affect the measured hardness in this study. We have confirmed identical values (within ~2%) of bulk hardness H_0 obtained in 0.5/s strain rate tests using CSM

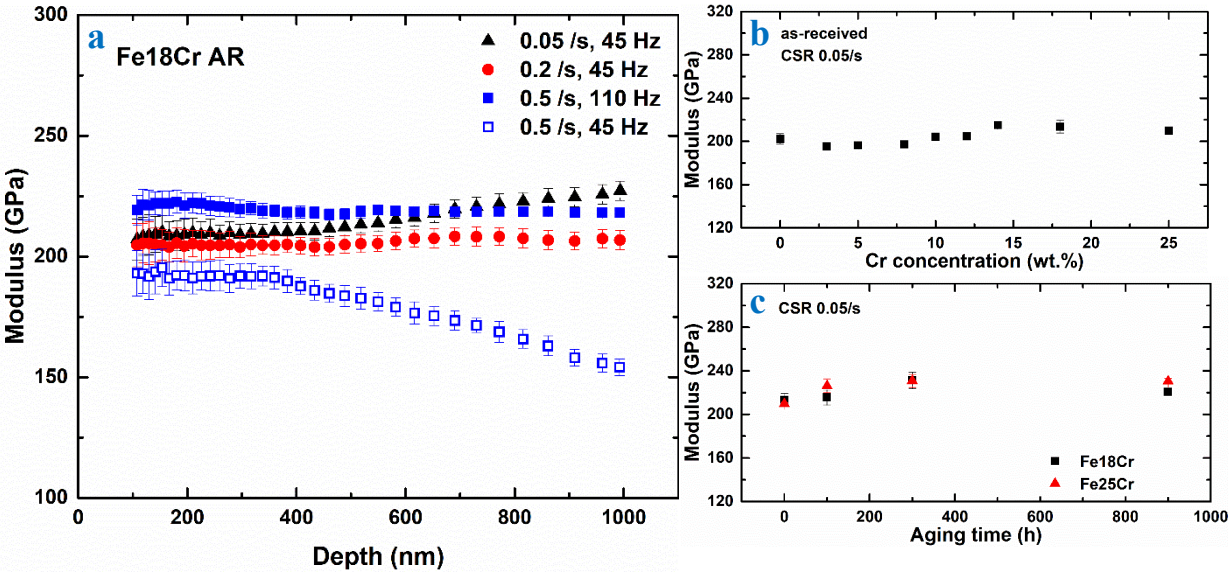

Fig. 5.2 (a) The modulus vs. indentation depth curves of as-received Fe18Cr for CSR tests with strain rates of 0.05, 0.2, 0.5 /s and oscillation frequency of 45 Hz and 110 Hz. The variation of the CSR tested modulus with (b) Cr concentration and (c) thermal aging time of the investigated materials in this study. The modulus data for (b) and (c) are averaged from depths of 100-1000nm.

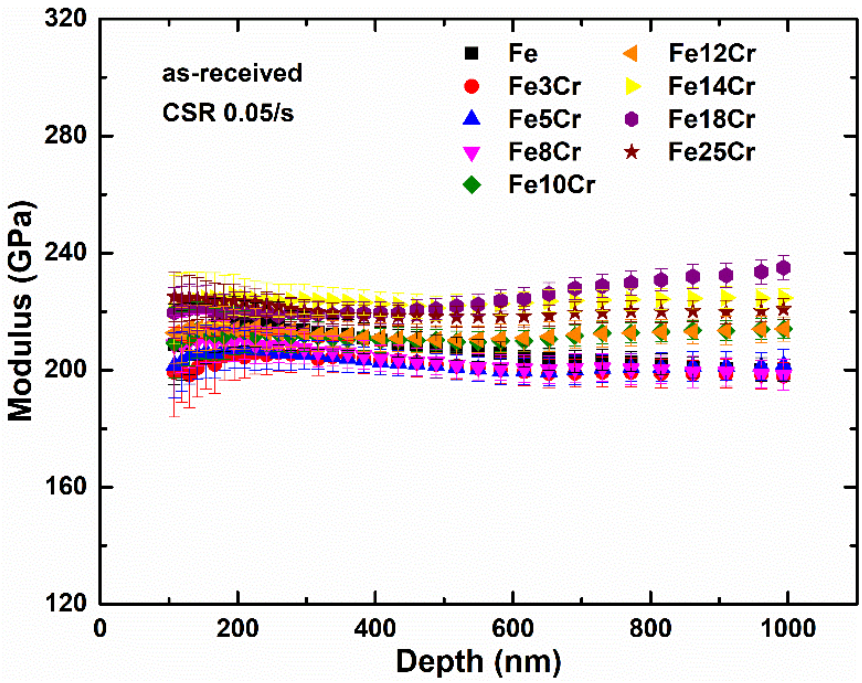

Fig. 5.3 The modulus vs. indentation depth curves of as-received FeCr alloys for CSR tests with strain rates of 0.05 /s and oscillation frequency of 45 Hz.

oscillation frequencies of 45 and 110 Hz.

To quantify the effect of Cr content on the modulus, the average modulus from depths of 100-1000 nm was calculated from 0.05/s strain rate tests; the results are presented in Fig. 5.2b. Overall, the measured modulus was approximately constant for all as-received materials between pure Fe and Fe-25%Cr. A similar negligible dependence of modulus on Cr content was previously reported for FeCr alloys by Speich et al. [137] and Song et al. [138]. Another important topic is the effect of thermal aging on the modulus. For the Fe18Cr and Fe25Cr alloys aged from 100 to 900 hours at 475 ℃ in this study, Fig. 5.2c presents the modulus variation with thermal aging time. A slight increase in elastic modulus from 210 GPa for as-received samples to ~230 GPa after aging was observed for both alloys, which may be caused by the formation of Cr-rich α' precipitates. Most of the increase in modulus was already observed after aging for 100 h; only slight further variation (<5%) of modulus with aging time (100-900 h) was observed. Our observations regarding the slight increase in modulus after thermal aging and weak dependence of aging time in Fig. 5.2c are consistent with prior studies on FeCr alloys [139] and dual phase stainless steel [140] under similar aging conditions. Similar weak effects of precipitates on the elastic moduli have been reported for other (nonferrous) binary alloy systems [141]. Overall, the measured variation of modulus with indentation depth, Cr concentration, and aging time under constant strain rate of 0.05 /s is consistent with expectations for all the thermally aged FeCr alloys in this study, which bolsters confidence in the accuracy of the measured nanoindentation hardness values.

To quantify the effect of variation in strain rate on the nanoindentation hardness, the stain rate sensitivity was evaluated based on a power law relationship described by

$$\sigma = K\dot{\varepsilon}^m \tag{5.2}$$

where σ is the yield stress, $\dot{\varepsilon}$ is the strain rate, K is a material constant, and m is the strain rate sensitivity [142]. In nanoindentation tests, the hardness and strain rate can be considered to be analogous to the tensile stress and strain rate used in Eq. 5.2. Consequently, at a constant temperature, the strain rate sensitivity can be derived as

$$m = \frac{\partial log H_0}{\partial log \dot{\varepsilon}} \tag{5.3}$$

where H_0 is the bulk equivalent hardness extracted by nanoindentation tests, and $\dot{\varepsilon}$ is the strain rate used by the nano indenter [113]. Fig. 5.4 shows the log-log plot of bulk equivalent hardness vs. strain rate for pure iron and as-received and aged Fe18Cr and Fe25Cr samples, in which the slope of the plot equals the strain rate sensitivity (m) as listed at the left end of the curves. A linear relationship was observed between the bulk equivalent hardness and the strain rate for

all of the alloys tested at room temperature. Even the hardness extracted from the tests with a strain rate of 0.5 /s (45 Hz) follows the same monotonic strain rate trend as the two other hardness values from 0.05 and 0.2 /s, confirming that the CSM plasticity error manifests more strongly in the modulus measurements than the hardness [136]. Moreover, the strain rate sensitivity is found to be in the range of m=0.0014-0.0595 for the investigated materials, which is consistent with the results reported for commercial iron and high-purity iron [142,143] tensile tested at room temperature. Overall, the room temperature strain rate effect on the hardness of the materials in the current research is rather weak, which also explains the comparable results between constant strain rate and constant loading rate tests in section 3.3. However, in strain rate sensitive materials the CLR hardness could be significantly affected by the varying strain rate with depth. The CSR method is generally recommended for nanoindentation investigations on the hardness of materials, in order to provide reasonable comparison with tensile tests.

5.1.3. Curvatures in Nix-Gao fitting

Significant curvatures in the region of shallow indent depth (h<~150nm; 1/h>0.006/nm) for the Nix-Gao plots were observed for all the experiments in the current investigation (see Figs. 4.1, 4.3, 4.5b, 4.6b), despite the uniform depth-dependent hardness of all of the tested materials (based on microstructural characterization). Testing using different strain rates, grain orientations, electropolishing, and pileup corrections did almost nothing to eliminate these curvatures (Figs. 4.3, 4.5b, 4.6b, 4.10b), indicating that the experimental test methods are not the origin of the discrepancy between the Nix-Gao model predicted H^2 vs $1/h$ linear behavior and the experimental nanoindentation data. Huang et al. [85] proposed that two aspects may contribute to this discrepancy; one is due to the indenter tip radius, and the other is due to the storage volume for GNDs which are dislocations necessary to accommodate the deformation of materials under the indenter. Oliver and Pharr [144] derived the mathematical area function for the indenter tip in the following form

$$A = \sum_{n=0}^{8} C_n (h_c)^{2^{1-n}} = C_0 h^2 + C_1 h + C_2 h^{\frac{1}{2}} + C_3 h^{\frac{1}{4}} + \cdots + C_8 h^{\frac{1}{128}} \qquad (5.4)$$

where C_0 to C_8 are fitting parameters in determining the area function. The first term represents the perfect Berkovich tip, while the C_1 constant is related to the rounding of the indenter tip. In the current study, the calibrated area function contains two constants, i.e., $C_0=24.24$ and

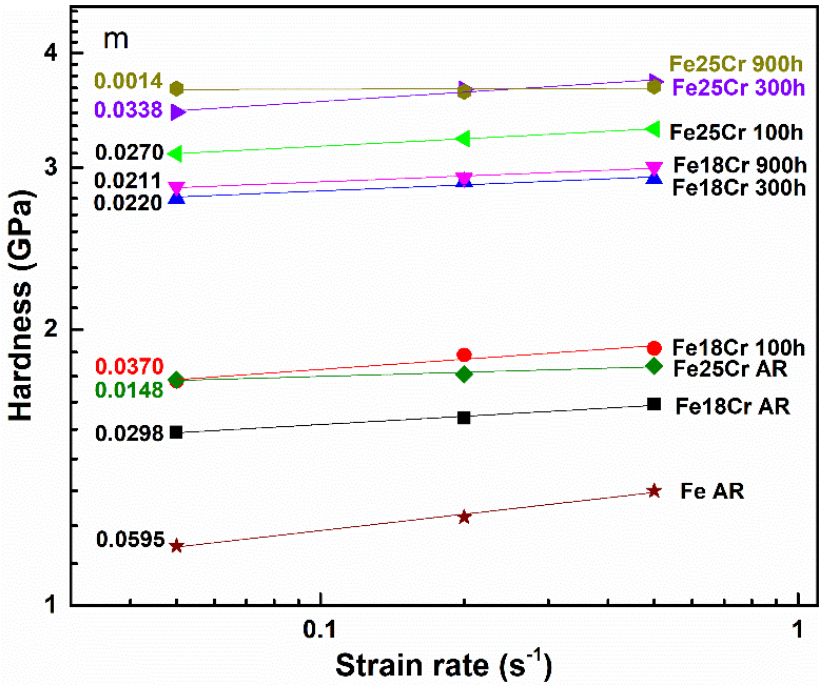

Fig. 5.4 Log-log plot of the hardness dependence on strain rate by nanoindentation tests on the investigated materials. The left end of the curves listed the strain rate sensitivity parameter (m).

C_1=*1090.43*, which implies that the Berkovich nano indenter for this study was slightly rounded at its tip. This rounded tip point modifies the geometrical shape of the perfectly sharp indenter assumed in the Nix-Gao model. Computational work performed by Qu et al. [145] using a conical indenter with a spherical tip also confirmed the deviation of nanoindentation hardness from the Nix-Gao model at very shallow depths due to the tip blunting. A direct comparison of the effect of the indenter area function (ideally sharp vs. blunted) on nonlinearity of the Nix-Gao plots at shallow indent depths is shown in Fig. 5.5. Compared with the area functions calibrated on fused silica and corrected for pileup, the Berkovich ideal area function ($A=24.50h^2$) produces a nearly perfect straight line, whereas the other two area functions produce curvature near 150-200 nm depth. Therefore, the indenter tip rounding may be partially responsible for the observed curvatures in the Nix-Gao plots at low indent depths. However, some other potential factors should also be considered.

Some researchers have questioned the validity of Nix-Gao model assumptions at shallow indentation depths [80,84–86]. In the Nix-Gao model, an important assumption is that all the geometrically necessary dislocations are located in a hemispherical volume under the indenter with the same radius as the contact area of impression, with the corresponding dislocation density described in the Eq. 2.9. As shown in Eq. 2.9, when the indentation depth is small the density of GNDs is extremely large. This close dislocation spacing can induce a high level of mutually repulsive forces between the dislocations, which would drive them to expand beyond the small hemispherical volume [84]. Therefore, the Nix-Gao model may overestimate the density of GNDs that can actually be present at small indent depths and thereby predict a higher modeled hardness than the actual (measured) nanoindentation hardness at very shallow depths (in agreement with our observations of curvature in the Nix-Gao plots below ~150 nm indent depths). Moreover, direct observations and simulation work have shown that the lattice misorientation under the indenter, which is a manifestation of the existence of GNDs, is not constrained in a hemispherical volume with a radius comparable to the indentation contact area radius as assumed by Nix and Gao [92,146,147].

We have observed that the impact of the curvature in the Nix-Gao plots at low indent depths on the bulk equivalent hardness becomes progressively more significant with decreasing bulk hardness. As summarized in Fig. 5.6, the bulk equivalent hardness ratio obtained by fitting data from 100-1000 nm (with curvature) compared to 150-1000 nm and 250-1000 nm (little or no curvature) depths ranged from ~1.05 at a hardness of ~1.5 GPa to <1.01 for hardness

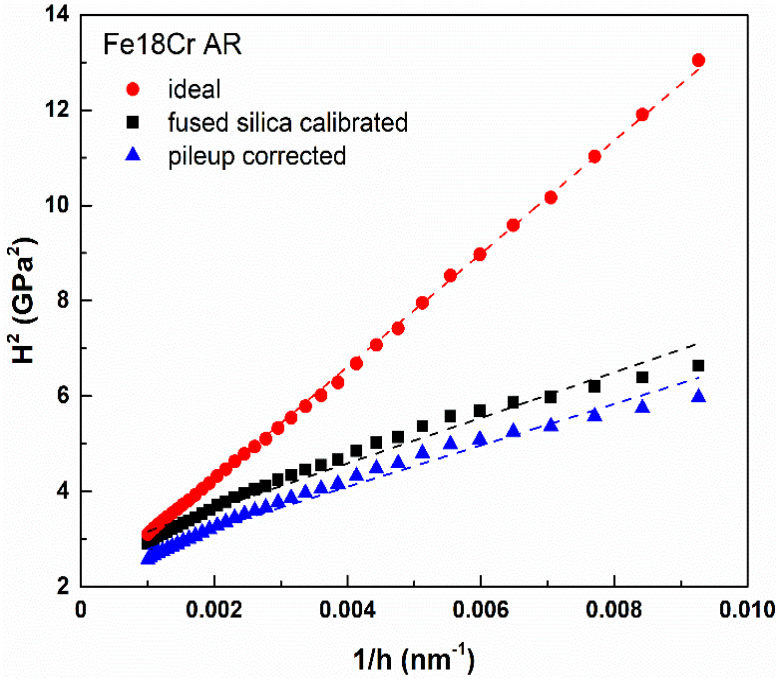

Fig. 5.5 Nix-Gao plots by using ideal, fused silica calibrated, and pileup corrected area functions.

values >2.5 GPa. This may explain the slightly larger deviation between H_V and H_0 for the softer materials in Fig. 5.8a (see section 5.1.4). Regarding the microstructural mechanism, the deviation might be possibly associated with a lack of α' precipitates in the as-received Fe and solution strengthened materials (Fe3-14Cr alloys). As mentioned above, the repulsion force between the dislocations at shallow indent depths may decrease the dislocation density compared to the Nix-Gao assumed GND value. However, the α' precipitates should be effective in pinning the dislocations created during the nanoindentation and may allow the Nix-Gao GND value to be achieved for the aged Fe18Cr and Fe25Cr alloys. For the as-received alloys without α' precipitates, the dislocations may be more easily pushed out beyond the hemispherical indent region, thereby resulting in a pronounced curvature in the H^2 vs. $1/h$ plot and increasing the fitted bulk equivalent hardness. The 100 h aged Fe18Cr might have too small of α' precipitate size to effectively serve as a strong dislocation barrier, and therefore it behaves closer to the solid solution alloys. This hypothesis would need to be confirmed in the future work.

Another consequence of the curvature in Nix-Gao plots at low indent depths is that significant errors may be introduced when trying to obtain quantitative strength values for ion irradiated or surface-modified materials with shallow surface-modified depths. The curvature in the Nix-Gao plots occurred at ~150 nm indent depth for the wide range of pure Fe and Fe-Cr alloys investigated in the current study, whereas other researchers have reported analogous curvatures at indent depths ranging from ~150 to ~600 nm [89,94,104,148]. Considering that elastic strain fields extend to ~5 to 7 times deeper than the indent depth [96], this makes it difficult to extract quantitatively accurate bulk equivalent strength values from surface modified layers less than 1000 nm. For the case of ion irradiation studies of strength changes, this restriction typically requires the use of self-ion energies well above 5 MeV in order to produce irradiated depths of 1000 nm or higher.

Generally, the Nix-Gao model does have some shortcomings in correctly fitting nanoindentation data, especially at very shallow depths (<150 nm for our current study). Although a few refinements on Nix-Gao model have been performed in recent years to describe the GNDs storage under the nano indenter [80,85], additional detailed investigations based on both experiment and simulation are needed to modify the Nix-Gao model in a more physically meaningful way.

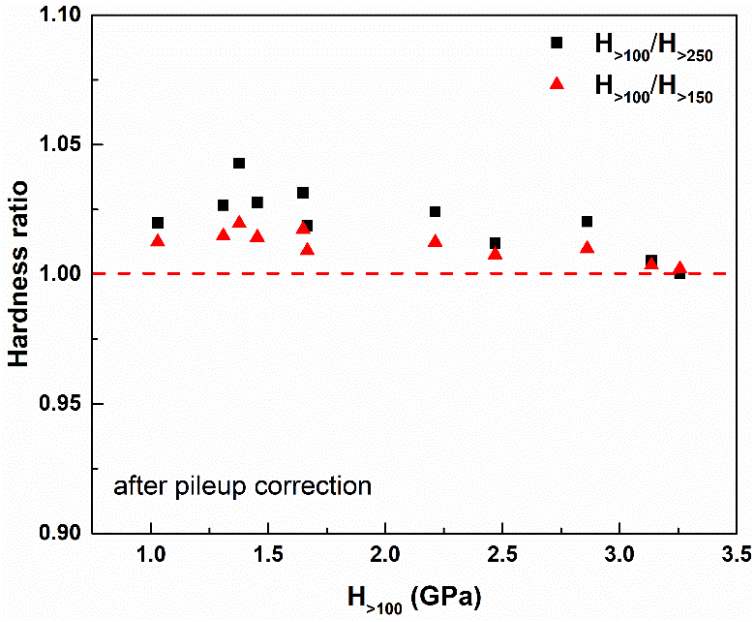

Fig. 5.6 The ratio of Nix-Gao fitted bulk equivalent hardness starting from slightly deeper depth (150 nm ($H_{>150}$) and 250 nm ($H_{>150}$)) and 100 nm ($H_{>100}$) indentation depth for the 16 unique Fe-Cr material conditions examined in this study.

5.1.4. Correlation between Vickers hardness and bulk equivalent hardness

Nanoindentation provides a way to measure the hardness in nanoscale volumes, which is especially important for ion irradiated sample with limited volume to perform bulk testing. After applying Nix-Gao model to the raw nanoindentation data, the ISE is eliminated and the bulk equivalent hardness, H_0, is acquired. Then a question arises whether the fitted H_0 can accurately represent the bulk mechanical properties tested by Vickers hardness testing, and also by tensile testing. Some researchers have performed investigations on the correlation between bulk equivalent hardness and Vickers hardness. As shown in Fig. 1.1, the reported ratio for H_V (kgf/mm^2)/H_n (MPa) is in the range of 0.066 to 0.081 [7–9]. No universal correlation was ever found for H_V/H_0. It is still not well known whether the ratio variation is from experimental artifacts or from a methodology issue for extracting the correct H_0.

In the current study, the h_f/h_{max} of all investigated materials was in the range of 0.91-0.97, and therefore all of the materials are potentially susceptible to significant pileup effects as mentioned in Chapter 2. To provide further confidence to determine pileup by h_f/h_{max} ratio, we compared the A/A_{sf} vs. h_f/h_{max} relation in our results with those from Ref.[91], as shown in Fig. 5.7 (see section 2.8.3 for parameter definition). It is clear that our data points fall between the "no work hardening" and "linear work hardening' regions, and was in the pileup regime. Considering the moderate work hardening capacity of the investigated FeCr alloys (which generally decreases with increasing alloy strength due to Cr addition or aging), the good match of our results with the simulation work qualitatively explains why all the investigated materials exhibited significant pileups as shown in Fig. 4.9.

Both direct measurement and indirect estimation of the actual contact area were conducted in the past decades to account for the pileup effect [92–95]. In the current study, quantification of the actual contact area was based on measurement of the peak pileup height along each side of the indent, with the total pileup area fitted to a sinusoidal curve.

Fig. 5.8a compares the bulk hardness extracted from Vickers tests using 1 kgf load and bulk equivalent hardness obtained from Nix-Gao analysis of the nanoindentation data using a constant strain rate of 0.05 /s. The plot of Vickers hardness vs. nanoindentation bulk equivalent hardness falls almost on a straight line for each set of data points regardless of data processing. The uncorrected data is well below the ideal correlation line (i.e., nanoindentation hardness H_0 values without pileup corrections consistently overpredict the actual bulk hardness), while the pileup corrected bulk equivalent hardness is generally close to the Vickers hardness although

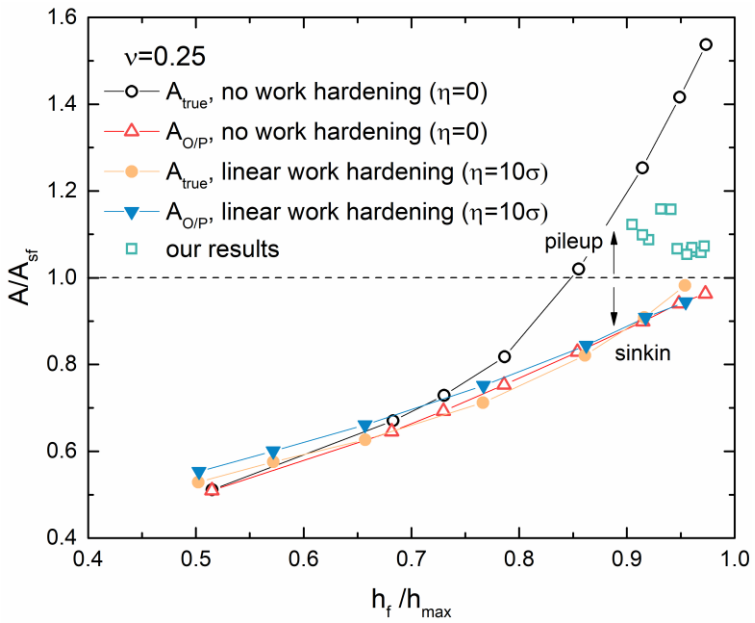

Fig. 5.7 The dependence of A/A_{sf} on h_f/h_{max}. Our results are included as open green squares. Reproduced from Ref. [91].

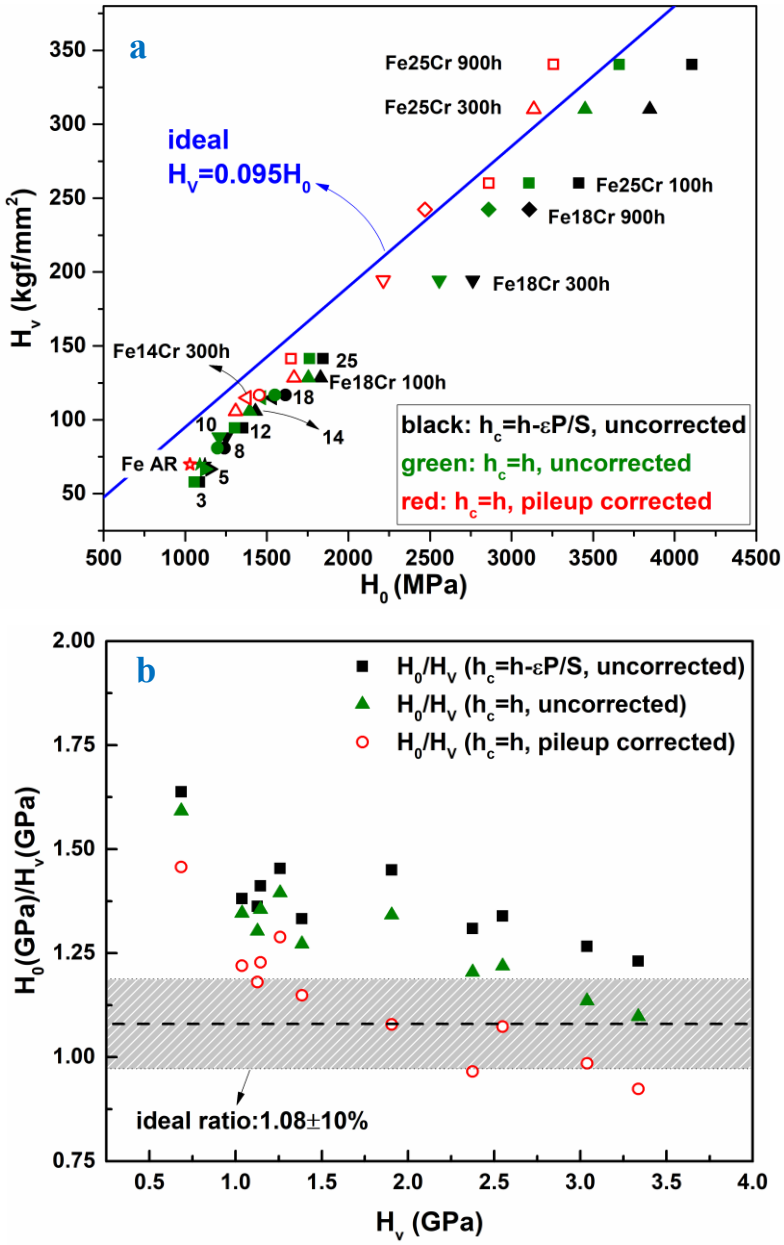

Fig. 5.8 (a) The relation of Vickers hardness and bulk equivalent hardness measured by nanoindentation. The solid symbols refer to the pileup-uncorrected values, and the open symbols to the pileup-corrected values. The ideal correlation line is plotted as a reference. All the as-received Fe-Cr alloys are identified with numbers corresponding to the Cr concentration (wt.%). (b) The ratio of Vickers hardness and bulk equivalent hardness. The shaded horizontal region depicts ±10% variation from the ideal relationship between H_0 and H_V.

there is a relative larger deviation for as-received Fe. Fig. 5.8b compares the ratio of H_0 vs. H_V for each material. The progressive improvement in agreement between H_V and H_0 can be seen for the Nix-Gao data after replacing the contact depth with total depth and including pileup corrections. Therefore, nanoindentation using the appropriate contact depth relationship (Eq. 2.4 vs. $h_c = h$) combined with pileup corrections provides a quantitatively accurate way to predict the bulk Vickers hardness in nano scale test volumes. The moderate overprediction of the nanoindentation bulk equivalent hardness for the softer materials (H_V < ~1.25GPa) even after pileup correction in Fig. 5.8b indicates that an additional physical phenomenon is affecting the measured nanoindentation hardness. This might be due to the actual dislocation density being less than the geometrically necessary dislocation density assumed in the Nix-Gao model [88,89], or another unidentified mechanism.

5.1.5. Correlation of microstructure and mechanical properties

In order to predict yield or ultimate tensile strength, numerous studies have noted that $H_V \sim 3\sigma_y$ [6,149]. It should be noted that the correlation factor of 3 between Vickers hardness and yield strength can be only rigorously applied for ideal plastic materials and fully work-hardened materials. For many typical metals with significant work-hardening capacity, the Vickers indentation process corresponds to a flow stress achieved after a strain of about 8%. Therefore, Vickers hardness for real metals without pre deformation is better correlated to three times the flow stress at ~8% strain rather than the yield stress, i.e., $H_V = 3\sigma_{8\%}$ (both in units of MPa) [6,149]. Based on empirical correlations between Vickers hardness and yield strength, for BCC ferritic steels we will assume $\Delta\sigma_y = 3\Delta H_V$ with units of MPa for $\Delta\sigma_y$ and kgf/mm^2 for ΔH_V [150,151]. Combining with the ideal factor 0.095 between H_V and pileup-corrected H_0, a prediction of yield strength change can be made from the change of bulk equivalent hardness as described in the equation below,

$$\Delta\sigma_y^{NI} = 0.285\Delta H_0 \tag{5.5}$$

where $\Delta\sigma_y^{NI}$ and ΔH_0 are both in units of MPa, and the superscript 'NI' refers to nanoindentation.

On the other hand, prediction of yield strength change by characterizing microstructures, i.e., model prediction, has also been widely studied [9,25,152–154]. In the current research, high purity Fe and FeCr samples with extremely large grain size were used for investigations. Comparing the hardness of as-received Fe, Fe18Cr and Fe25Cr samples, the differences mainly originate from solid solution hardening due to the alloyed element chromium. During thermal

aging of the FeCr alloys at 475 ℃ for 100-900 hours, the chromium atoms in the matrix nucleate a high density of nanoscale Cr-rich α' precipitates, as quantified by atom probe tomography. These precipitates are obstacles to the movement of dislocations, which increases the hardness of the thermally aged FeCr alloys. The formation of α' precipitates also reduces the chromium content in the matrix of the aged samples, thereby decreasing the solid solution hardening contribution compared to the corresponding as-received samples. Therefore, both solution hardening and precipitation strengthening effects need to be accounted for in model predictions of yield strength change of the aged FeCr alloys.

Several models have been proposed to account for the solute hardening effect by quantifying the relationship between the change of yield strength and solute concentration. A power law equation is widely used to describe the solution hardening as $\Delta\sigma_{ss} = Bc^n$, where B is a constant related to the material properties and c is the solute content. The exponent n varies depending on the solute concentration from 1/2 for low solute content, 1 for the intermediate concentration and 2/3 for high solute content [155–157]. In the current research, the measured change of Vickers hardness with Cr content for Fe 3-25 wt.% Cr alloys is shown in Fig. 5.9. Compared with pure iron, the lower hardness of FeCr alloys with chromium content below ~5 wt.% is reasonably considered as solution softening which routinely occurs in dilute FeCr alloys at and below room temperature [158,159]. A linear variation of the Vickers hardness as a function of Cr concentration is observed for FeCr alloys near 3-10 wt.%Cr, which agrees with the trend found by prior research at similar intermediate FeCr alloy concentrations [156,160]. For higher Cr content (>10 wt.%), we found both linear and 2/3 power fitting provide good correlation between the change of Vickers hardness and Cr concentration. Here, the 2/3 power fitting is shown in Fig. 5.9. Therefore, the solution hardening $\Delta\sigma_{ss}$ relative to pure Fe can be related to Cr content as $\Delta\sigma_{ss}=3(13.57c^{2/3}-44.92)$ for the as-received and aged Fe18-25Cr, where the matrix Cr content is shown in Table 3.1 (section 3.6).

To quantify the effect of dispersoid size and density on precipitation strengthening, two hardening models have been proposed based on the obstacle resistance to shearing or bypassing by gliding dislocations [161]. For strong obstacles, the dispersed barrier hardening (DBH) model developed by Seeger et al. [162] is most appropriate and is described by the equation below:

$$\Delta\sigma = \alpha M \mu b \sqrt{Nd} \tag{5.6}$$

where $\Delta\sigma$ is the change in yield strength, M is the Taylor factor (3.06 for equiaxed BCC polycrystalline metals), α is the obstacle strength factor (0.25-1 for strong obstacles [161]), μ

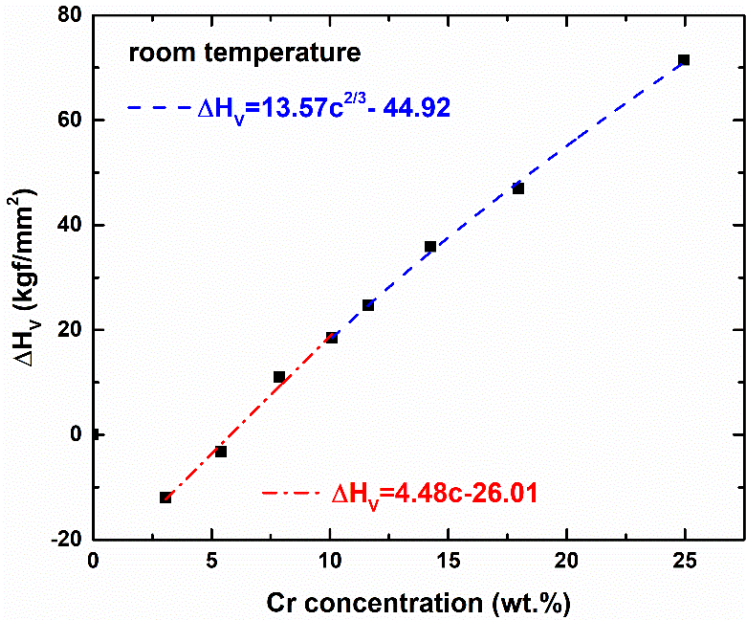

Fig. 5.9 Change of Vickers hardness as a function of Cr concentration for as-received FeCr alloys.

is shear modulus, *b* is the magnitude of the Burgers vector of the glide dislocations interacting with barrier obstacles (a/2<111> in current study where a=0.248 nm), *d* is the defect diameter and *N* is the defect number density. Conversely, the Friedel–Kroupa–Hirsch (FKH) model [163,164] is generally considered more relevant to describe the hardening behavior due to interaction of dislocations with weak obstacles [152]:

$$\Delta\sigma = \gamma M \mu b d N^{\frac{2}{3}} \tag{5.7}$$

where γ is the obstacle strength factor with typical estimated values of 0.05-0.2 for vacancy loops and voids [163,164].

Both solution hardening and precipitation strengthening contribute to the change of the hardness of the aged samples in this study. To quantify the combined effect of these two strengthening mechanisms, an appropriate superposition method should be adopted. Linear and root-sum-square (RSS) superpositions are two methods usually used to evaluate strengthening contributions due to different barriers. Generally, linear superposition is a bounding limit for obstacles with very different strengths, while obstacles with similar strengths (similar dislocation bowing) can be added in root sum square [154,165,166] as below,

$$\Delta\sigma_y^{\text{model}} = \sqrt{\Delta\sigma_{ss}^2 + \Delta\sigma_{\alpha'}^2} \tag{5.8}$$

where $\Delta\sigma_{\alpha'}$ is the $\Delta\sigma$ associated with the Cr-rich precipitates in the DBH or FKH model. In the current study, both DBH and FKH models, as well as linear and RSS superposition methods for the solid solution and precipitate strengthening components, were evaluated to examine the predictive accuracy of the models.

The strength factors in this study were calculated according to equations below [167],

$$\alpha = \frac{0.816\gamma_{cp}d}{\mu b^2\left(1-0.816d\sqrt{Nd}\right)} + 1.7\left(\frac{d}{b}\right)^{1.5}\varepsilon^{1.5} + 0.0044\left(\frac{d}{b}\right)^{1.275}\left(\frac{\Delta\mu}{\mu}\right)^{1.5} \tag{5.9}$$

$$\gamma = \frac{0.816\gamma_{cp}d}{\mu b^2} + 1.7\left(\frac{\varepsilon}{b}\right)^{1.5}\frac{d}{N^{1/6}} + 0.0044\left(\frac{\Delta\mu}{\mu}\right)^{1.5}\frac{d^{0.775}}{b^{1.275}N^{1/6}} \tag{5.10}$$

where μ is the shear modulus of the matrix, Δμ is the shear modulus mismatch due to the addition of Cr in Fe, b is the glide dislocation Burgers vector (0.247nm), d and N are the precipitate diameter and number density, respectively, and γ_{cp} and ε(≈2/3Δa/a) are the interfacial energy and lattice parameter mismatch of the matrix and the precipitates. Eq. 5.10 was modified from Eq. 5.9 by using a different inter-obstacle spacing definition, $\lambda=d^{-1}N^{-2/3}$ [167]. In this study, Δμ, γ_{cp} and ε were estimated from pure bcc iron and bcc chromium as 33 GPa [168], 0.01 J/m^2 [169], and 0.0046 [170–174] at the room temperature.

Fig. 5.10 shows the calculated strength factors for the aged Fe18Cr and Fe25Cr samples. A nearly linear relationship was observed between the strength factor and the α' precipitate diameters. Table 5.1 lists the yield change calculated from DBH and FKD models using the corresponding strength factors. In aged Fe25Cr samples, the hardening contributions from spherical and non-spherical precipitates were superposed by root-sum-square method, and Table 5.1 only presents the resultant values.

Fig. 5.11 compares the predicted change of yield strength from the DBH and FKH models (Eqs. 5.6, 5.7) with the yield strength derived from nanoindentation tests (H_0 values corrected for pileup effects and converted to yield strength using Eq. 5.5) for as-received and aged samples. The detailed numerical values are summarized in Table 5.1. In our study, the barrier strength factors, i.e., α and γ, were assumed to be dependent on the size of the α' precipitates, and were calculated according to Ref. [167] (see Eq. 5.9, 5.10 and Fig. 5.10 and Table 5.1 for details). For the DBH model, the calculated barrier strengths for coherent precipitates are α ~0.04-0.08 for d<5 nm, which are close to the best fit empirical values from previous studies for nanoscale α' precipitates in Fe-Cr alloys (values ranging from 0.04 to 0.06) [25,175]. For larger α' precipitates, the calculated barrier strength factor increases up to α ~0.2 for d=7 nm. In the FKH model, the γ factors increase from 0.07 to 0.24 for obstacle size in the range of 2-7nm, which are comparable to the simple estimates of 0.05-0.2 derived in Ref. [163,164]. With those calculated strength factors, both the DBH and FKH models with root-sum-square superpositions provided very good agreement with the bulk equivalent hardening measured by nanoindentation as shown in Fig. 5.11b. Conversely, the linear superposition for quantifying total hardening overestimated the hardening contributions from the microstructures, particularly for the precipitate-containing materials.

The good agreement for the solid solution + precipitation model predicted strength changes with the nanoindentation results offers promise for the prospect of using nanoindentation tests to predict the bulk mechanical properties in nano scale volumes with acceptable quantitative accuracy. This good quantitative accuracy required application of indentation pileup corrections and size-dependent adjustments of the precipitate hardening coefficients. Ultimately, additional studies over a wide range of alloys are needed to evaluate the most appropriate hardening model (DBH vs FKH) and superposition method.

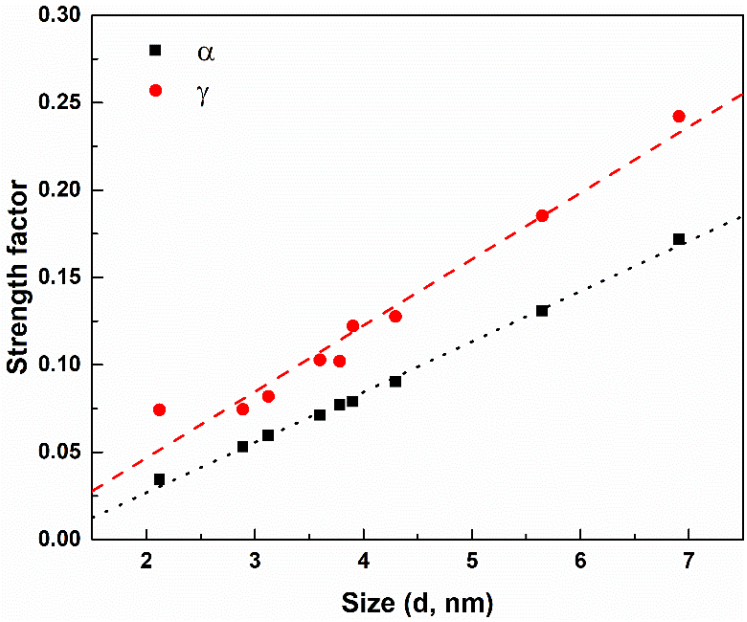

Fig. 5.10 Calculated strength factors vs. diameter of α' precipitates in Fe18Cr and Fe25Cr thermally aged at 475 ℃ for 100-900 hours. The strength factors for the non-spherical precipitates in Fe25Cr samples were also included.

Table 5.1 Yield strength changes (MPa) due to solid solution hardening and model-predicted precipitate strengthening contributions, along with the measured nanoindentation strengthening relative to pure Fe.

Materials	$\Delta\sigma_{ss}$	DBH	RSS	Linear	FKH	RSS	Linear	$\Delta\sigma_y^{NI}$
Fe18Cr AR	145	-	145	145	-	145	145	121
Fe18Cr 100h	142	83	165	225	77	161	219	182
Fe18Cr 300h	109	363	379	472	342	359	451	338
Fe18Cr 900h	88	445	454	533	419	429	507	410
Fe25Cr AR	213	-	213	213	-	213	213	177
Fe25Cr 100h	147	460	482	607	435	459	582	522
Fe25Cr 300h	110	567	577	677	540	551	650	600
Fe25Cr 900h	90	641	647	731	612	618	702	635

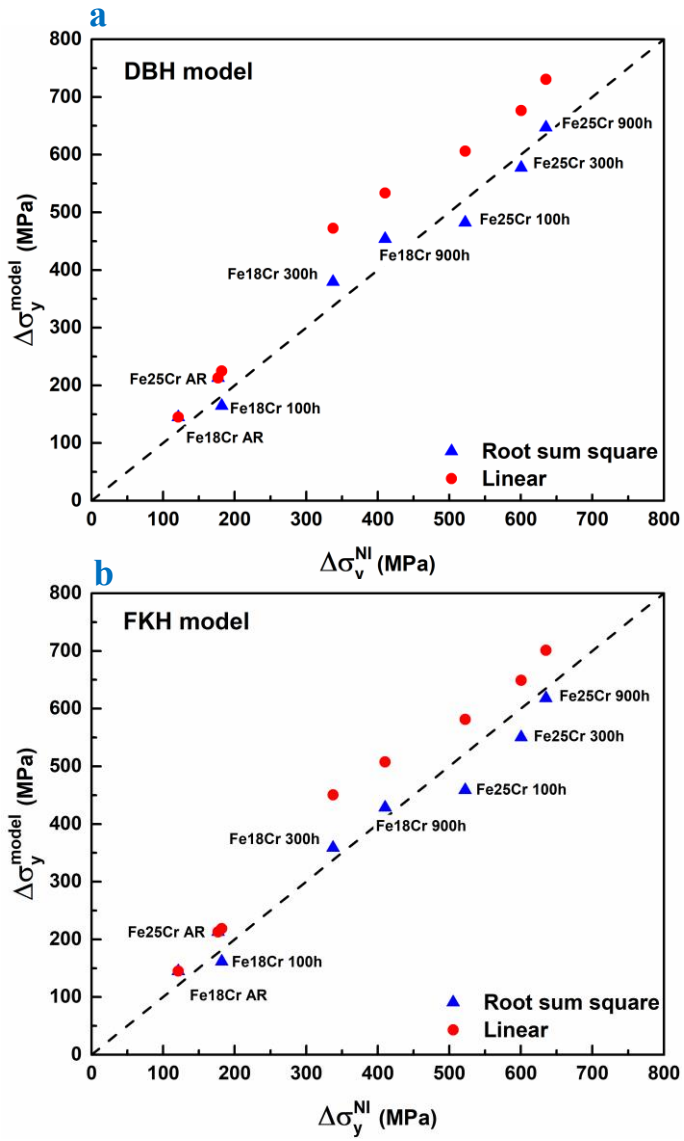

Fig. 5.11 Correlation of nanoindentation ($\Delta\sigma_y^{NI}$) and microstructural model prediction ($\Delta\sigma_y^{model}$) of yield stress change assuming linear and root sum square superposition of solution hardening and precipitate strengthening for (a) DBH model and (b) FKH model. The dashed line is the ideal correlation ratio of 1.

5.2. Microstructure evolution and mechanical properties of ion irradiated Fe18Cr

In section 5.1, the nanoindentation test protocol has been demonstrated to work well on the thermally aged FeCr binary alloys. The accurately extracted nanoindentation bulk equivalent hardness resulted in a good correlation with Vickers hardness, as well as a great agreement between model predicted yield strength and nanoindentation converted yield strength. In this section, the developed test method was applied to ion irradiated Fe18Cr alloys under different temperatures, doses, and dose rates. The effect of irradiation on the microstructures and mechanical properties was discussed, and a refined method was suggested for the model-predicted strength.

5.2.1. Temperature effect on microstructures

In the current study, a large amount of black dot defect clusters was found forming either in the matrix or around the dislocation lines at all temperature conditions, while larger dislocation loops were only observed at 450 °C. To clarify these features from possible FIB damages, STEM images from the interface of irradiated and unirradiated regions were taken at different zones, as shown in Fig. 5.12. The depth of 1800 nm is corresponding to the peak damage position. It is clear that within the irradiated region < 1800 – 2000 nm, both samples exhibit apparent black dots. However, both the matrix and the dislocation lines are almost free of any dot features outside the damage region. The results in Fig. 5.12 demonstrate that the electropolishing on the FIB lamellas used in this study effectively removed the FIB damages on the samples, and the black dots were predominantly induced by ion irradiation.

At 300 and 350 °C, the dislocations decorating with the irradiation-induced black dots are the most impressive microstructural modifications. A similar decoration phenomenon was also reported for neutron irradiated alpha-iron at reactor ambient temperature (80 °C) [176] and 300 °C [177]. One possible reason for the decoration is related to the strain field around the dislocations, which can trap the irradiation induced point defects and finally promote the formation of small defect clusters [178]. Besides, if a Cottrell atmosphere exists on the dislocations, the strain field can be enhanced, and more interstitials will be accumulated for the formation of small clusters such as black dots. These black dots can be the precursor of large dislocation loops, which was evident on the 10^{-4} dpa/s irradiated samples from 300 °C to 450 °C with the dislocation loops being formed on the dislocation lines.

For the black dots in the matrix, Field et al. assumed that they are either 1/2<111> or <100> loops in neutron irradiated FeCrAl alloys at 382 °C [25], in order to quantify their hardening

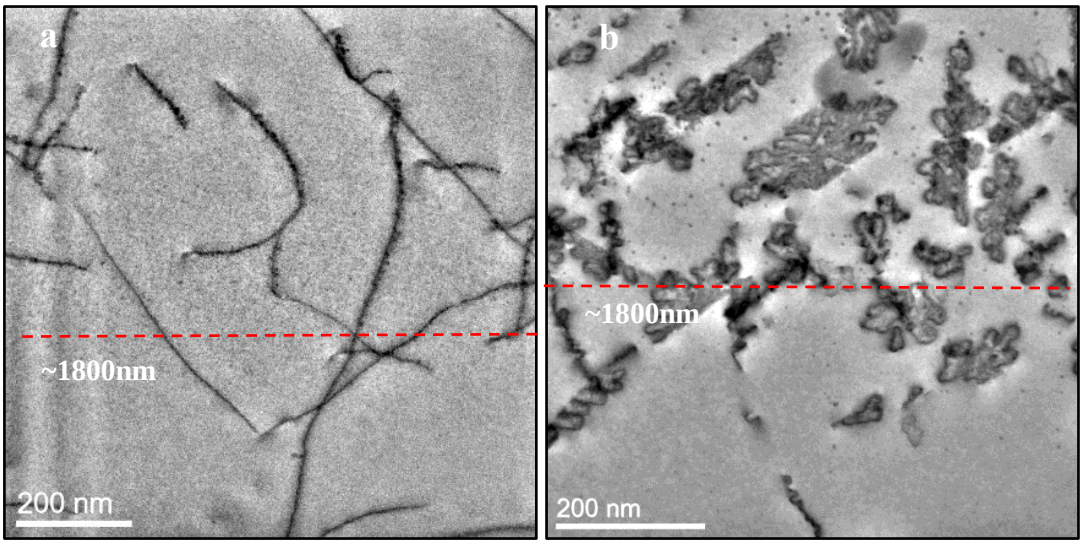

Fig. 5.12 STEM images showing the black dots in the irradiated region. (a) 350 ℃, 0.35 dpa, 10^{-4} dpa/s, [100] zone. (b) 450 ℃, 0.35 dpa, 10^{-5} dpa/s, [111] zone. The sample surface is parallel to the red dashed line.

effect. Yao et al. investigated the in-situ irradiation on Fe18Cr alloys using 100 keV Fe^+ ions at room temperature, and also observed the formation of black dots. By performing careful TEM characterizations with g·b criteria, they concluded that the black dots are small dislocation loops and identified them as the 1/2<111> and <100> loops [179]. It may be reasonable to infer

that the black dots in the matrix in this study also consist of these two types of dislocation loops. In the current study, the black dots were only observed at lower temperatures, either in the matrix or on the dislocation lines. Horton et al. reported only edge-on <100> loops at elevated temperatures for the neutron irradiated Fe and ferritic steels, which is similar with our results at 450 °C [178]. The loop type transformation from 1/2<111> to <100> may occur with the increasing temperatures, resulting in the absence of 1/2<111> loops. In an in-situ irradiation investigation on tungsten, Li et al. observed the nucleation, movement and growth of the black dots in the bcc crystal [180]. In their study, the interactions of two 1/2<111> loops were considered as the formation mechanism of <100> loops at elevated temperature. Such a mechanism was also proposed for FeCr alloys [29,181].

Overall, the black dots formed in the ion irradiated Fe18Cr alloys consist of both 1/2<111> and <100> loops at 300 and 350 °C. With the increase of irradiation temperature, the growth and interaction between the small dots occurred and eventually large <100> loops were formed. A detailed TEM characterization is needed to confirm the type of black dots in the future work.

5.2.2. Dose rate and dose effect on microstructures

For 0.37 dpa irradiation, the evolution trend of black dots and dislocations with dose rate is related with each other. At 300 °C, black dots appear at intermediate dose rate (10^{-4} dpa/s), indicating a threshold dose rate is needed for the nucleation of these small clusters [182]. The black dots density increases while the size decreases with increasing dose rate at 350 °C due to more point defects produced at higher dose rate (Fig. 4.14). At 450 °C, both density and size of the black dots decrease with increasing dose rate (Fig. 4.14). Considering the existence of dislocation loops at this temperature and the increasing loop size with dose rate (Fig. 4.13), it is reasonable to state that the black dots were agglomerated to form the dislocation loops. The comparable dislocation loop density regardless of dose rate and larger loop size for lower dose rate at 450 °C, are consistent with the literature [29]. Schaublin et al. found that the number density of loops in pure iron after irradiation with 500 keV Fe^+ did not depend on the dose rate (5.5×10^{-4} and 5.5×10^{-5} dpa/s), while the sizes of the loops were larger under lower dose rate.

Such a trend of decreasing loop size with increasing dose rate was also observed in another bcc system, i.e., tungsten [183]. Li et al. reported a consistent vacancy loop density with dose rate and a larger loop size at lower dose rate on Fe-C alloys at dose larger than 0.3 dpa [184]. They attributed this evolution to the vacancy jump events which were promoted at lower dose rate; thus the vacancies can aggregate to larger clusters.

Even at higher dose of 3.7 dpa, irradiation at 350 °C induced black dots but no dislocation loops, indicating that temperature is a more significant factor than dose for the formation of dislocation loops. Higher dose induced higher concentration of point defects [23], which favored the formation of black dots and resulted in a higher density at 350 °C under 3.7 dpa, as shown in Fig. 4.16b. Ding et al. proposed that the interstitial cluster could absorb the interstitials and evolve to dislocation loops at higher doses [183]. Although we did not identify the loop type in this study, it can be generally inferred that the dislocation loops were also formed by coalescence of black dots (either interstitial or vacancy type). Indeed, the experimental results shows that pronounced transformation of black dots to dislocation loops likely happened under 3.7 dpa, leading to a lower black dot density and higher dislocation loop density compared with 0.37 dpa. This transformation depends on irradiation temperature and is affected by dose as well as dose rate. The comparable size of black dots at both doses is reasonable, since the larger dots can be imaged using STEM and be categorized as dislocation loops.

5.2.3. Correlation of microstructure with mechanical properties

As mentioned in section 5.1.2, elastic modulus is an important criterion to evaluate the reliability of nanoindentation measured bulk equivalent hardness. For the ion irradiated Fe18Cr alloys in this study, the modulus evolution with indentation depth is shown in Fig. 5.13. It is clear that the moduli are almost constant as indentation depth increases from 100 nm to 1000 nm, indicating the good accuracy of the measured nanoindentation hardness. For better understanding the strengthening contribution from the microstructures, the strength predicted from the classic hardening model was compared with the measured strength. The measured strengths were calculated based on nanoindentation measured bulk equivalent hardness and using $\sigma = 0.285\ H_0$, as described in section 5.1.5. In Chapter 4, dislocation lines, dislocation loops, black dots and α' precipitates were observed in the Fe ion irradiated Fe18Cr alloys under

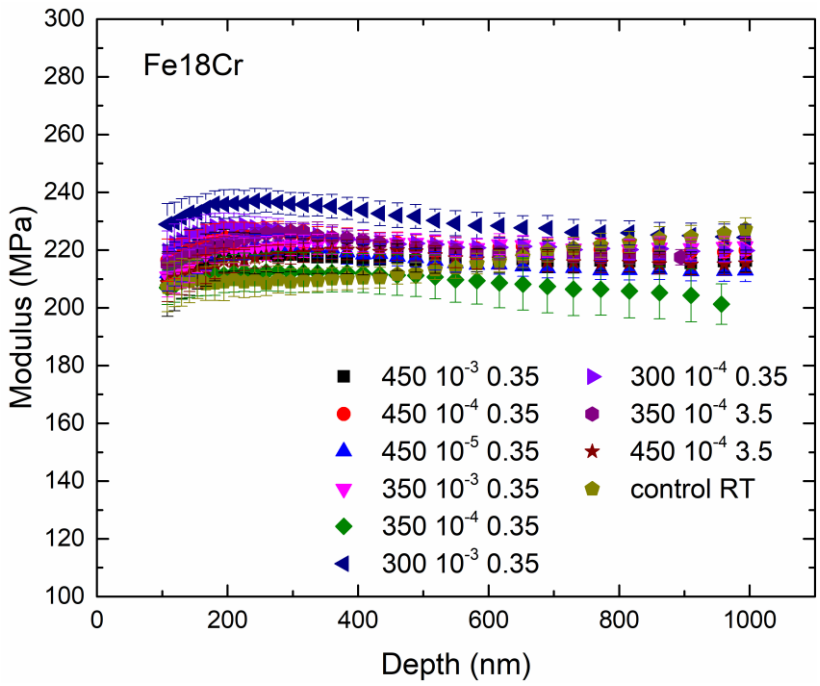

Fig. 5.13 The modulus evolution with indentation depth for ion irradiated Fe18Cr. The units of the legend are ℃, dpa/s and dpa, respectively.

different doses, doses rates and temperatures. In this Chapter, we will consider the hardening components from these features, as well as the solution hardening.

Before and after treatment, such as thermal aging and irradiation, the change of yield strength is caused by the change of microstructures. Therefore, an intuitive method to conduct the correlation is to compare the measured yield change $\Delta\sigma_y^{measured}$ with the model predicted yield change $\Delta\sigma_y^{model}$ from irradiation-induced microstructures. In this method, $\Delta\sigma_y^{model}$ is associated with yield strength before and after irradiation as given in the equation below:

$$\sigma_y^{irr} = \sigma_y^{unirr} + \Delta\sigma_y^{model} \tag{5.11}$$

where σ_y^{irr} and σ_y^{unirr} are the model predicted yield strengths by accounting for the microstructures before and after irradiation, respectively.

One issue in Eq. 5.11 is the superposition method used to combine all the hardening components. From section 5.1.5, the hardening obstacle with similar strengths should be added by root sum square method, while for quite different strengths a linear supposition should be used [165,185]. Generally, we separate the obstacles into weak (α<0.25) and strong (α>0.25) groups. For each of the weak and strong groups, root sum square is used, followed by linear supposition to combine the strength from composite weak and strong obstacles together, as shown in Eq. 5.12.

$$\sigma_y = \sqrt{\sum \sigma_{weak}^2} + \sqrt{\sum \sigma_{strong}^2} \tag{5.12}$$

where σ_{weak} and σ_{strong} refer to the each of he weak and strong obstacle, respectively. In Eq. 5.11, σ_y^{unirr} may contain both weak (solute solution, lattice friction stress, etc.) and strong (grain boundary, dislocation lines, etc.) obstacles, as does the $\Delta\sigma_y^{model}$. Therefore, a simple linear superposition on σ_y^{unirr} and $\Delta\sigma_y^{model}$ may cause errors in the combination of the microstructure contribution in line with Eq. 5.12. It is imperative to distinguish the obstacles for accurate accounting of the strengthening from the microstructures. For the ion irradiated Fe18Cr in this study, we considered strengths from base metal strength (pure Fe), solute hardening, Cr-rich precipitates, dislocation lines, dislocation loops, and black dots.

Since the strengthening for Fe18Cr is based on pure iron, the yield strength of large-grained pure iron is included as $\sigma_{Fe} \approx 50$ MPa [186]. The primary solute element in Fe18Cr materials is chromium. In our prior study, an empirical relation between yield strength change with Cr content was established as $\sigma_{ss}=3(13.57c^{2/3}-44.92)$, where c is the Cr content in the matrix in unit of wt.% [124]. For the Cr-rich α' precipitates quantified by APT, since the DBH model used in section 5.1.5 worked well on thermally aged FeCr alloys, it was also applied to calculate

the strengthening $\sigma_{\alpha'}$ on the ion irradiated Fe18Cr alloys. The strength factor α was calculated according to Eq. 5.9, which varied for each irradiation condition due to different density and size of the precipitates. For simplicity, DBH model was also used to account for the strengthening contribution from other microstructures. The dislocation line strengthening was calculated according to $\Delta\sigma_{line} = M\alpha\mu b\sqrt{\rho}$ [187], where ρ is the density of dislocation lines (m^{-2}). α = 0.56 was selected according to Ref. [47].

The dislocation loops (σ_{loop}) and black dots (σ_{dot}) are similar to a thin-plate shape. Therefore, the strength factor was calculated with the following equation [167,188]:

$$\alpha = \frac{0.271A}{(1-\nu)^{\frac{1}{2}}\sqrt{ND}(16-\pi tA)} \ln\left(\frac{0.637D}{r_0}\right) \quad (5.13)$$

where N is number density, D is the diameter of the dislocation loop, r_0 is the radius of dislocation core, and t is the thin plate thickness, which depends on the type of loops. In a bcc structure, t=0.287nm and 0.166 nm for <100> and 1/2<111> loops, respectively. A is a simplified parameter described as below:

$$A = \sqrt{16\pi ND} + 4ND^2 - \pi^2 NDt \quad (5.14)$$

For dislocation loops and black dots, r_0 = 1.77b was used in our study [167].

The calculated strength factors are listed in Table 5.2. The Cr-rich α' precipitates are weak obstacles with strength factor less than 0.1, while for the dislocation lines and dislocation loops, α is much larger than 0.5. For dislocation lines, since the literature strength factors were estimated by fitting the model predicted strength and tensile measured strength, it is not possible to have an accurate science-based independent estimate of their strength factor. A strength factor of α=0.33 for dislocation lines has been used for ODS FeCr alloys in the previous studies [189–192]. Porollo et al. reported α=0.64 for dislocation lines in neutron irradiated FeCr alloys [193]. In the current study, α=0.56 was used based on the similar microstructures (α' precipitates, dislocation loops, dislocation lines) to materials in the literature study [47]. However, it is worth noting that the decoration of black dots on the dislocation lines may produce higher strengthening effect compared with bare dislocations. Further work is needed to clarify the influence of black dots on the strength factor of dislocation lines. The strength factor for dislocation loops was proposed to depend on loop size [194,195]. However, the functions to calculate the factors were not based on rigorous models and generally assumed a monotonic increase with defect size. Dubinko et al. [194] estimated that the loop strength factor for the RPV steel rapidly increases from ~0.1 to ~0.6 as the number of atoms in

Table 5.2 Summary of the size-dependent barrier strength factors used in the DBH model calculations for precipitates, dislocation lines, loops and black dots.

Dose	Dose rate	Temperature	Cr-rich α' precipitates	dislocation lines	dislocation loop	black dots
(dpa)	(dpa/s)	(°C)				
0.37	10^{-3}	300	0.03	0.56		
		350	0.04	0.56		0.20
		450	0.05	0.56	0.59	0.21
	10^{-4}	300	0.03	0.56		0.26
		350	0.04	0.56		0.25
		450	0.05	0.56	0.66	0.22
	10^{-5}	450	0.06	0.56	0.87	0.23
3.70	10^{-4}	350	0.04	0.56		0.28
		450	0.08	0.56	0.59	0.27

the loop increases from ~300 to 10^5. Similarly, Hu et al. [195] assumed that small loops have a strength factor near zero, while the factor for loops > 6 nm increased to near 1 in Fe. Besides, some other studies obtained the loop strength factors via best fit between the barrier strength hardening model and mechanical testing properties. Varied values for the strength factors were reported, such as ~0.33-0.7 for RPV steels [196] and 1.135 for α-Fe [197]. The loop strength factors in this study were calculated based on the size and number density of the dislocation loops, and considered the physical interactions between the moving dislocations and loops. The only issue for the calculation of dislocation loop strength factor is that Eq. 5.13 was derived on Frank loops which are sensile in the materials. For the glissile 1/2<111> and <100> perfect loops in the bcc materials in this study, we may overestimate the strength factors. And this may be one of the reasons for the slightly higher strength factor for dislocation loops compared with dislocation lines. Therefore, a better estimation of the strengthening component from dislocation loops is needed in the future research. Currently, the assumed dislocation loop strength factor (Eq. 5.13) is the best available expression.

According to the strength factors, the final superposition for the model-predicted yield strength is as follows:

$$\sigma_y = \sqrt{\sigma_{Fe}^2 + \sigma_{ss}^2 + \sigma_{\alpha'}^2 + \sigma_{dot}^2} + \sqrt{\sigma_{line}^2 + \sigma_{loop}^2} \quad (5.15)$$

For black dots with a slightly larger strength factor than 0.25, they were included in strong obstacle category in Eq. 5.15. Table 5.3 summarizes the measured strength, the strengthening contributions from each microstructure, and the final superposed strengths. To compare the contributions of these strengthening components, the percentage of each component in the total strengths is plotted in Fig. 5.14. The total strength is superposed by linear method since the root sum square method is not suitable for the percentage calculation. Although the barrier strength for α' precipitates is small, the strengthening contribution is comparable to or even larger than that from dislocation loops/black dots due to the high α' precipitates number density. The dislocation lines account for over 30% of the total strengths, followed by α' precipitates and dislocation loops (including black dots). For Fe18Cr irradiated at 300 ℃ to 0.37 dpa with 10^{-3} dpa/s, dislocation lines dominate the hardening, while no dislocation line strengthening was observed in the 450 ℃ irradiation at 10^{-5} dpa/s to 0.37 dpa. By using the root sum square superposition for the similar strengths and linear superposition for the different strengths, the model predicted strengths were acquired and compared with the measured strengths, as shown in Fig. 5.15.

Table 5.3 Summary of the measured strength, the strengthening contribution, and the superposed model strengths.

Dose	Dose rate	Temperature	H_0	measured σ_y	pure Fe	solution hardening	Cr-rich α' precipitates	dislocation lines	dislocation loop	black dots	model σ_y
dpa	dpa/s	°C	MPa	MPa	MPa	MPa	MPa	MPa	MPa	MPa	MPa
0.37	10^{-3}	300	3039	866	50	145	36±14	673			831±3
		350	2398	683	50	126±1	211±34	340		66±14	599±28
		450	2935	836	50	128±4	233±21	535	155±23	30±8	829±19
	10^{-4}	300	2937	837	50	130±2	152±21	570		102±14	785±16
		350	2489	709	50	120±4	242±44	341		49±7	619±39
		450	2947	840	50	114±3	323±13	416	199±45	41±5	809±23
	10^{-5}	450	2994	853	50	87±1	437±73		368±58	56±7	820±92
3.70	10^{-4}	350	3051	870	50	107±3	289±26	466		85±20	786±24
		450	2652	756	50	117±2	314±12	341	183±44	30±6	727±24

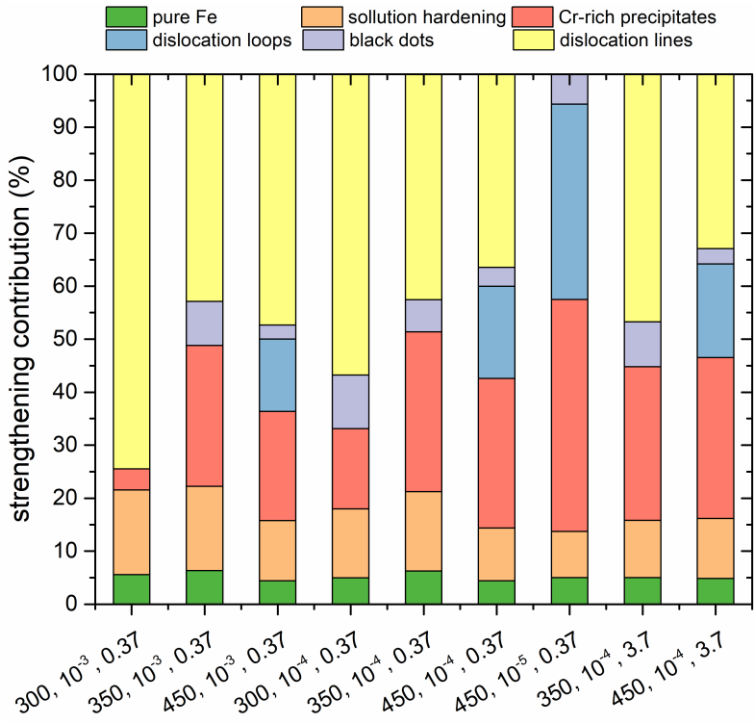

Fig. 5.14 The strengthening contribution from each of the microstructures for the irradiated Fe18Cr alloys. The x axis is labelled according to temperature, dose rate, and dose with units of °C, dpa/s and dpa, respectively.

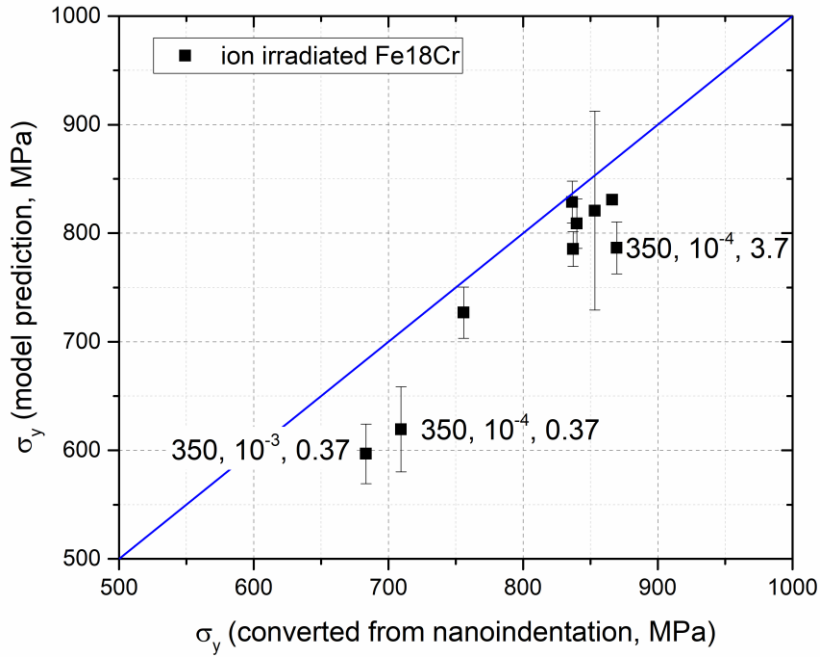

Fig. 5.15 Correlation of model predicted strength with the measured strength. The solid line represents the ideal 1:1 correlation.

Generally, most of the data points fall closely to the 1:1 ideal line, with a minor variation less than 10% except for the data from all 350 ℃ irradiated samples. There are several possible reasons for the underestimation of model predicted strength at 350 ℃: 1) The black dot density may be underestimated, since almost all the black dots were accumulated on the dislocation lines and it is difficult to clearly separate the overlapped features; 2) Due to the significant decoration of black dots on dislocation line, the actual obstacle strength for decorated dislocation lines may be larger than regular dislocation lines; 3) There may exist some unknown features which also contribute to the hardening but were ignored in the characterizations. For the 450 ℃ irradiated sample at 10^{-5} dpa/s to 0.37 dpa, the largest error bar comes from the non-homogeneous distribution of the α' precipitates and dislocation loops. Overall, only the strength factors for dislocation lines were selected from literature fitting of hardening data; the calculated size-dependent strength factors for other features in the current study can improve the estimation of strengthening component from each microstructure element, compared with the traditional approach of artificially adjusting the strength parameters so that a reasonable match is achieved between microstructure-calculated and measured hardening. Meanwhile, the relatively good agreement between model predicted strength and measured strength further demonstrates that the nanoindentation test protocol in this study works well on the ion irradiated samples, and also supports the refined superposition method in this Chapter.

5.3. Insight in ion irradiation as a surrogate of neutron irradiation

We have demonstrated the accuracy of nanoindentation test on the thermally aged FeCr binary alloys and ion irradiated Fe18Cr alloys. Thermal aging produced only Cr-rich precipitates in the alloys, while ion irradiation introduced additional dislocation loops and black dots. In the previous sections, these features were correlated to the mechanical properties by the DBH model. For more complicated microstructures in the dual ion and neutron irradiated commercial alloy T91 and HT9 in this section, a detailed discussion was made to test the hardening model. From the microstructure evolution and strengthening contribution, the fidelity of ion irradiation as a surrogate of neutron irradiation is discussed.

5.3.1. Temperature shift and cavity swelling

The dose rate for ion irradiation is generally several orders of magnitude higher than neutron irradiation. At a fixed temperature, a higher dose rate causes higher radiation induced

point defect concentration, resulting in an increase of point defect recombination and decrease of thermal emission of vacancies. However, increasing the temperature reduces the matrix recombination and increases the thermal emission, due to higher vacancy mobility, which compensates the effect of higher dose rate [198]. Therefore, a higher temperature is generally used for ion irradiation for a comparable swelling with neutron irradiation. One classic temperature shift theory was developed under the recombination dominated steady-state case for two different dose rate irradiations which produce a constant net flux of vacancies over interstitials to voids. The equation is described as [57,198]:

$$T_2 - T_1 = \frac{kT_1^2/(E_v^m+2E_v^f)\ln(G_2/G_1)}{1-kT_1/(E_v^m+2E_v^f)\ln(G_2/G_1)} \quad (5.16)$$

where T_1 and T_2 are irradiation temperatures for dose rate G_1 and G_2, respectively. k is the Boltzmann constant, which is 8.617×10^{-5} eV/K. E_v^m and E_v^f are vacancy migration and formation energy, respectively.

In this study for T91 and HT9 alloys, the ion irradiation dose rate is ~7.5×10^{-4} dpa/s, and the neutron irradiation dose rate is 6-9×10^{-7} dpa/s [109]. Fig. 5.16 shows the swelling of the investigated samples. Neutron irradiation at 376 ℃ produced the largest volumetric swelling, and we will take this temperature as the peak swelling temperature T_1. If setting E_v^m = 0.67 eV, and E_v^f = 2.02 eV [199,200], the theoretical peak swelling temperature shift for T91 is 57-61 ℃. For T91 in Fig. 5.16, ion irradiation at 445 ℃ was shifted slightly higher than theoretical values (69 ℃ vs. 57-61 ℃), with a swelling slightly less than neutron irradiation at 376 ℃. The minor decrease in swelling indicated that the peak swelling temperature for ion irradiation is either lower or higher than 445 ℃. Taller et al. [109] investigated the dual ion (Fe^{2+} and He^{2+}) irradiation on the same heat of T91 alloys as we used, and reported a peak swelling temperature at around 460 ℃ with a relatively smaller swelling of 0.017% than ours at 445 ℃ (0.049%) partially due to ignoring the small cavities (diameter < 2 nm) in their study. Although we did not perform ion irradiation experiments at a higher temperature, it can be inferred that the peak swelling temperature may be about 445 ℃. Therefore, the experimental peak swelling temperature shift is about 69 ℃, which is comparable to the theoretical estimation. Future ion irradiation studies at about 430 ℃ and 460 ℃ is needed to confirm the actual shift.

For neutron irradiation at about 460 ℃, the swelling of T91 and HT9 seems to approach the cessation regime. If we set T_1 = 460 ℃, the estimated cessation swelling temperature shift is 73-78 ℃ under Mansur's model. Experimentally from Fig. 5.16, this shift is about 60 ℃ for T91 and HT9, which is lower than the theoretical values. Lin et al. reported a similar failure of

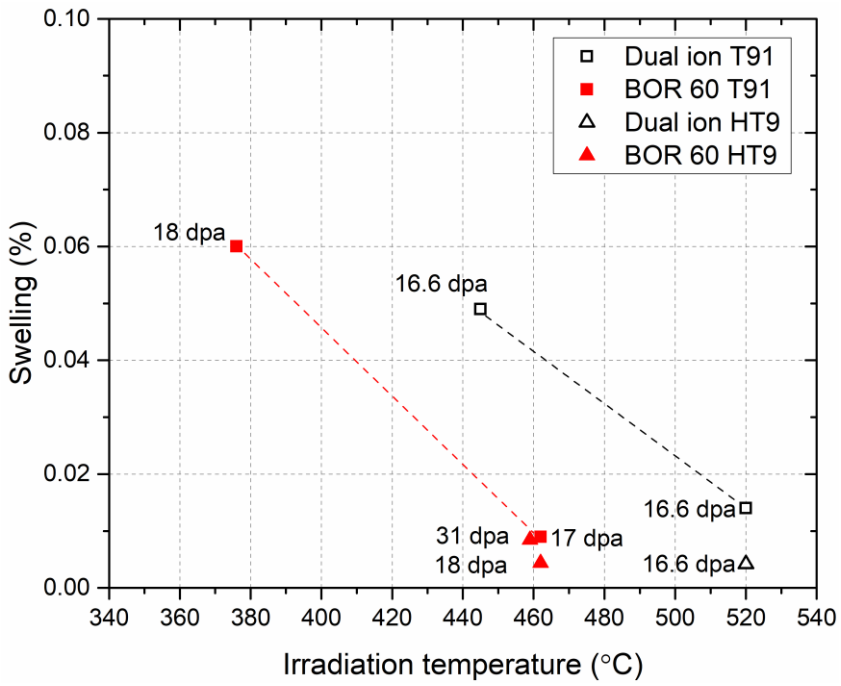

Fig. 5.16 Volume swelling for the dual ion and neutron irradiated T91 and HT9 samples.

Mansur's model in the cessation swelling temperature shift for neutron and ion irradiated Fe9/10Cr binary alloys [201]. To summarize, the Mansur model provided a general match for the peak swelling temperature shift, but there is a larger discrepancy between theoretical and experimental values. A temperature shift around 60 ℃ generally works well for the match of cavity swellings for neutron and ion irradiation.

5.3.2. Dislocations and precipitates: Dual ion vs. Neutron

The 60 ℃ temperature shift between neutron and ion irradiations has been demonstrated to work with the cavity swelling for T91 and HT9 samples in this study, although a failure of Mansur's model occurred for the cessation swelling. For the dislocations, precipitates and radiation induced solute segregation, the comparison between neutron and dual ion irradiation with the same 60 ℃ shift shows comparable results only for dislocation loops for T91, but presents totally different behaviors for the other features, as mentioned in Chapter 4. The neutron irradiation effect on the microstructure evolution of the T91 (376 and 462 ℃) and HT9 (462 ℃) has been reported under similar temperatures and doses.

For F/M steels under neutron irradiation, dislocation loops are typically observed at temperatures less than 400-450 ℃; conversely, only dislocation networks are formed at higher temperatures [202]. Calculation and experiments also show that the <100> type dislocation loops are favorable at elevated irradiation temperatures [202–206]. In this study, both <100> and 1/2<111> type dislocation loops were observed in the BOR 60 reactor irradiated T91samples at 376 ℃, in which the <100> type was dominant. For T91 irradiated at 462 ℃, only dislocation lines and networks were found, which shows the similar trend of dislocation loop evolution with neutron irradiation temperature as reported by others. The dislocation lines and networks may be transformed by dislocation loops at elevated temperatures or the pre-existing features. Jiao et al. studied the dislocation evolution of T91 under the similar irradiation conditions as ours and found that <100> loops were dominant in the temperature regime of 376-415 ℃ [107]. For the dual ion irradiated T91:445℃:16.6 dpa sample, pronounced <100> loops were also observed, with a number density comparable to the 376 ℃ neutron irradiated sample. As shown in Fig. 4.22, the consistent number densities and loop size between neutron and dual ion irradiation support the 60 ℃ temperature shift to account for dose rate differences, which is similar to the study by Taller et al. [109]. At a higher temperature of 520 ℃, ion irradiated T91 is free of dislocation loops in the present study, due to formation of dislocation lines/networks from interactions between the dislocation loops [207].

Although T91 shows a good agreement of dislocation evolution between neutron and dual ion irradiation, HT9 alloys exhibit a different characteristic. Similar with dual ion irradiated T91:445℃:16.6 dpa, the HT9 sample at the same temperature created dominant <100> dislocation loops under 72 dpa. However, contrary to T91, HT9 under ion irradiation at 520 ℃ induced very low density (< 10^{21} m^{-3}) of both <100> and 1/2<111> loops. The <100> loops accounted for 57% of the total characterized loops, which is lower than the 72% reported by Zheng et al. [36] even at a lower temperature (470 ℃). Considering the low loop density in this study and in the reference, one reason for the discrepancy of <100> loop ratio may be the statistic error in quantifying the numbers of dislocation loops. Another possible cause is the uncertainty in determining loop type by shape under [110] zone axis in the present study. A detailed TEM characterization under multiple g vectors is needed in the future work. By shifting the dual ion irradiation temperature of about 60 ℃, the neutron irradiated HT9 at ~460℃ did not exhibit any dislocation loops due to the higher temperature, similar to prior studies [32]. The comparison of dislocation loops in HT9 indicates that thermal annealing, associated with long term exposure of neutron irradiation due to low dose rate, is likely to promote the interaction between the dislocation loops [206]. Consequently, neutron irradiation at ~460 ℃ annealed all the dislocation loops and only network/line dislocations were observed. Overall, the temperature shift of ~60 ℃ didn't work well on the dislocations for HT9 alloys at the investigated irradiation temperatures.

For the investigated T91 (9% Cr) and HT9 (12% Cr) samples subject to neutron irradiation at 376 (T91), 459 (HT9) and 462 (T91, HT9) ℃, as well as ion irradiation at 445 and 520 ℃ (T91, HT9), Cr-rich α' precipitates were not considered since the alloy chromium content is below or on the boundary of the Cr solubility limit in α-Fe for the temperatures in this study [123,208]. The absence of α' precipitates on HT9 has also been confirmed by neutron irradiation at 457 ℃ [32] and heavy ion irradiation at 420-470 ℃ [24], as well as proton irradiation [209]. For T91 in the current study, Ni-rich clusters (including Ni/Si/Mn-rich precipitates) were only observed after neutron irradiation at 376 ℃. At 462 ℃, the temperature appears too high to support the net flux of defects needed to form precipitates, which is also the case for dual ion irradiation at 520 ℃. In contrast, the thermal emission is promoted at this temperature level and an absence of Ni-rich clusters occurred [107]. Under dual ion irradiation at 445 ℃, Ni-cluster was not observed in this study. At the similar condition, T91 was reported to exhibit a very low density (~10^{20} m^{-3}) of Ni-clusters which were considered as the precursors of G phases [109]. The difference between our results and the literature results may come from

the heterogeneous distribution of the possible Ni-clusters. Besides, at an ion irradiation temperature of 445 ℃, the precipitation could be at an initial stage with an extremely low density and small size, making observation difficult. Comparing neutron irradiation at 376 ℃ and dual ion irradiation at 445 ℃, the dose rate discrepancy seems to be responsible for the present and absence of Ni-clusters. It is known that radiation induced precipitation is associated with radiation induced segregation (RIS) which occurs when sufficient flux of defects to sinks are provided [23]. Taller et al. reported an increase of recombination and decrease of point defect to sinks with increasing damage rate at a fixed temperature (445 ℃) [210]. Consequently, Ni-cluster formation is reduced for ion irradiation compared to neutron irradiation.

Compared with T91, dual ion irradiation induced (Ni, Si, Mn)-clusters in HT9 at 445 ℃ after 72 dpa, possibly due to a large amount of point defects and fluxes to sinks at higher doses [23] and slightly higher Ni content than T91 (0.51 wt.% vs. 0.09 wt.%). For neutron irradiation at 462 ℃, HT9 shows comparable (Ni, Si, Mn)-cluster density and sizes with the literature results [32]. Besides, the similar quantitative data shown in Table 4.15 for 459℃:31dpa and 462℃:17 dpa indicates a minor dependence of precipitation on dose. Although it was stated that the G-phase density decreased and size increased for neutron irradiated HT9 at 377 ℃ to 17.1 and 35.1 dpa [31], the statistical values had only minor differences and showed a weak dose effect. This can support the mentioned minor dose dependence in our results even though the neutron irradiation temperatures were different. Overall, the comparison of precipitates between neutron and dual ion irradiation did not support the 60 ℃ shift for T91 and HT9.

5.3.3. Temperature dependence of mechanical properties

The nanoindentation measured elastic modulus vs. depth of ion and neutron irradiated T91 and HT9 alloys are shown in Fig. 5.17. The constant modulus with indentation depth provides sufficient confidence in the accuracy of nanoindentation measure hardness. In this study, the irradiation induced hardening generally decreased with increasing temperature for both ion and neutron irradiation. Fig. 5.18 summarizes the evolution of Vickers hardness of T91 and HT9 with the irradiation temperature; the hardness tests were performed at room temperature. Although most of the samples were irradiated to about 18 dpa, the dual ion irradiated HT9:445 ℃:72 dpa, and neutron irradiated sample HT9:459 ℃:31 dpa were also included for comparison considering likely saturated hardening effects after ~10 dpa for HT9 steels [211]. The values from Ref. [212] on the same heats of T91 and HT9 alloys were added in the figure,

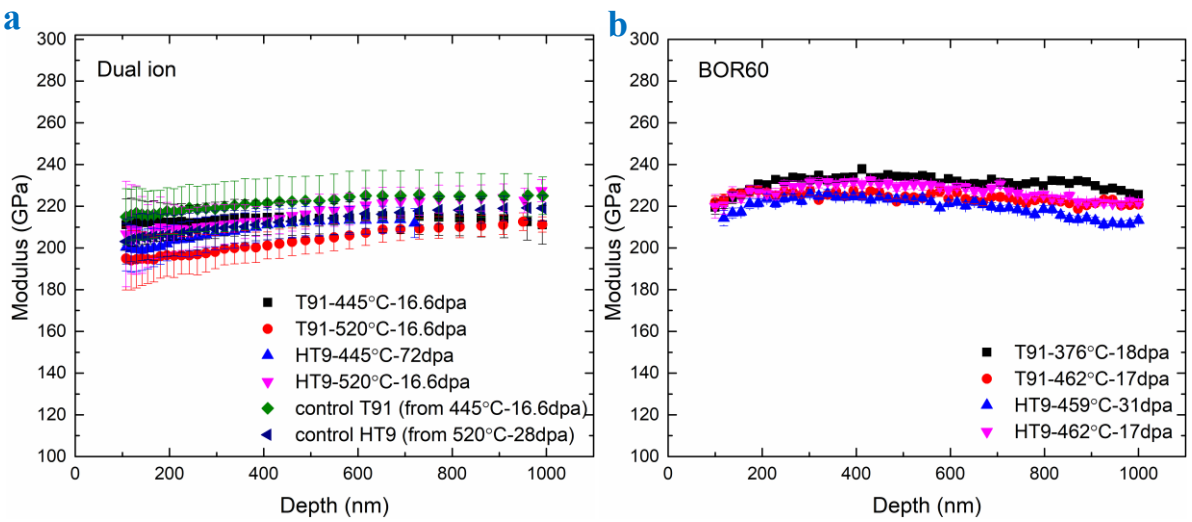

Fig. 5.17 The evolution of nanoindentation measured modulus with indentation depth for (a) ion and (b) neutron irradiated T91 and HT9 alloys. "control" refers to unirradiated region on the bulk sample.

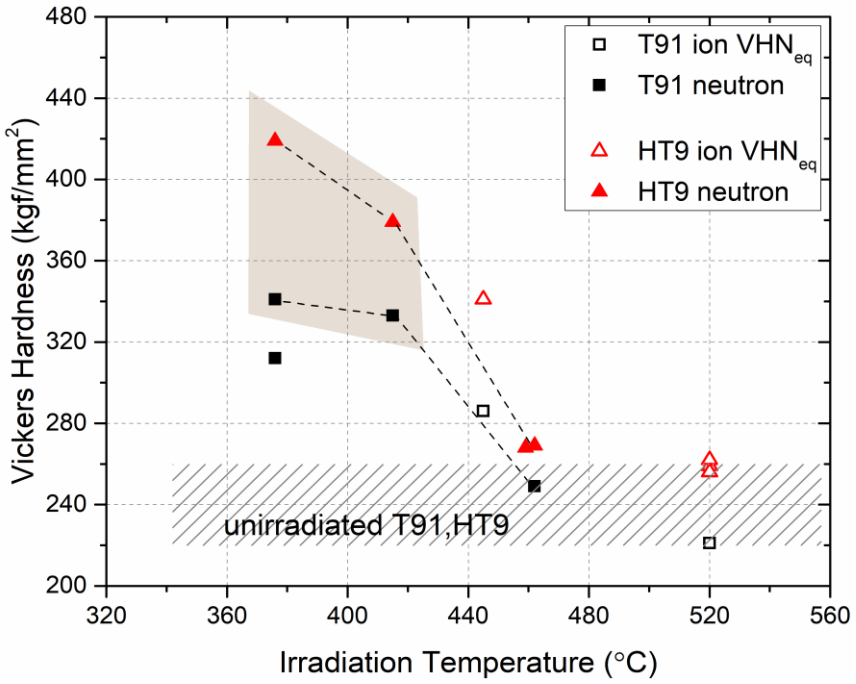

Fig. 5.18 Evolution of Vickers hardness with irradiation temperature. The tests were performed at room temperature. The shaded data points are from Ref. [181].

as shown in the shaded region. It is evident that pronounced irradiation hardening occurred below 420 ℃, followed by a rapid decrease of hardness in 420-460 ℃ regime. However, the irradiation induced hardening is miniscule at higher temperatures, with a hardness close to the unirradiated samples. Similar hardness evolution with irradiation temperature has been widely reported for the 9-12%Cr F/M steels [43,213]. A clear irradiation hardening was observed below 350 ℃ by Dai et al. on the neutron irradiated T91 samples [214]. In the 350-400 ℃ regime, only weak hardening occurred, while beyond 400-450 ℃, there is little or no hardening effect. The decline of irradiation hardening was also detected above 425 ℃ [211] and 400 ℃ [215] for HT9, as well as ~450 ℃ [216,217] for 9-12%Cr F/M steels subjected to neutron irradiation. The hardening for HT9 (12% Cr) in this study is higher than T91 (9% Cr), which is consistent with the prior studies [216] and may be attributable to α' precipitation.

The hardness for dual ion irradiated samples at 520 ℃ fell into the unirradiated region, with a ~60 ℃ shift compared to the neutron irradiation at around 460 ℃. Since little hardening or even softening occurred above 460 ℃, the comparable hardness between dual ion and neutron irradiated samples in this study does not support the 60 ℃ temperature shift as used in the swelling comparison. Meanwhile, in 420-460 ℃ regime, the hardness values of the ion irradiated samples (open symbols in Fig. 5.18) are close to the temperature-dependent trend of the neutron samples. This indicates that a simple 60 ℃ temperature shift may not be suitable for the entire broad temperature range (360-520 ℃).

5.3.4. Correlation between microstructures and mechanical properties

In section 5.2.3 we developed a new method to combine the strengthening contributions from different microstructures. In this section for the dual ion and neutron irradiated T91 and HT9 alloys, we will further include more complicated microstructures and test the model used in the previous sections. By detailed analysis on the hardening contribution from the microstructures and perform the comparison to the measured hardness, we can provide new insight about the fidelity of ion irradiation as a surrogate to neutron irradiation.

The measured strengths were still calculated based on nanoindentation measured bulk equivalent hardness and using $\sigma = 0.285\ H_0$. In the investigated T91 and HT9 alloys, dislocation lines, dislocation loops, cavities and Ni-rich precipitates were observed under dual ion and neutron irradiations. The DBH model was used to quantify the strengthening contribution from these microstructures. Besides the hardening components from these features, the solution hardening and base metal strength (pure Fe) was also used for the calculated strength. The pure

Fe strength, dislocation line and dislocation loop strengthening were calculated using the same method as described in section 5.2.3, and will not be repeated here.

The Ni-rich clusters were considered as spherical precipitates for simplicity, which is different from the coherent Cr-rich precipitates in section 5.2. The barrier strength factor α was calculated according to the equation below [167],

$$\alpha = \frac{0.135}{(1-\nu)^{1/2}\left(1-0.816d\sqrt{Nd}\right)} \ln\left[\frac{0.816d}{r_0}\right] \tag{5.17}$$

where d and N are the diameter and number density of the precipitates, respectively. The dislocation core radius r_0 is taken as 1.19b (b=0.247 nm) [167]. The cavities can be considered as in spherical shape and the strength factor was calculated by the equation below:

$$\alpha = \frac{0.383}{(1-\nu)^{\frac{1}{2}}\left(1-0.816d\sqrt{Nd}\right)} \ln\left[\frac{0.247d}{r_0}\left(1-0.816d\sqrt{Nd}\right)\right] \tag{5.18}$$

where the dislocation core radius r_0 is taken as 1.02b. Grain boundaries also provide a strengthening contribution due to relatively small grain sizes of T91 and HT9 alloys. The Hall-Patch equation [218] was applied to calculate this component:

$$\Delta\sigma_{gb} = k/\sqrt{d} \tag{5.19}$$

where k is a constant, and d is the average diameter of the grain boundary. k = 620 MPa· μm $^{1/2}$ was used in this study [219]. The grain sizes of T91 and HT9 are 9 μm [220] and 50 μm [221], respectively.

To combine the different strengthening components, the same superposition method described in section 5.2.3 was used. In this study, the pure Fe strength ($\Delta\sigma_{Fe}$), solution hardening ($\Delta\sigma_{ss}$), and cavities < 2nm ($\Delta\sigma_{c<2}$) are weak obstacles, while the Ni-rich precipitates ($\Delta\sigma_{Ni}$), dislocation lines ($\Delta\sigma_{line}$), dislocation loops ($\Delta\sigma_{<100>}$ and $\Delta\sigma_{1/2<111>}$), cavities > 2nm ($\Delta\sigma_{c>2}$) and grain boundaries ($\Delta\sigma_{gb}$) are considered as strong obstacles. The final superposition equation is as follow:

$$\sigma_y = \sqrt{\Delta\sigma_{Fe}^2 + \Delta\sigma_{ss}^2 + \Delta\sigma_{c<2}^2} + \sqrt{\Delta\sigma_{Ni}^2 + \Delta\sigma_{line}^2 + \Delta\sigma_{<100>}^2 + \Delta\sigma_{1/2<111>}^2 + \Delta\sigma_{c>2}^2 + \Delta\sigma_{gb}^2} \tag{5.20}$$

Fig. 5.19a shows the correlation between model-predicted strength and measured strength (converted from nanoindentation). For both dual ion and neutron irradiation, the data points fall close to the ideal 1:1 line. This good agreement indicates that nanoindentation offers the

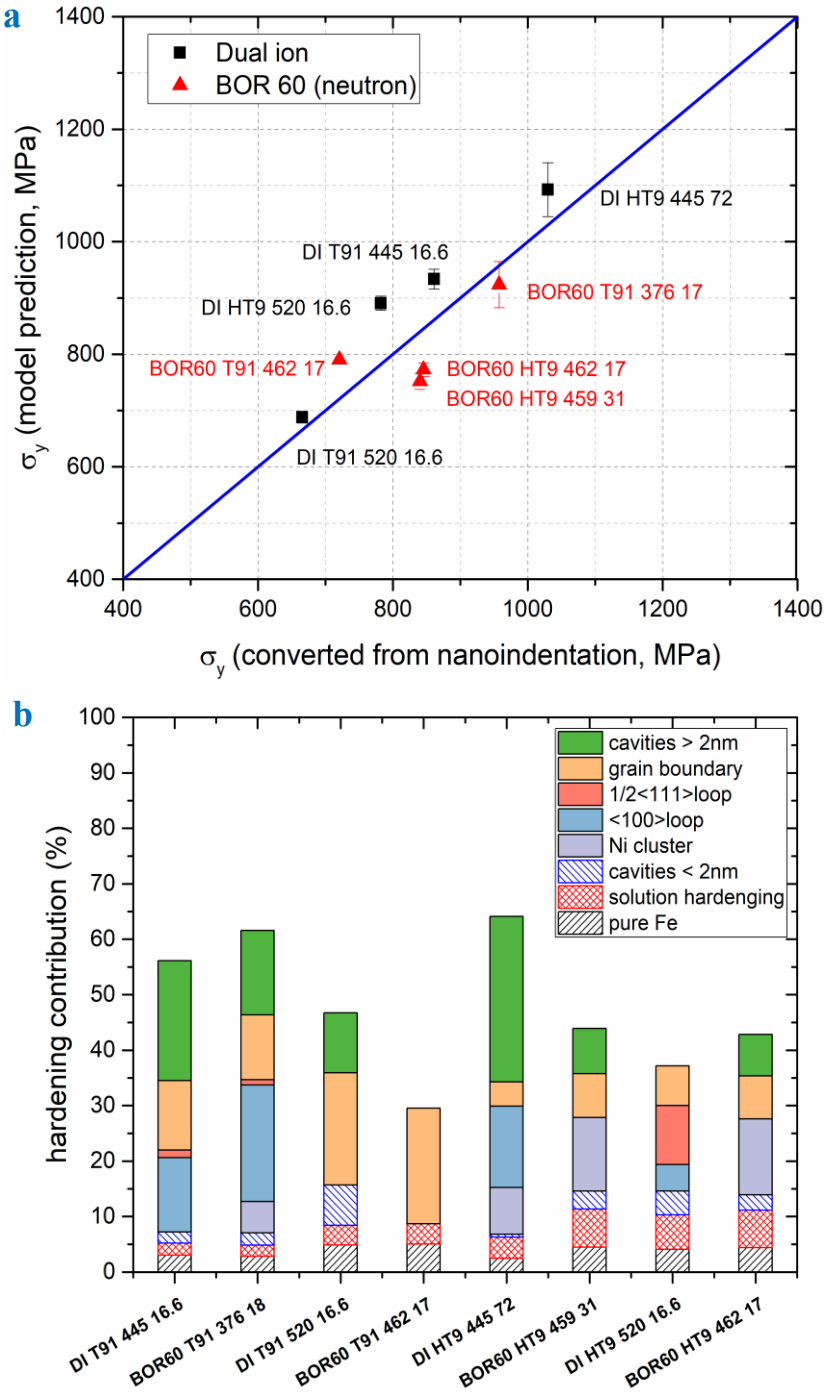

Fig. 5.19 (a) Correlation between model predicted strength and the measured strength. (b) strengthening contribution from every microstructure. The rest of the contribution is from dislocation lines and was not plotted in the figure.

potential to accurately predict bulk mechanical strength (within ~10% accuracy) in nano scale volumes. Meanwhile, since the model prediction and measurement were performed independently, the good correlation between them demonstrates the feasibility to use the strengthening model as well as the superposition method in this study to predict the strengths from the microstructure aspects. A detailed comparison of the strengthening contribution between neutron and ion irradiation is shown in Fig. 5.19b. The dual ion sample and its corresponding neutron sample with a ~60 ℃ temperature shift are listed in coupled pairs in Fig. 5.19b for clear comparison. The rest of the contribution is from the dislocation lines and were not plotted in Fig. 5.19b since they represent the remaining space above each bar. This comparison provides another perspective of the problem of using a simplistic 60 ℃ temperature shift for the neutron vs. ion irradiation conditions. The corresponding neutron and ion irradiation pairs of hardening data did not share the similar percentage of the individual strengthening contribution (stacked bars in Fig. 5.19b), which is a reflection of their inconsistent microstructures especially for HT9 alloys.

CHAPTER 6. CONCLUSIONS

There are three objectives of this study: (1) develop a protocol for nanoindentation study on the ion-irradiated Fe-Cr alloys; (2) develop well-calibrated, physically based models to predict change in mechanical properties of irradiated alloys; and (3) provide more insight on the potential to simulate reactor irradiation by ion irradiation in the aspect of mechanical properties of the Fe-Cr alloys. To achieve these objectives, we investigated the microstructure evolution and mechanical properties of high purity binary FeCr alloys under thermal aging and ion irradiations, as well as T91 and HT9 under neutron and dual ion irradiation. The purpose of this work is to provide an accurate methodology for nanoindentation testing and to obtain an important database for future prediction on mechanical properties of new materials solely from microstructural aspect. The key observations and conclusions drawn for each of the three objectives are listed below.

6.1. Nanoindentation test protocol

The work was focused on nanoindentation testing of high purity Fe and Fe alloys containing 3-25 wt. %Cr in the as-annealed condition as well as thermally aged (100-900 hours at 475 ℃) Fe14 wt. %Cr, Fe18 wt. %Cr and Fe25 wt. %Cr. This set of alloys provided a wide range of alloy hardness (~50 to 350 VHN) for investigation of relationships between nanoindentation and bulk hardness. The challenges to obtaining accurate quantitative estimates of bulk equivalent hardness via nanoindentation testing at low indent depths were analyzed, with the following main conclusions:

(1) Nix-Gao analysis, selection of the appropriate contact depth (h_c=h) and pileup corrections are the three most important factors for obtaining quantitatively accurate (within ~10%) bulk equivalent hardness values from nanoindentation measurements. The indentation size effect length-scale parameter (h^*) generally decreased with increasing alloy hardness, although there was considerable variability in the detailed h^* values for the solid solution alloys. Consideration of pileup effects produced hardness corrections of 5% to 14% for the investigated materials.

(2) Estimating the hardness change at a reference load or depth by simply measuring the hardness ratio or raw hardness change will induce hardness uncertainties much higher than 10% due to ISE, as indicated by the scale parameter h^* shown in Eq. 2.12.

(3) Both constant strain rate (0.05 to 0.5 /s) and constant loading rate test methods provided comparable nanoindentation bulk equivalent hardness, which was attributed to the

relatively weak slight strain rate sensitivity that was measured in dedicated strain rate tests for the investigated Fe-Cr materials at room temperature. For materials whose strength are sensitive to strain rate, constant strain rate tests should be utilized.

(4) Nanoindentation tests on fine mechanically polished samples can produce comparable extrapolated Nix-Gao bulk hardness (H_0) as electropolished samples. Similarly, indentation testing in grains with different surface normal orientations ([001], [110], [111]) and under constant loading rate vs. constant strain rate test conditions yielded comparable H_0 results.

(5) Significant curvature in the Nix-Gao plots was frequently observed at indent depths near 150 nm. The nanoindentation testing procedures (CSR versus CLR test methods, surface preparation, pileup corrections) did not eliminate the observed curvatures. The possible causes of the curvatures include non-ideal indenter tip and inability of the material to achieve the geometrically necessary dislocation density underneath the indenter at low indent depths that is assumed by the Nix-Gao model. This nonlinearity may introduce significant errors when trying to obtain quantitative strength values at indent depths <150-200 nm. Considering that elastic strain fields extend to ~5 to 7 times deeper than the indent depth, this makes it difficult to extract quantitatively accurate bulk equivalent strength values from surface modified layers less than 1000 nm.

(6) The observed good quantitative agreement between the predicted strength changes associated with solid solution hardening and nanoscale precipitates using either the dispersed barrier hardening, or Friedel-Kroupa-Hirsch model compared with measured nanoindentation strength change (Nix-Gao bulk equivalent hardness with pileup corrections) indicates that nanoindentation offers the potential to accurately predict bulk mechanical strength (within ~10% accuracy) in nano scale volumes.

6.2. Microstructure evolution and mechanical properties of ion irradiated Fe18Cr

The work was focused on TEM and APT characterization of the microstructures (dislocation loops, α' precipitates) and nanoindentation testing of high purity binary alloy Fe18Cr, which was subject to heavy-ion irradiation using 8 MeV Fe^{2+} at 300-450 °C to 0.37 and 3.7 dpa with dose rates of ~10^{-5}-10^{-3} dpa/s. The nanoindentation test protocol developed on the thermally aged FeCr alloys was applied. The hardening values were compared with theoretical estimates from dispersed barrier hardening models based on detailed transmission electron microscopy characterization of the irradiated microstructures. The main conclusions are as follows:

(1) 8 MeV Fe^{2+} irradiation induced black dots and dislocation loops in the investigated Fe18Cr alloy. The formation of black dots is dependent on the temperatures and dose rate, with a threshold temperature of 350 ℃ under 10^{-3} dap/s and a threshold dose rate of 10^{-4} dpa/s at 300 ℃. The black dots were mainly decorated on the dislocations, which was attributed to the strain field around the dislocations that can trap the small defects.

(2) The black dots were inferred as the precursor of dislocation loops, with both 1/2<111> and <100> types. They were transformed into dislocation loops at 450 ℃, and all the loops were <100> type, possibly due to the transformation of 1/2<111> to <100>.

(3) Model prediction of the strength requires an appropriate superposition method for each microstructure contribution. The conventional method to compare the yield change based on Eq. 5.11 is questionable due to the possible existence of both weak and strong strengthening components. A new method using root sum square superposition for similar strengths and linear superposition for different strengths worked well and resulted in a good agreement with the measured strengths on the ion irradiated Fe18Cr.

(4) The great agreement between the measured strengths and model predicted strengths indicates the accuracy of both the nanoindentation testing protocol developed in our studies, and the reasonable quantitative accuracy of the strength factors in the hardening model calculated solely based on the microstructure density and size.

6.3. Insight in ion irradiation as a surrogate of neutron irradiation

This work extends the previous research from the simple binary alloy to the commercial 9-12%Cr ferritic-martensitic alloys T91 and HT9, which were subjected to both fission neutron (BOR60 reactor) and dual-ion (9MeV Fe^{3+} and 3.24MeV He^{2+}) irradiations from 376 to 520 ℃ with damage levels from 16.6 to 72 dpa. The microstructures and mechanical properties were compared between neutron and dual ion irradiation to quantify the possibility of using ion irradiation to simulate neutron irradiation. Nanoindentation testing protocol and microstructure-based model for strength estimation were applied. The main conclusion are as follows:

(1) Nanoindentation with pileup correction is important and effective for obtaining quantitatively accurate bulk equivalent hardness values for ion and neutron irradiated materials.

(2) The temperature shift theory works generally well for the cavities and dislocation loops observed in T91 following ion and neutron irradiations, but it is not suitable for the match

of precipitates. Especially for the HT9 material, both dislocation loop and precipitate evolution didn't follow the calculated temperature shift.

(3) The comparable nanoindentation results from dual-ion and neutron irradiated T91 and HT9 at elevated temperatures (>450 ℃) may be largely due to the minimal irradiation hardening at elevated temperatures. The discrepancy in the microstructures indicates that more complex modeling should be used to link ion vs neutron irradiation microstructures and hardening.

(4) The newly developed superposition method developed for ion irradiated Fe18Cr also worked well on the dual ion and neutron irradiated commercial alloys, indicating that this superposition method is likely to be universal.

LIST OF REFERENCES

[1] R.L. Klueh, D.R. Harries, High-chromium ferritic and martensitic steels for nuclear applications, ASTM, W. Conshohocken, PA, 2001.

[2] P. Hosemann, C. Vieh, R.R. Greco, S. Kabra, J.A. Valdez, M.J. Cappiello, S.A. Maloy, Nanoindentation on ion irradiated steels, J. Nucl. Mater. 389 (2009) 239–247. https://doi.org/10.1016/j.jnucmat.2009.02.026.

[3] P. Hosemann, Y. Dai, E. Stergar, H. Leitner, E. Olivas, A.T. Nelson, S.A. Maloy, Large and Small Scale Materials Testing of HT-9 Irradiated in the STIP Irradiation Program, Exp Mech. 51 (2011) 1095–1102. https://doi.org/10.1007/s11340-010-9419-2.

[4] P. Hosemann, C. Shin, D. Kiener, Small scale mechanical testing of irradiated materials, J. Mater. Res. 30 (2015) 1231–1245. https://doi.org/10.1557/jmr.2015.26.

[5] W.C. Oliver, G.M. Pharr, An improved technique for determining hardness and elastic modulus using load and displacement sensing indentation experiments, J. Mater. Res. 7 (1992) 1564–1583.

[6] D. Tabor, The hardness and strength of metals, J. Inst. Metals. 79 (1951) 1–18.

[7] Y. Yang, C. Zhang, Z. Ding, C. Su, T. Yan, Y. Song, Y. Cheng, A correlation between micro- and nano-indentation on materials irradiated by high-energy heavy ions, J. Nucl. Mater. 498 (2018) 129–136.

[8] K. Yabuuchi, Y. Kuribayashi, S. Nogami, R. Kasada, A. Hasegawa, Evaluation of irradiation hardening of proton irradiated stainless steels by nanoindentation, J. Nucl. Mater. 446 (2014) 142–147.

[9] S. Chen, Y. Miyahara, A. Nomoto, K. Nishida, Effects of thermal aging and low-fluence neutron irradiation on the mechanical property and microstructure of ferrite in cast austenitic stainless steels, Acta. Mater. 179 (2019) 61–69.

[10] W.D. Nix, H. Gao, Indentation size effects in crystalline materials: a law for strain gradient plasticity, J. Mech. Phys. Solids. 46 (1998) 411–425.

[11] S.J. Zinkle, J.T. Busby, Structural materials for fission & fusion energy, Materials Today. 12 (2009) 12–19. https://doi.org/10.1016/S1369-7021(09)70294-9.

[12] M. Igarashi, Y. Sawaragi, Development of 0.1C-11Cr-3W-3Co-V-Nb-Ta-Nd-N ferritic steel for USC boilers, in: Tokyo, Japan, 1997: pp. 107–112.

[13] J.Z. Briggs, T.D. Parker, The Super 12 % Cr Steels, 2. print. by McNaughton & Gunn, Climax Molybdenum Co., New York, NY, 1982.

[14] R.L. Klueh, E.E. Bloom, The development of ferritic steels for fast induced-radioactivity

decay for fusion reactor applications, Nuclear Engineering and Design. Fusion. 2 (1985) 383–389. https://doi.org/10.1016/0167-899X(85)90026-6.

[15] H. Cerjak, V. Foldyna, P. Hofer, B. Schaffernak, in: Microstructural development and stability in high chromium ferritic power plant steels, London, Institute of Materials, 1997: pp. 145–158.

[16] M. Tamura, H. Hayakawa, A. Yoshitake, A. Hishinuma, T. Kondo, Phase stability of reduced activation ferritic steel: 8%Cr-2%W-0.2%V-0.04%Ta-Fe, J. Nucl. Mater. 155–157 (1988) 620–625. https://doi.org/10.1016/0022-3115(88)90384-4.

[17] R. Lagneborg, Deformation in an iron-30% chromium alloy aged at 475°c, Acta. Mater. 15 (1967) 1737–1745. https://doi.org/10.1016/0001-6160(67)90065-X.

[18] P.J. Grobner, The 885° f (475° c) embrittlement of ferritic stainless steels, MT. 4 (1973) 251–260. https://doi.org/10.1007/BF02649625.

[19] G. Bonny, D. Terentyev, L. Malerba, On the α–α′ miscibility gap of Fe–Cr alloys, Scr. Mater. 59 (2008) 1193–1196. https://doi.org/10.1016/j.scriptamat.2008.08.008.

[20] L. Huang, X. Hu, C. Yang, W. Yan, F. Xiao, Y. Shan, K. Yang, Influence of thermal aging on microstructure and mechanical properties of CLAM steel, J. Nucl. Mater. 443 (2013) 479–483. https://doi.org/10.1016/j.jnucmat.2013.08.008.

[21] V. Sklenicka, Long-term creep behavior of 9–12%Cr power plant steels, Mater. Charact. 51 (2003) 35–48. https://doi.org/10.1016/j.matchar.2003.09.012.

[22] E.H. Lee, P.J. Maziasz, A.F. Rowcliffe, Structure and composition of phases occurring in austenitic stainless steels in thermal and irradiation environments, Oak Ridge National Lab. (1980) 29.

[23] M. Nastar, F. Soisson, 1.08 - Radiation-Induced Segregation☆, in: R.J.M. Konings, R.E. Stoller (Eds.), Comprehensive Nuclear Materials (Second Edition), Elsevier, Oxford, 2020: pp. 235–264. https://doi.org/10.1016/B978-0-12-803581-8.00668-8.

[24] C. Zheng, M.A. Auger, M.P. Moody, D. Kaoumi, Radiation induced segregation and precipitation behavior in self-ion irradiated Ferritic/Martensitic HT9 steel, J. Nucl. Mater. 491 (2017) 162–176. https://doi.org/10.1016/j.jnucmat.2017.04.040.

[25] K.G. Field, X. Hu, K.C. Littrell, Y. Yamamoto, L.L. Snead, Radiation tolerance of neutron-irradiated model Fe–Cr–Al alloys, J. Nucl. Mater. 465 (2015) 746–755.

[26] C. Pareige, V. Kuksenko, P. Pareige, Behaviour of P, Si, Ni impurities and Cr in self ion irradiated Fe–Cr alloys – Comparison to neutron irradiation, J. Nucl. Mater. 456 (2015) 471–476. https://doi.org/10.1016/j.jnucmat.2014.10.024.

[27] E.R. Reese, N. Almirall, T. Yamamoto, S. Tumey, G. Robert Odette, E.A. Marquis, Dose rate dependence of Cr precipitation in an ion-irradiated Fe 18Cr alloy, Scr. Mater. 146 (2018) 213–217. https://doi.org/10.1016/j.scriptamat.2017.11.040.

[28] D.S. Gelles, Microstructural examination of neutron-irradiated simple ferritic alloys, J. Nucl. Mater. 108–109 (1982) 515–526. https://doi.org/10.1016/0022-3115(82)90523-2.

[29] R. Schäublin, B. Décamps, A. Prokhodtseva, J.F. Löffler, On the origin of primary ½ a0 and a0 loops in irradiated Fe(Cr) alloys, Acta. Mater. 133 (2017) 427–439. https://doi.org/10.1016/j.actamat.2017.02.041.

[30] Y. Katoh, A. Kohyama, D.S. Gelles, Swelling and dislocation evolution in simple ferritic alloys irradiated to high fluence in FFTF/MOTA, J. Nucl. Mater. 225 (1995) 154–162. https://doi.org/10.1016/0022-3115(94)00669-5.

[31] C. Zheng, E.R. Reese, K.G. Field, E. Marquis, S.A. Maloy, D. Kaoumi, Microstructure response of ferritic/martensitic steel HT9 after neutron irradiation: effect of dose, J. Nucl. Mater. 523 (2019) 421–433. https://doi.org/10.1016/j.jnucmat.2019.06.019.

[32] C. Zheng, E.R. Reese, K.G. Field, T. Liu, E.A. Marquis, S.A. Maloy, D. Kaoumi, Microstructure response of ferritic/martensitic steel HT9 after neutron irradiation: Effect of temperature, J. Nucl. Mater. 528 (2020) 151845. https://doi.org/10.1016/j.jnucmat.2019.151845.

[33] B.H. Sencer, J.R. Kennedy, J.I. Cole, S.A. Maloy, F.A. Garner, Microstructural analysis of an HT9 fuel assembly duct irradiated in FFTF to 155dpa at 443°C, J. Nucl. Mater. 393 (2009) 235–241. https://doi.org/10.1016/j.jnucmat.2009.06.010.

[34] L. Tan, B.K. Kim, Y. Yang, K.G. Field, S. Gray, M. Li, Microstructural evolution of neutron-irradiated T91 and NF616 to ~4.3 dpa at 469 °C, J. Nucl. Mater. 493 (2017) 12–20. https://doi.org/10.1016/j.jnucmat.2017.05.041.

[35] B.H. Sencer, J.R. Kennedy, J.I. Cole, S.A. Maloy, F.A. Garner, Microstructural stability of an HT-9 fuel assembly duct irradiated in FFTF, J. Nucl. Mater. 414 (2011) 237–242. https://doi.org/10.1016/j.jnucmat.2011.03.050.

[36] C. Zheng, S. Maloy, D. Kaoumi, Effect of dose on irradiation-induced loop density and Burgers vector in ion-irradiated ferritic/martensitic steel HT9, Philos. Mag. 98 (2018) 2440–2456. https://doi.org/10.1080/14786435.2018.1490825.

[37] M.L. Grossbeck, 1.05 - Effect of Radiation on Strength and Ductility of Metals and Alloys, in: R.J.M. Konings, R.E. Stoller (Eds.), Comprehensive Nuclear Materials (Second Edition), Elsevier, Oxford, 2012: pp. 130–152. https://doi.org/10.1016/B978-0-08-102865-0.00004-2.

[38] C.-C. Fu, F. Willaime, Ab initio study of helium in α − Fe : Dissolution, migration, and clustering with vacancies, Phys. Rev. B. 72 (2005) 064117. https://doi.org/10.1103/PhysRevB.72.064117.

[39] S.J. Zinkle, G.S. Was, Materials challenges in nuclear energy, Acta. Mater. 61 (2013) 735–758. https://doi.org/10.1016/j.actamat.2012.11.004.

[40] E. Gaganidze, J. Aktaa, Assessment of neutron irradiation effects on RAFM steels, Fusion Engineering and Design. 88 (2013) 118–128. https://doi.org/10.1016/j.fusengdes.2012.11.020.

[41] C.E. Kessel, J.P. Blanchard, A. Davis, L. El-Guebaly, L.M. Garrison, N.M. Ghoniem, P.W. Humrickhouse, Y. Huang, Y. Katoh, A. Khodak, E.P. Marriott, S. Malang, N.B. Morley, G.H. Neilson, J. Rapp, M.E. Rensink, T.D. Rognlien, A.F. Rowcliffe, S. Smolentsev, L.L. Snead, M.S. Tillack, P. Titus, L.M. Waganer, G.M. Wallace, S.J. Wukitch, A. Ying, K. Young, Y. Zhai, Overview of the fusion nuclear science facility, a credible break-in step on the path to fusion energy, Fusion Eng. Des. 135 (2018) 236–270. https://doi.org/10.1016/j.fusengdes.2017.05.081.

[42] S.J. Zinkle, N.M. Ghoniem, Operating temperature windows for fusion reactor structural materials, Fusion Eng. Des. 51–52 (2000) 55–71. https://doi.org/10.1016/S0920-3796(00)00320-3.

[43] A. Bhattacharya, S.J. Zinkle, J. Henry, S.M. Levine, P.D. Edmondson, M.R. Gilbert, H. Tanigawa, C.E. Kessel, Irradiation damage concurrent challenges with RAFM and ODS steels for fusion reactor first-wall/blanket: a review, J. Phys. Energy. 4 (2022) 034003. https://doi.org/10.1088/2515-7655/ac6f7f.

[44] A.S. Tetelman, A.J. McEvily, in: Fracture of Structural Materials, New York, Wiley, 1967: p. 178.

[45] J.R. Hawthorne, Irradiation Embrittlement, in: Treatise on Materials Science & Technology, Elsevier, 1983: pp. 461–524. https://doi.org/10.1016/B978-0-12-341825-8.50016-7.

[46] G.R. Odette, On the ductile to brittle transition in martensitic stainless steels — Mechanisms, models and structural implications, J. Nucl. Mater. 212–215 (1994) 45–51. https://doi.org/10.1016/0022-3115(94)90032-9.

[47] I. Belianov, P. Marmy, The effect of low dose irradiation on the impact fracture energy and tensile properties of pure iron and two ferritic martensitic steels, J. Nucl. Mater. (1998) 5.

[48] R. Klueh, D. Alexander, Irradiation Effects on Impact Behavior of 12Cr-1MoVW and 2¼Cr-1Mo Steels, in: R. Stoller, A. Kumar, D. Gelles (Eds.), Effects of Radiation on

Materials: 15th International Symposium, ASTM International, West Conshohocken, PA, 1992: pp. 1256–1266. https://doi.org/10.1520/STP17944S.

[49] W.-L. Hu, D. Gelles, The Ductile-to-Brittle Transition Behavior of Martensitic Steels Neutron Irradiated to 26 dpa, in: F. Garner, C. Henager, N. Igata (Eds.), Influence of Radiation on Material Properties: 13th International Symposium (Part II), ASTM International, West Conshohocken, PA, 1987: pp. 83–97. https://doi.org/10.1520/STP25642S.

[50] R.L. Klueh, J.M. Vitek, Elevated-temperature tensile properties of irradiated 9 Cr-1 MoVNb steel, J. Nucl. Mater. 132 (1985) 27–31. https://doi.org/10.1016/0022-3115(85)90389-7.

[51] R.L. Klueh, J.M. Vitek, Tensile behavior of irradiated 12Cr-1MoVW steel, J. Nucl. Mater. 137 (1985) 44–50. https://doi.org/10.1016/0022-3115(85)90047-9.

[52] J.H. Gittus, Theory of dislocation-creep due to the frenkel defects or interstitialcies produced by bombardment with energetic particles, Philos. Mag. 25 (1972) 345–354. https://doi.org/10.1080/14786437208226809.

[53] P.T. Heald, M.V. Speight, Steady-state irradiation creep, Philos. Mag. 29 (1974) 1075–1080. https://doi.org/10.1080/14786437408226592.

[54] R. Bullough, J.R. Willis, The stress-induced point defect-dislocation interaction and its relevance to irradiation creep, Philos. Mag. 31 (1975) 855–861. https://doi.org/10.1080/14786437508229635.

[55] W.G. Wolfer, M. Ashkin, Diffusion of vacancies and interstitials to edge dislocations, J. Appl. Phys. 47 (1976) 791–800. https://doi.org/10.1063/1.322710.

[56] L.K. Mansur, Irradiation creep by climb-enabled glide of dislocations resulting from preferred absorption of point defects, Philos. Mag. A. 39 (1979) 497–506. https://doi.org/10.1080/01418617908239286.

[57] L.K. Mansur, Theory of transitions in dose dependence of radiation effects in structural alloys, J. Nucl. Mater. 206 (1993) 306–323. https://doi.org/10.1016/0022-3115(93)90130-Q.

[58] N.H. Packan, K. Farrell, J.O. Stiegler, Correlation of neutron and heavy-ion damage, J. Nucl. Mater. 78 (1978) 143–155. https://doi.org/10.1016/0022-3115(78)90513-5.

[59] N.Q. Lam, S.J. Rothman, R. Sizmanns, Steady-state point-defect diffusion profiles in solids during irradiation, Radiation Effects. 23 (1974) 53–59. https://doi.org/10.1080/00337577408232045.

[60] A.D. Brailsford, L.K. Mansur, Effect of self-ion injection in simulation studies of void

swelling, J. Nucl. Mater. 71 (1977) 110–116. https://doi.org/10.1016/0022-3115(77)90194-5.

[61] S.J. Zinkle, L.L. Snead, Opportunities and limitations for ion beams in radiation effects studies: Bridging critical gaps between charged particle and neutron irradiations, Scr. Mater. 143 (2018) 154–160. https://doi.org/10.1016/j.scriptamat.2017.06.041.

[62] D. Kiener, W. Grosinger, G. Dehm, R. Pippan, A further step towards an understanding of size-dependent crystal plasticity: In situ tension experiments of miniaturized single-crystal copper samples, Acta Materialia. 56 (2008) 580–592. https://doi.org/10.1016/j.actamat.2007.10.015.

[63] H.T. Vo, O. Anderoglu, P. Hosemann, S.A. Maloy, The effects of microstructures and radiation damage on the deformation behavior of a HT-9 alloy using microtensile testing, Mater. Charact. 174 (2021) 110972. https://doi.org/10.1016/j.matchar.2021.110972.

[64] T. Miura, K. Fujii, K. Fukuya, M. Ando, H. Tanigawa, Micro-tensile testing of reduced-activation ferritic steel F82H irradiated with Fe and He ions, Nuclear Materials and Energy. 17 (2018) 24–28. https://doi.org/10.1016/j.nme.2018.08.004.

[65] K.E. Johanns, A. Sedlmayr, P. Sudharshan Phani, R. Mönig, O. Kraft, E.P. George, G.M. Pharr, In-situ tensile testing of single-crystal molybdenum-alloy fibers with various dislocation densities in a scanning electron microscope, J. Mater. Res. 27 (2012) 508–520. https://doi.org/10.1557/jmr.2011.298.

[66] D.M. Dimiduk, M.D. Uchic, T.A. Parthasarathy, Size-affected single-slip behavior of pure nickel microcrystals, Acta Materialia. 53 (2005) 4065–4077. https://doi.org/10.1016/j.actamat.2005.05.023.

[67] S. Shim, H. Bei, M.K. Miller, G.M. Pharr, E.P. George, Effects of focused ion beam milling on the compressive behavior of directionally solidified micropillars and the nanoindentation response of an electropolished surface, Acta. Mater. 57 (2009) 503–510. https://doi.org/10.1016/j.actamat.2008.09.033.

[68] H. Bei, S. Shim, E. George, M. Miller, E. Herbert, G. Pharr, Compressive strengths of molybdenum alloy micro-pillars prepared using a new technique, Scr. Mater. 57 (2007) 397–400. https://doi.org/10.1016/j.scriptamat.2007.05.010.

[69] H. Bei, S. Shim, M.K. Miller, G.M. Pharr, E.P. George, Effects of focused ion beam milling on the nanomechanical behavior of a molybdenum-alloy single crystal, Appl. Phys. Lett. 91 (2007) 111915. https://doi.org/10.1063/1.2784948.

[70] D. Kiener, C. Motz, G. Dehm, Micro-compression testing: A critical discussion of experimental constraints, Mater. Sci. Eng. A. 505 (2009) 79–87.

https://doi.org/10.1016/j.msea.2009.01.005.

[71] M.B. Lowry, D. Kiener, M.M. LeBlanc, C. Chisholm, J.N. Florando, J.W. Morris, A.M. Minor, Achieving the ideal strength in annealed molybdenum nanopillars, Acta. Mater. 58 (2010) 5160–5167. https://doi.org/10.1016/j.actamat.2010.05.052.

[72] S. Özerinç, R.S. Averback, W.P. King, In situ creep measurements on micropillar samples during heavy ion irradiation, J. Nucl. Mater. 451 (2014) 104–110. https://doi.org/10.1016/j.jnucmat.2014.03.037.

[73] A simple theory of static and dynamic hardness, Proc. R. Soc. Lond. A. 192 (1948) 247–274. https://doi.org/10.1098/rspa.1948.0008.

[74] N.A. Stilwell, D. Tabor, Elastic Recovery of Conical Indentations, Proceedings of the Physical Society. 78 (1961) 169–179. https://doi.org/10.1088/0370-1328/78/2/302.

[75] A. Ternovskii, V. Alekhin, M.K. Shorshorov, M. Khrushchev, V. Skvortsov, The character of the variation of microhardness with indentation size and the deformation behavior of materials under conditions of concentrated surface loading, Zavodskaya Laboratoriya. 39 (1973) 20.

[76] S. Bulychev, V. Alekhin, M. Shorshorov, A. Ternovskii, G. Shnyrev, Determining Young's modulus from the indentor penetration diagram, Ind. Lab. 41 (1975) 1409–1412.

[77] S.I. Bulychev, V.P. Alekhin, M.Kh. Shorshorov, A.P. Ternovskii, Mechanical properties of materials studied from kinetic diagrams of load versus depth of impression during microimpression, Strength Mater. 8 (1976) 1084–1089. https://doi.org/10.1007/BF01529860.

[78] M. Shorshorov, B. SI, THE WORK OF PLASTIC AND ELASTIC DEFORMATION DURING INDENTATION, (1981).

[79] S. Bulychev, V. Alekhin, Method of kinetic hardness and microhardness in testing impression by an indentor, Industrial Laboratory. 53 (1988) 1091–1096.

[80] G.M. Pharr, E.G. Herbert, Y. Gao, The Indentation Size Effect: A Critical Examination of Experimental Observations and Mechanistic Interpretations, Annu. Rev. Mater. Res. 40 (2010) 271–292.

[81] N.A. Fleck, G.M. Muller, M.F. Ashby, J.W. Hutchinson, Strain gradient plasticity: Theory and experiment, Acta Metallurgica et Materialia. 42 (1994) 475–487. https://doi.org/10.1016/0956-7151(94)90502-9.

[82] M. Shell De Guzman, G. Neubauer, P. Flinn, W.D. Nix, The Role of Indentation Depth on the Measured Hardness of Materials, MRS Proceedings. 308 (1993) 613. https://doi.org/10.1557/PROC-308-613.

[83] Q. Ma, D.R. Clarke, Size dependent hardness of silver single crystals, J. Mater. Res. 10 (1995) 853–863. https://doi.org/10.1557/JMR.1995.0853.

[84] J.G. Swadener, E.P. George, G.M. Pharr, The correlation of the indentation size effect measured with indenters of various shapes, J. Mech. Phys. Solids. 50 (2002) 681–694.

[85] Y. Huang, F. Zhang, K. Hwang, W. Nix, G. Pharr, G. Feng, A model of size effects in nano-indentation, J. Mech. Phys. Solids. 54 (2006) 1668–1686.

[86] A. Ruiz-Moreno, P. Hähner, Indentation size effects of ferritic/martensitic steels: A comparative experimental and modelling study, Mater. Des. 145 (2018) 168–180.

[87] G.M. Pharr, J.H. Strader, W.C. Oliver, Critical issues in making small-depth mechanical property measurements by nanoindentation with continuous stiffness measurement, J. Mater. Res. 24 (2009) 653–666.

[88] K. Durst, B. Backes, M. Göken, Indentation size effect in metallic materials: Correcting for the size of the plastic zone, Scr. Mater. 52 (2005) 1093–1097.

[89] G. Feng, W.D. Nix, Indentation size effect in MgO, Scr. Mater. 51 (2004) 599–603.

[90] K. Durst, O. Franke, A. Böhner, M. Göken, Indentation size effect in Ni–Fe solid solutions, Acta. Mater. 55 (2007) 6825–6833.

[91] A. Bolshakov, G.M. Pharr, Influences of pileup on the measurement of mechanical properties by load and depth sensing indentation techniques, J. Mater. Res. 13 (1998) 1049–1058.

[92] C.D. Hardie, S.G. Roberts, A.J. Bushby, Understanding the effects of ion irradiation using nanoindentation techniques, J. Nucl. Mater. 462 (2015) 391–401.

[93] K.O. Kese, Z.C. Li, B. Bergman, Method to account for true contact area in soda-lime glass during nanoindentation with the Berkovich tip, Mater. Sci. Eng. A. 404 (2005) 1–8.

[94] C. Heintze, F. Bergner, S. Akhmadaliev, E. Altstadt, Ion irradiation combined with nanoindentation as a screening test procedure for irradiation hardening, J. Nucl. Mater. 472 (2016) 196–205.

[95] K. Kese, Z.C. Li, Semi-ellipse method for accounting for the pile-up contact area during nanoindentation with the Berkovich indenter, Scr. Mater. 55 (2006) 699–702.

[96] L.E. Samuels, T.O. Mulhearn, An experimental investigation of the deformed zone associated with indentation hardness impressions, J. Mech. Phys. Solids. 5 (1957) 125–134.

[97] K.L. Johnson, The correlation of indentation experiments, J. Mech. Phys. Solids. 18 (1970) 115–126. https://doi.org/10.1016/0022-5096(70)90029-3.

[98] C.L. Woodcock, D.F. Bahr, Plastic zone evolution around small scale indentations, Scr. Mater. 43 (2000) 783–788. https://doi.org/10.1016/S1359-6462(00)00489-9.

[99] P. Hosemann, D. Kiener, Y. Wang, S.A. Maloy, Issues to consider using nano indentation on shallow ion beam irradiated materials, J. Nucl. Mater. 425 (2012) 136–139.

[100] G.M. Pharr, W.C. Oliver, Measurement of Thin Film Mechanical Properties Using Nanoindentation, MRS Bull. 17 (1992) 28–33. https://doi.org/10.1557/S0883769400041634.

[101] R. Kasada, Y. Takayama, K. Yabuuchi, A. Kimura, A new approach to evaluate irradiation hardening of ion-irradiated ferritic alloys by nano-indentation techniques, Fusion. Eng. Des. 86 (2011) 2658–2661.

[102] D. Kiener, A.M. Minor, O. Anderoglu, Y. Wang, S.A. Maloy, P. Hosemann, Application of small-scale testing for investigation of ion-beam-irradiated materials, J. Mater. Res. 27 (2012) 2724–2736. https://doi.org/10.1557/jmr.2012.303.

[103] S. Li, Y. Wang, X. Dai, F. Liu, J. Li, X. Wang, Evaluation of hardening behaviors in ion-irradiated Fe–9Cr and Fe–20Cr alloys by nanoindentation technique, J. Nucl. Mater. 478 (2016) 50–55.

[104] M. Saleh, Z. Zaidi, M. Ionescu, C. Hurt, K. Short, J. Daniels, P. Munroe, L. Edwards, D. Bhattacharyya, Relationship between damage and hardness profiles in ion irradiated SS316 using nanoindentation – Experiments and modelling, Int. J. Plast. 86 (2016) 151–169.

[105] Y. Takayama, R. Kasada, Y. Sakamoto, K. Yabuuchi, A. Kimura, M. Ando, D. Hamaguchi, H. Tanigawa, Nanoindentation hardness and its extrapolation to bulk-equivalent hardness of F82H steels after single- and dual-ion beam irradiation, J. Nucl. Mater. 442 (2013) S23–S27.

[106] S. Agarwal, Y. Lin, C. Li, R.E. Stoller, S.J. Zinkle, On the use of SRIM for calculating vacancy production: Quick calculation and full-cascade options, Nucl Instrum Methods Phys Res B NUCL INSTRUM METH B. 503 (2021) 11–29. https://doi.org/10.1016/j.nimb.2021.06.018.

[107] Z. Jiao, S. Taller, K. Field, G. Yeli, M.P. Moody, G.S. Was, Microstructure evolution of T91 irradiated in the BOR60 fast reactor, J. Nucl. Mater. 504 (2018) 122–134. https://doi.org/10.1016/j.jnucmat.2018.03.024.

[108] G. Was, B. Wirth, A. Motta, D. Morgan, D. Kaoumi, P. Hosemann, R. Odette, High Fidelity Ion Beam Simulation of High Dose Neutron Irradiation, 2018. https://doi.org/10.2172/1437129.

[109] S. Taller, Z. Jiao, K. Field, G.S. Was, Emulation of fast reactor irradiated T91 using dual ion beam irradiation, J. Nucl. Mater. 527 (2019) 151831.

https://doi.org/10.1016/j.jnucmat.2019.151831.

[110] S. Taller, G.S. Was, Understanding bubble and void nucleation in dual ion irradiated T91 steel using single parameter experiments, Acta. Mater. 198 (2020) 47–60.

[111] B. Yao, D.J. Edwards, R.J. Kurtz, TEM characterization of dislocation loops in irradiated bcc Fe-based steels, J. Nucl. Mater. 434 (2013) 402–410. https://doi.org/10.1016/j.jnucmat.2012.12.002.

[112] C.M. Parish, K.G. Field, A.G. Certain, J.P. Wharry, Application of STEM characterization for investigating radiation effects in BCC Fe-based alloys, J. Mater. Res. 30 (2015) 1275–1289. https://doi.org/10.1557/jmr.2015.32.

[113] M.J. Mayo, W.D. Nix, A micro-indentation study of superplasticity in Pb, Sn, and Sn-38 wt% Pb, Acta. Mater. 36 (1988) 2183–2192.

[114] B.N. Lucas, W.C. Oliver, Indentation power-law creep of high-purity indium, Metall. Mater. Trans. A. 30 (1999) 601–610.

[115] S. Pathak, D. Stojakovic, R. Doherty, S.R. Kalidindi, Importance of surface preparation on the nano-indentation stress-strain curves measured in metals, J. Mater. Res. 24 (2009) 1142–1155.

[116] K.S. Mao, C. Sun, Y. Huang, C.-H. Shiau, F.A. Garner, P.D. Freyer, J.P. Wharry, Grain orientation dependence of nanoindentation and deformation-induced martensitic phase transformation in neutron irradiated AISI 304L stainless steel, Materialia. 5 (2019) 100208.

[117] T. Csanádi, M. Bl'anda, N.Q. Chinh, P. Hvizdoš, J. Dusza, Orientation-dependent hardness and nanoindentation-induced deformation mechanisms of WC crystals, Acta. Mater. 83 (2015) 397–407.

[118] H.L. Yang, S. Kano, J.J. Shen, J. McGrady, Y.F. Li, D.Y. Chen, K. Murakami, H. Abe, Investigation of anisotropic hardening response in a 12Cr-ODS ferritic steel subjected to 2.8 MeV Fe2+ irradiation, J. Nucl. Mater. 531 (2020) 152016.

[119] Y. Liu, S. Varghese, J. Ma, M. Yoshino, H. Lu, R. Komanduri, Orientation effects in nanoindentation of single crystal copper, Int. J. Plast. 24 (2008) 1990–2015.

[120] H. Jabir, A. Fillon, P. Castany, T. Gloriant, Crystallographic orientation dependence of mechanical properties in the superelastic Ti-24Nb-4Zr-8Sn alloy, Phys. Rev. Materials. 3 (2019) 063608.

[121] T. Chen, L. Tan, Z. Lu, H. Xu, The effect of grain orientation on nanoindentation behavior of model austenitic alloy Fe-20Cr-25Ni, Acta. Mater. 138 (2017) 83–91.

[122] M. Bachhav, G. Robert Odette, E.A. Marquis, α′ precipitation in neutron-irradiated Fe–Cr alloys, Scr. Mater. 74 (2014) 48–51.

[123] Y. Zhao, A. Bhattacharya, C. Pareige, C. Massey, P. Zhu, J.D. Poplawsky, J. Henry, S.J. Zinkle, Effect of heavy ion irradiation dose rate and temperature on α′ precipitation in high purity Fe-18%Cr alloy, Acta. Mater. 231 (2022) 117888. https://doi.org/10.1016/j.actamat.2022.117888.

[124] P. Zhu, Y. Zhao, S. Agarwal, J. Henry, S.J. Zinkle, Toward accurate evaluation of bulk hardness from nanoindentation testing at low indent depths, Mater. Des. 213 (2022) 110317. https://doi.org/10.1016/j.matdes.2021.110317.

[125] Z. Shang, J. Ding, C. Fan, D. Chen, J. Li, Y. Zhang, Y. Wang, H. Wang, X. Zhang, He ion irradiation response of a gradient T91 steel, Acta. Mater. 196 (2020) 175–190.

[126] F. Röder, C. Heintze, S. Pecko, S. Akhmadaliev, F. Bergner, A. Ulbricht, E. Altstadt, Nanoindentation of ion-irradiated reactor pressure vessel steels – model-based interpretation and comparison with neutron irradiation, Philos. Mag. 98 (2018) 911–933.

[127] T. Chen, L. He, M.H. Cullison, C. Hay, J. Burns, Y. Wu, L. Tan, The correlation between microstructure and nanoindentation property of neutron-irradiated austenitic alloy D9, Acta. Mater. 195 (2020) 433–445.

[128] C. Heintze, I. Hilger, F. Bergner, T. Weissgärber, B. Kieback, Nanoindentation of single- (Fe) and dual-beam (Fe and He) ion-irradiated ODS Fe-14Cr-based alloys: Effect of the initial microstructure on irradiation-induced hardening, J. Nucl. Mater. 518 (2019) 1–10.

[129] S. Li, Y. Wang, X. Dai, F. Liu, J. Li, X. Wang, Evaluation of hardening behaviors in ion-irradiated Fe–9Cr and Fe–20Cr alloys by nanoindentation technique, J. Nucl. Mater. 478 (2016) 50–55.

[130] X. Xiao, L. Yu, Comparison of linear and square superposition hardening models for the surface nanoindentation of ion-irradiated materials, J. Nucl. Mater. 503 (2018) 110–115.

[131] X. Liu, R. Wang, A. Ren, J. Jiang, C. Xu, P. Huang, W. Qian, Y. Wu, C. Zhang, Evaluation of radiation hardening in ion-irradiated Fe based alloys by nanoindentation, J. Nucl. Mater. 444 (2014) 1–6.

[132] G. Bonny, T. Khvan, A. Bakaeva, C. Yin, A. Dubinko, C. Cabet, M. Loyer-Prost, N. Castin, A. Bakaev, D. Terentyev, Effect of statistically stored dislocations in tungsten on the irradiation induced nano-hardening analyzed by different methods, J. Nucl. Mater. 543 (2021) 152543.

[133] V. Maier, K. Durst, J. Mueller, B. Backes, H.W. Höppel, M. Göken, Nanoindentation strain-rate jump tests for determining the local strain-rate sensitivity in nanocrystalline Ni

and ultrafine-grained Al, J. Mater. Res. 26 (2011) 1421–1430.

[134] P.S. Phani, W.C. Oliver, G.M. Pharr, An experimental assessment of methods for mitigating plasticity error during nanoindentation with continuous stiffness measurement, Mater. Des. 194 (2020) 108924.

[135] P.S. Phani, W.C. Oliver, G.M. Pharr, Understanding and modeling plasticity error during nanoindentation with continuous stiffness measurement, Mater. Des. 194 (2020) 108923.

[136] B. Merle, W.H. Higgins, G.M. Pharr, Critical issues in conducting constant strain rate nanoindentation tests at higher strain rates, J. Mater. Res. 34 (2019) 3495–3503.

[137] G.R. Speich, A.J. Schwoeble, W.C. Leslie, Elastic constants of binary iron-base alloys, Metall. Trans. 3 (1972) 2031–2037.

[138] K. Song, S. Das, A. Reza, N.W. Phillips, R. Xu, H. Yu, K. Mizohata, D.E.J. Armstrong, F. Hofmann, Characterising Ion-Irradiated FeCr: Hardness, Thermal Diffusivity and Lattice Strain, Acta. Mater. 201 (2020) 535–546.

[139] B.M. Drapkin, B.V. Fokin, Young's modulus and internal friction of FeCr alloys in relation to heat treatment, Met. Sci. Heat. Treat. 22 (1980) 325–329.

[140] H.C. Wu, B. Yang, S.L. Wang, M.X. Zhang, Y.Z. Shi, Y.F. Chen, Y.H. Sun, Effect of thermal aging on corrosion fatigue of Z3CN20.09M duplex stainless steel in high temperature water, Mater. Sci. Eng. A. 655 (2016) 183–192.

[141] A. Villuendas, J. Jorba, A. Roca, The Role of Precipitates in the Behavior of Young's Modulus in Aluminum Alloys, Metall. Mater. Trans. A. 45 (2014) 3857–3865.

[142] C. Zener, J.H. Hollomon, Effect of Strain Rate Upon Plastic Flow of Steel, J. Appl. Phys. 15 (1944) 22–32.

[143] E. Lucon, K. Abiko, M. Lambrecht, B. Rehmer, Tensile Properties of Commercially Pure, High-Purity and Ultra-High-Purity Iron: Results of an International Round-Robin, (2015). https://doi.org/10.6028/NIST.TN.1879.

[144] W.C. Oliver, G.M. Pharr, Measurement of hardness and elastic modulus by instrumented indentation: Advances in understanding and refinements to methodology, J. Mater. Res. 19 (2004) 18.

[145] S. Qu, Y. Huang, W.D. Nix, H. Jiang, F. Zhang, K.C. Hwang, Indenter tip radius effect on the Nix–Gao relation in micro- and nanoindentation hardness experiments, J. Mater. Res. 19 (2004) 3423–3434.

[146] M. Rester, C. Motz, R. Pippan, Microstructural investigation of the volume beneath nanoindentations in copper, Acta. Mater. 55 (2007) 6427–6435.

[147] D.S. Balint, V.S. Deshpande, A. Needleman, E. Van der Giessen, Discrete dislocation plasticity analysis of the wedge indentation of films, J. Mech. Phys. Solids. 54 (2006) 2281–2303.

[148] M.A. Mattucci, I. Cherubin, P. Changizian, T. Skippon, M.R. Daymond, Indentation Size Effect, Geometrically Necessary Dislocations and Pile-Up Effects in Hardness Testing of Irradiated Nickel, Acta. Mater. 207 (2021) 116702.

[149] J.R. Cahoon, W.H. Broughton, A.R. Kutzak, The determination of yield strength from hardness measurements, Metallurgical Transactions. 2 (1971) 1979–1983.

[150] J.T. Busby, M.C. Hash, G.S. Was, The relationship between hardness and yield stress in irradiated austenitic and ferritic steels, J. Nucl. Mater. 336 (2005) 267–278.

[151] E.J. Pavlina, C.J. Van Tyne, Correlation of Yield Strength and Tensile Strength with Hardness for Steels, J. Mater. Eng. Perform. 17 (2008) 888–893.

[152] A.J.E. Foreman, M.J. Makin, Dislocation movement through random arrays of obstacles, Philos. Mag. 14 (1966) 911–924.

[153] U.F. Kocks, The theory of an obstacle-controlled yield strength—Report after an international workshop, Mater. Sci. Eng. 27 (1977) 291–298.

[154] U.F. Kocks, A.S. Argon, M.F. Ashby, Thermodynamics and kinetics of slip, Prog. Mater. Sci. 19 (1975) 1.

[155] R.L. Fleischer, Substitutional solution hardening, Acta. Matell. 11 (1963) 203–209.

[156] T. Suzuki, On the Studies of Solid Solution Hardening, Jpn. J. Appl. Phys. 20 (1981) 449–462.

[157] R. Labusch, A Statistical Theory of Solid Solution Hardening, Phys. Stat. Sol. (b). 41 (1970) 659–669.

[158] G.T. Horne, R.B. Roy, H.W. Paxton, Tensile Properties of Single Crystals of Iron-Chromium Alloys, J. Iron. Steel. Inst. 201 (1963) 161.

[159] J.R. Stephens, W.R. Witzke, Alloy softening in binary iron solid solutions, J. Less. Common. Met. 48 (1976) 285–308.

[160] M.J. Kelley, N.S. Stoloff, Effect of chromium on low-temperature deformation of high-purity iron, MTA. 7 (1976) 331–333.

[161] S.J. Zinkle, Y. Matsukawa, Observation and analysis of defect cluster production and interactions with dislocations, J. Nucl. Mater. 329 (2004) 88–96.

[162] A. Seeger, J. Diehl, S. Mader, H. Rebstock, Work-hardening and work-softening of face-centred cubic metal crystals, Philos. Mag. 2 (1957) 323–350.

[163] F. Kroupa, P.B. Hirsch, Elastic interaction between prismatic dislocation loops and

straight dislocations, Discuss. Faraday Soc. 38 (1964) 49.

[164] J. Friedel, On the Elastic Limit of Crystals, in: Electron Microscopy and Strength of Crystals, Interscience, New York, 1963: pp. 605–648.

[165] G.R. Odette, G.E. Lucas, Recent progress in understanding reactor pressure vessel steel embrittlement, Radiat. Eff. Defects Solids. 144 (1998) 189–231.

[166] M. Hiratani, V.V. Bulatov, Solid-solution hardening by point-like obstacles of different kinds, Philos. Mag. Lett. 84 (2004) 461–470.

[167] L. Tan, J.T. Busby, Formulating the strength factor α for improved predictability of radiation hardening, J. Nucl. Mater. 465 (2015) 724–730.

[168] K. Edalati, Z. Horita, High-pressure torsion of pure metals: Influence of atomic bond parameters and stacking fault energy on grain size and correlation with hardness, Acta. Mater. 59 (2011) 6831–6836.

[169] S. Lu, Q.-M. Hu, B. Johansson, L. Vitos, Composition and orientation dependence of the interfacial energy in Fe-Cr stainless steel alloys, Phys. Status Solidi B. 248 (2011) 2087–2090.

[170] W.P. Davey, Precision Measurements of the Lattice Constants of Twelve Common Metals, Phys. Rev. 25 (1925) 753–761.

[171] Yu.I. Petrov, E.A. Shafranovsky, Yu.F. Krupyanskii, S.V. Essine, Structure and Mössbauer spectra for the Fe–Cr system: From bulk alloy to nanoparticles, J. Appl. Phys. 91 (2002) 352.

[172] W. Pepperhoff, M. Acet, Constitution and magnetism of iron and its alloys, Springer Science & Business Media, 2001.

[173] G. Ghosh, G.B. Olson, The isotropic shear modulus of multicomponent Fe-base solid solutions, Acta. Mater. 50 (2002) 2655–2675.

[174] J.-A. Sutlijfand, B.P. Bewlay, H.A. Lipsitt, High-temperature phase equilibria in Cr-Cr3Si two-phase alloys, J. Phase Equilibria. 14 (1993) 583.

[175] F. Bergner, C. Pareige, M. Hernández-Mayoral, L. Malerba, C. Heintze, Application of a three-feature dispersed-barrier hardening model to neutron-irradiated Fe–Cr model alloys, J. Nucl. Mater. 448 (2014) 96–102.

[176] I.M. Robertson, M.L. Jenkins, C.A. English, Low-dose neutron-irradiation damage in α-iron, J. Nucl. Mater. 108 (1982) 209–221. https://doi.org/10.1016/0022-3115(82)90489-5.

[177] W.-Y. Chen, Y. Miao, J. Gan, M.A. Okuniewski, S.A. Maloy, J.F. Stubbins, Neutron irradiation effects in Fe and Fe-Cr at 300 °C, Acta Materialia. 111 (2016) 407–416.

https://doi.org/10.1016/j.actamat.2016.03.060.

[178] L.L. Horton, J. Bentley, K. Farrell, A TEM study of neutron-irradiated iron, J. Nucl. Mater. 108–109 (1982) 222–233. https://doi.org/10.1016/0022-3115(82)90490-1.

[179] Z. Yao, M. Hernández-Mayoral, M.L. Jenkins, M.A. Kirk, Heavy-ion irradiations of Fe and Fe–Cr model alloys Part 1: Damage evolution in thin-foils at lower doses, Philos. Mag. 88 (2008) 2851–2880. https://doi.org/10.1080/14786430802380469.

[180] Y. Li, L. Wang, G. Ran, Y. Yuan, L. Wu, X. Liu, X. Qiu, Z. Sun, Y. Ding, Q. Han, X. Wu, H. Deng, X. Huang, In-situ TEM investigation of 30 keV he+ irradiated tungsten: Effects of temperature, fluence, and sample thickness on dislocation loop evolution, Acta. Mater. 206 (2021) 116618. https://doi.org/10.1016/j.actamat.2020.116618.

[181] A. Prokhodtseva, B. Décamps, A. Ramar, R. Schäublin, Impact of He and Cr on defect accumulation in ion-irradiated ultrahigh-purity Fe(Cr) alloys, Acta. Mater. 61 (2013) 6958–6971. https://doi.org/10.1016/j.actamat.2013.08.007.

[182] N. Soneda, S. Ishino, A. Takahashi, K. Dohi, Modeling the microstructural evolution in bcc-Fe during irradiation using kinetic Monte Carlo computer simulation, J. Nucl. Mater. 323 (2003) 169–180. https://doi.org/10.1016/j.jnucmat.2003.08.021.

[183] Y. Ding, G. Ran, Y. Li, Z. Cao, D. Cui, J. Huang, Z. Zhou, Effect of dose rate on dislocation loop evolution in tungsten: Combination of defect generation rate and elastic interaction, Scr. Mater. 222 (2023) 115054. https://doi.org/10.1016/j.scriptamat.2022.115054.

[184] J. Li, C. Zhang, Y. Yang, T. Wang, I. Martin-Bragado, Irradiation dose-rate effect in Fe-C system: An Object Kinetic Monte Carlo simulation, J. Nucl. Mater. 561 (2022) 153529. https://doi.org/10.1016/j.jnucmat.2022.153529.

[185] U.F. Kocks, A.S. Argon, M.F. Ashby, Thermodynamics and kinetics of slip, Prog. Mater. Sci. 19 (1975) 1–281.

[186] D.J. Dingley, D. McLean, Components of the flow stress of iron, Acta. Matell. 15 (1967) 885–901. https://doi.org/10.1016/0001-6160(67)90371-9.

[187] U.F. Kocks, H. Mecking, Physics and phenomenology of strain hardening: the FCC case, Prog. Mater. Sci. 48 (2003) 171–273. https://doi.org/10.1016/S0079-6425(02)00003-8.

[188] P.M. Kelly, The effect of particle shape on dispersion hardening, Scr. Metall. 6 (1972) 647–656. https://doi.org/10.1016/0036-9748(72)90120-2.

[189] C. Hin, B.D. Wirth, Formation of Y2O3 nanoclusters in nano-structured ferritic alloys: Modeling of precipitation kinetics and yield strength, J. Nucl. Mater. 402 (2010) 30–37.

https://doi.org/10.1016/j.jnucmat.2010.04.020.

[190] M. Praud, F. Mompiou, J. Malaplate, D. Caillard, J. Garnier, A. Steckmeyer, B. Fournier, Study of the deformation mechanisms in a Fe–14% Cr ODS alloy, J. Nucl. Mater. 428 (2012) 90–97. https://doi.org/10.1016/j.jnucmat.2011.10.046.

[191] A. Chauhan, F. Bergner, A. Etienne, J. Aktaa, Y. de Carlan, C. Heintze, D. Litvinov, M. Hernandez-Mayoral, E. Oñorbe, B. Radiguet, A. Ulbricht, Microstructure characterization and strengthening mechanisms of oxide dispersion strengthened (ODS) Fe-9%Cr and Fe-14%Cr extruded bars, J. Nucl. Mater. 495 (2017) 6–19. https://doi.org/10.1016/j.jnucmat.2017.07.060.

[192] M. Dadé, J. Malaplate, J. Garnier, F. De Geuser, F. Barcelo, P. Wident, A. Deschamps, Influence of microstructural parameters on the mechanical properties of oxide dispersion strengthened Fe-14Cr steels, Acta. Mater. 127 (2017) 165–177. https://doi.org/10.1016/j.actamat.2017.01.026.

[193] S.I. Porollo, A.M. Dvoriashin, A.N. Vorobyev, Yu.V. Konobeev, The microstructure and tensile properties of Fe–Cr alloys after neutron irradiation at 400°C to 5.5–7.1 dpa, J. Nucl. Mater. 256 (1998) 247–253. https://doi.org/10.1016/S0022-3115(98)00043-9.

[194] V.I. Dubinko, S.A. Kotrechko, V.F. Klepikov, Irradiation hardening of reactor pressure vessel steels due to the dislocation loop evolution, Radiat. Eff. Defects Solids. 164 (2009) 647–655. https://doi.org/10.1080/10420150903115743.

[195] X. Hu, D. Xu, T.S. Byun, B.D. Wirth, Modeling of irradiation hardening of iron after low-dose and low-temperature neutron irradiation, Modelling Simul. Mater. Sci. Eng. 22 (2014) 065002.

[196] M. Lambrecht, E. Meslin, L. Malerba, M. Hernández-Mayoral, F. Bergner, P. Pareige, B. Radiguet, A. Almazouzi, On the correlation between irradiation-induced microstructural features and the hardening of reactor pressure vessel steels, J. Nucl. Mater. 406 (2010) 84–89. https://doi.org/10.1016/j.jnucmat.2010.05.020.

[197] A. Dunn, R. Dingreville, L. Capolungo, Multi-scale simulation of radiation damage accumulation and subsequent hardening in neutron-irradiated α -Fe, Modelling Simul. Mater. Sci. Eng. 24 (2016) 015005. https://doi.org/10.1088/0965-0393/24/1/015005.

[198] L.K. Mansur, Correlation of neutron and heavy-ion damage, J. Nucl. Mater. 78 (1978) 156–160. https://doi.org/10.1016/0022-3115(78)90514-7.

[199] S.L. Dudarev, Density Functional Theory Models for Radiation Damage, Annu. Rev. Mater. Res. 43 (2013) 35–61. https://doi.org/10.1146/annurev-matsci-071312-121626.

[200] C.-C. Fu, J.D. Torre, F. Willaime, J.-L. Bocquet, A. Barbu, Multiscale modelling of

defect kinetics in irradiated iron, Nature Mater. 4 (2005) 68–74. https://doi.org/10.1038/nmat1286.

[201] Y.-R. Lin, A. Bhattacharya, D. Chen, J.-J. Kai, J. Henry, S.J. Zinkle, Temperature-dependent cavity swelling in dual-ion irradiated Fe and Fe-Cr ferritic alloys, Acta. Mater. 207 (2021) 116660. https://doi.org/10.1016/j.actamat.2021.116660.

[202] J. Henry, S.A. Maloy, Irradiation-resistant ferritic and martensitic steels as core materials for Generation IV nuclear reactors, in: Structural Materials for Generation IV Nuclear Reactors, Elsevier, 2017: pp. 329–355. https://doi.org/10.1016/B978-0-08-100906-2.00009-4.

[203] S.L. Dudarev, P.M. Derlet, R. Bullough, The magnetic origin of anomalous high-temperature stability of dislocation loops in iron and iron-based alloys, J. Nucl. Mater. 386–388 (2009) 45–48. https://doi.org/10.1016/j.jnucmat.2008.12.303.

[204] M.L. Jenkins, Z. Yao, M. Hernández-Mayoral, M.A. Kirk, Dynamic observations of heavy-ion damage in Fe and Fe–Cr alloys, J. Nucl. Mater. 389 (2009) 197–202. https://doi.org/10.1016/j.jnucmat.2009.02.003.

[205] Z. Yao, M.L. Jenkins, M. Hernández-Mayoral, M.A. Kirk, The temperature dependence of heavy-ion damage in iron: A microstructural transition at elevated temperatures, Philos. Mag. 90 (2010) 4623–4634. https://doi.org/10.1080/14786430903430981.

[206] X. Liu, Y. Miao, M. Li, M.A. Kirk, S.A. Maloy, J.F. Stubbins, Ion-irradiation-induced microstructural modifications in ferritic/martensitic steel T91, J. Nucl. Mater. 490 (2017) 305–316. https://doi.org/10.1016/j.jnucmat.2017.04.047.

[207] A. Bhattacharya, E. Meslin, J. Henry, F. Leprêtre, B. Décamps, A. Barbu, Combined effect of injected interstitials and He implantation, and cavities inside dislocation loops in high purity Fe-Cr alloys, J. Nucl. Mater. 519 (2019) 30–44.

[208] S. Novy, P. Pareige, C. Pareige, Atomic scale analysis and phase separation understanding in a thermally aged Fe–20at.%Cr alloy, J. Nucl. Mater. 384 (2009) 96–102. https://doi.org/10.1016/j.jnucmat.2008.10.008.

[209] Z. Jiao, V. Shankar, G.S. Was, Phase stability in proton and heavy ion irradiated ferritic–martensitic alloys, J. Nucl. Mater. 419 (2011) 52–62. https://doi.org/10.1016/j.jnucmat.2011.08.020.

[210] S. Taller, V. Pauly, Z. Jiao, R. Hanbury, G.S. Was, Solute segregation and precipitation across damage rates in dual-ion–irradiated T91 steel, J. Nucl. Mater. 563 (2022) 153626. https://doi.org/10.1016/j.jnucmat.2022.153626.

[211] Y. Chen, IRRADIATION EFFECTS OF HT-9 MARTENSITIC STEEL, Nuclear Engineering and Technology. 45 (2013) 311–322. https://doi.org/10.5516/NET.07.2013.706.

[212] D.L. Krumwiede, Correlation of Nanohardness to Bulk Mechanical Tensile and Shear Properties through Direct Characterization and Comparison of Neutron-Irradiated Steels, UC Berkeley, 2018. https://escholarship.org/uc/item/1qv0h8fk.

[213] T. Yamamoto, G.R. Odette, H. Kishimoto, J.-W. Rensman, P. Miao, On the effects of irradiation and helium on the yield stress changes and hardening and non-hardening embrittlement of ~8Cr tempered martensitic steels: Compilation and analysis of existing data, J. Nucl. Mater. 356 (2006) 27–49. https://doi.org/10.1016/j.jnucmat.2006.05.041.

[214] Y. Dai, J. Henry, Z. Tong, X. Averty, J. Malaplate, B. Long, Neutron/proton irradiation and He effects on the microstructure and mechanical properties of ferritic/martensitic steels T91 and EM10, J. Nucl. Mater. 415 (2011) 306–310. https://doi.org/10.1016/j.jnucmat.2011.04.029.

[215] S.A. Maloy, M. Toloczko, J. Cole, T.S. Byun, Core materials development for the fuel cycle R&D program, J. Nucl. Mater. 415 (2011) 302–305. https://doi.org/10.1016/j.jnucmat.2011.04.027.

[216] Y. Kohno, A. Kohyama, T. Hirose, M.L. Hamilton, M. Narui, Mechanical property changes of low activation ferritic/martensitic steels after neutron irradiation, J. Nucl. Mater. 271–272 (1999) 145–150. https://doi.org/10.1016/S0022-3115(98)00735-1.

[217] R.L. Klueh, J.M. Vitek, Tensile properties of 9Cr-1MoVNb and 12Cr-1MoVW steels irradiated to 23 dpa at 390 to 550 OC, (n.d.) 10.

[218] N. Hansen, Hall–Petch relation and boundary strengthening, Scr. Mater. 51 (2004) 801–806. https://doi.org/10.1016/j.scriptamat.2004.06.002.

[219] Q. Yuan, L. Chai, J. Shen, H. Wang, H. Guan, N. Guo, Y. Li, Microstructural characteristics, hardness and wear resistance of a typical ferritic/martensitic steel surface-treated by pulsed laser, Surf. Coat. Technol. 418 (2021) 127261. https://doi.org/10.1016/j.surfcoat.2021.127261.

[220] G. Gupta, G.S. Was, B. Alexandreanu, Grain boundary engineering of ferritic-martensitic alloy T91, Metall and Mat Trans A. 35 (2004) 717–719. https://doi.org/10.1007/s11661-004-0382-3.

[221] P. Ampornrat, G.S. Was, Oxidation of ferritic–martensitic alloys T91, HCM12A and HT-9 in supercritical water, J. Nucl. Mater. 371 (2007) 1–17. https://doi.org/10.1016/j.jnucmat.2007.05.023.

VITA

Pengcheng Zhu was born at Yichang, Hubei, China in 1991. He entered Huazhong University of Science and Technology in 2010 and received a bachelor's degree in Nuclear Engineering in 2014. The following September he entered Shanghai Jiao Tong University and obtained a master's degree in Nuclear Engineering in June 2017. Then he joined Dr. Steven Zinkle's group at the University of Tennessee for PhD study on nuclear materials. He received a PhD degree in Nuclear Engineering in April 2023.